UNIVERSITY OF OSLO

Master thesis

Patient Specific Robust Optimisation Strategies for Mitigation of Intra-Fractional Motion Effects on Proton Beam Therapy of Lung Cancer

June 2023

Kyriakos Fotiou

Biological and Medica Physics

FYS5960 60

Department of Physics

The Faculty of Mathematics and Natural Sciences

Supervisor: Eirik Malinen

Co-supervisors: Taran Paulsen Hellebust, Per-Ivar Lønne

Abstract

Purpose: Intensity Modulated Proton Beam (IMPT) therapy has emerged as a highly relevant option relevant treatment option due to the favourable physical properties of protons. However, respiratory anatomical changes in the thorax region due to respiration have a significant impact on plan quality due to proton transport sensitivity to tissue alterations. Shifts of the Bragg peaks with respect to planned locations cause geometrical misses of the tumor, leading to distortions in the dose distribution and subsequent plan degradation. Still, these effects are patient-specific and better treatment plan approaches need to be identified to identify robust plan parameters that mitigate them. The purpose of this study is to analyse intrafractional motion effects from 4D-CT scans to identify robust treatment angles that minimise Bragg peak shifts while taking into consideration dose to organs at risk. In addition, the efficacy of robust optimisation plan techniques to generate treatment plan resistant to anatomical motions was evaluated.

Materials and Methods: 4D-CT scans of 11 Locally Advanced Non-Small Cell Lung Cancer (LA-NSCLC) were selected from The Cancer Imaging Archive (TCIA) 4D Lung database. The patients exhibit different breathing patterns, tumor motions and tumor sizes, and are representative for clinical applications. Stoichiometric calibration was performed to generate the Hounsfield Unit Look-Up Table (HULT) for the conversion of the CT number to proton Relative Stopping Power (RSP). The 4D-CT scan and the Average Intensity Projection CT scan were converted to RSP-CT scan and Water Equivalent Path Length (WEPL) analysis was performed to identify the optimal beam geometries. The AIP ST scan was employed as the planning CT, and the variation in the WEPL (ΔWEPL) along the beam path from the planned and evaluated CT scans was estimated for 350 unique couch gantry angle combinations. The average beam ΔWEPL were then correlated with dose degradation in Internal Clinical Target Volume (iCTV) by observing reduction of D95 and D98 from planned and evaluated dose. The effect of the incident beam geometry on OAR was also investigated by estimating the percentage irradiated volume of the organ in question from the incident beam and correlating the result with the organ accumulated dose. Treatment planning was performed in RayStation (Raysearch AB, Stockholm) where 3D and 4D robust optimisation strategies where evaluated. The impact of the optimisation strategy on plan robustness was analysed by observing both target coverage and dose to organs at risk.

Results: A Pearson statistical test was employed to evaluate the correlation of ΔWEPL and OAR percentage irradiation with iCTV dose reduction and OAR accumulated dose respectively. Strong positive correlations were observed for ΔWEPL and iCTV dose reduction, with population average Pearson coefficient of 0.89 for ΔD95 and 0.89 for ΔD98, indicating the potential of WEPL analysis in identifying the effect of incident beam geometry on target dose degradation. Additionally, analysis of OAR percentage irradiation also revealed significant correlations, with the average Pearson coefficients of 0.88 for heart D5, 0.98 for heart Dmean, 0.93 for spinal cord D5, 0.97 for spinal cord Dmean, 0.90 for lungs Dmean and 0.89 for lungs V20, emphasising the influence of beam orientation on organ dose. While 3D optimisation was generally successful, 4D optimisation demonstrated superior performance, particularly in handling complex motion patterns and achieving a more homogeneous dose distribution.

Conclusion: In this study strong correlations between ΔWEPL and OAR percentage irradiation with target dose reduction and OAR accumulated dose were observed. The generated angle selection algorithm employed utilising the aforementioned variables, was thus successful in identifying robust beam geometries. 4D robust optimisation depicted an advantage over 3D robust optimisation plans in generating more homogenous dose distributions across the breathing cycle. . However, it is important to acknowledge that these advantages were accompanied by a higher accumulated organs at risk dose.

Contents

1.   Introduction

Cancer is a pervasive disease that has a significant impact on global health. In 2020, it was estimated that approximately 10 million deaths were attributable to cancer [1]. Among the various types of cancer, lung cancer ranks as the third most common, following prostate cancer and breast cancer, with 3466 cases reported in 2022 in Norway [2]. Non-Small Cell Lung Cancer (NSCLC) is the predominant form of lung cancer, accounting for the majority of cases. Unfortunately, lung cancer is responsible for the highest number of cancers related deaths globally, with five-year survival rates reported at 30.0% in Norway [2]. Thus, it is important to explore new strategies to improve likelihood of cure.

Lung cancer is known for its aggressive nature and dismal prognosis, largely attributed to late-stage diagnosis. A significant portion of lung cancer cases were diagnosed when the disease has already advanced. In 2022, only 27.8% of diagnosed lung cancer cases were found to be in stage I, whereas a substantial 43.9% were classified as stage IV in Norway. Current treatment modalities for lung cancer patients include a combination of radiotherapy with curative or palliative intent, chemotherapy, surgery, and immunotherapy. For inoperable locally advanced (LA)-NSCLC, the standard treatment is a combination of chemotherapy with curative intended radiation therapy.

Radiotherapy plays a significant role in the management of lung cancer, with approximately half the patients undergoing this modality. Studies have demonstrated that lung cancer tends to respond better to higher radiation doses [3]. However, there are limitations to the dose that can be delivered to patients due to the proximity of the tumour to critical organs at risk, such as the heart, and the irradiated healthy lung volume. Irradiation can lead to severe organ toxicities, which are dependent on the dose levels and irradiated volume of the organ in question. The volume of the lung that is exposed to radiation is influenced by factors such as the size of the tumour, the type of radiation used, the angles which the incident beams are directed and the extent of tumour motion. Lung tumours exhibit motion within the thoracic cavity due to the natural process of respiration [4]. The respiratory motion poses a challenge in conventional radiotherapy, as a larger volume of the lung needs to be irradiated in order to adequately cover the entire tumour with sufficient dose. This effect becomes more significant for more pronounced tumour motions. However, it is important to note that the extend and characteristics of tumour motion can vary from patient to patient. Factors such as lung compliance, tumor location, and patient-specific breathing patterns contribute to the degree and nature of tumor motion during respiration. Consequently, the magnitude and direction of tumor motion can vary among patients.

The use of Intensity Modulated Proton Therapy (IMPT) has emerged as significantly relevant treatment option for locally advanced lung cancer due to the favourable physical properties of protons compared to high-energy photons utilised in conventional radiotherapy [5]. Protons possess a characteristic property known as Bragg peak, where their stopping power is highest at the end of their particle track. This unique characteristic allows for the potential delivery of naturally high dose

deposition within the tumour if an appropriate kinetic energy is extracted from the beamline. Therefore, by utilising proton therapy, it becomes possible to deliver a highly conformal dose to the target volume while minimising the dose accumulated by organs at risk. This precision in dose delivery offers an advantage over conventional radiotherapy, where the surrounding healthy tissues may receive higher doses due to the inherent properties of high energy X-rays.

However, this advantage of proton therapy also presents challenges related to the sensitivity of proton transport in tissue alterations. In the presence of anatomical changes during the course of fractionated therapy, the initial planned proton kinetic energy and fluence distribution may no longer provide sufficient coverage of the tumour. Moreover, these alterations may also affect healthy tissue to a greater extent than anticipated during treatment planning. Alterations in patient anatomy can occur gradually over the course of days, weeks or months, and monitoring and evaluation of these changes is necessary. Repeat CT images acquired during fractionation are commonly employed to assess any deviations in patient anatomy. Continuous monitoring and adaptive strategies based on the repeat CT scans provide opportunities to personalise the proton therapy for each patient [6].

Furthermore, the presence of tumour motion during radiation delivery as mentioned previously, presents additional challenges for proton therapy. Unlike conventional X-ray radiotherapy, proton beams exhibit greater sensitivity to rapid anatomical changes due to the inherent characteristics of proton transport in tissue. Treatment planning in radiotherapy is based on a static representation of the patient anatomy and does not inherently account for intrafractional motion, which refers to the internal motion of anatomical structures due to respiration. To address the impact of intrafractional motion, advanced imaging techniques such as 4D CT scans have been employed. These scans involve capturing a series of 10 CT images, where each phase represents a different phase of the patient's breathing cycle [7]. By incorporating 4D CT scans into treatment planning, information of the patient specific intrafractional motion can be obtained and incorporated in the planning process.

The presence of intrafractional motion in proton therapy presents various factors that can affect the precision of IMPT. These factors arise from alterations in the treatment volume and beam path due to the motion of the tumour and surrounding anatomy [8]. Geometrical misses may occur when delivered radiation dose not accurately target the tumour due to its motion. Proton range uncertainties can arise from tissue alterations along the planned beam path due to respiratory induced motion, leading to reduction of the dose delivered to the tumour . Additionally, the interplay effect between the dynamic tumour motion and the active scanning of proton beams can further impact treatment accuracy.

Estimation of the Water Equivalent Path Length (WEPL) of protons within the patient can provide valuable insight into the impact of intrafractional motion. By quantitively analysing the variation in WEPL between the planned CT scans and the evaluated 4D CT scan, becomes possible to assess tissue variations along the beam path and estimate the magnitude of the induced Bragg peak shift. These shifts can be attributed to variations in lung densities traversed by the beam, or the movement of organs and bone structures in and out of the beam path during certain breathing phases. Such effects have a significant influence on the proton stopping power, leading to shifts of the Bragg peak and

subsequent degradation of the planned dose distribution. WEPL analysis can be performed to evaluate the effects of intrafractional motion as a function of incident beam geometry, with beam angles that exhibit the highest robustness being selected for treatment planning [9]. Previous studies identified positive correlations between variations in WEPL along planned and evaluated beam paths and the resulting dose reduction in the target volume. To evaluate the WEPL from the CT images, a stoichiometric calibration can be performed to convert the Hounsfield Units, which represent X-ray attenuation, to proton stopping power relative to water (RSP) [10]. The integrated RSP values along the traversed beam path depict the water equivalent estimation of the proton range.

However, in radiation therapy of lung cancer, it is crucial to optimise incident beam angles not only for tumour coverage, but also to minimise the accumulated dose to critical organs at risk (OARs) [11]. The impact of dose on OARs is a crucial factor in determining treatment outcomes and potential side effects, as mentioned previously. A comprehensive analysis involving the evaluation of irradiated volume of a specific OAR as a function of incident beam angle can provide valuable insight into incident beam geometries where direct irradiation of OARs is minimised. However, it is essential to consider not only the irradiate volume but also the proximity and spatial relationship between the tumour and critical organs in order to account for dose accumulated by the organ through secondary electrons.

Conventional X-ray radiotherapy typically utilises additional margins on target volume, to compensate for variations in tumour geometry and motion during beam delivery. However, the highly modulated nature of IMPT necessitates a more sophisticated approach known as robust optimisation, to address proton range, setup and intrafractional uncertainties that occur during beam delivery [12]. Robust optimisation aims to identify beam parameters that are resilient to uncertainties by incorporating them into the optimisation algorithm. Currently, the treatment planers have the option to choose between 3D and 4D robust optimisation strategies. 3D robust optimisation is performed solely on the planning CT scan ad does not explicitly account for respiratory motion effects. In contrast, 4D robust optimisation incorporates all breathing phases and explicitly considers the uncertainties associated with intrafractional motion in the optimisation algorithm. However, previous studies have shown that 3D robust optimisation can yield treatment plans that are resistant to respiratory motion effects, without explicitly accounting for them [13]. Comparing the efficacy of both robust optimisation strategies in relation to tumour motion can provide valuable insight into the preferred method for treatment planning for IMPT.

1.1 Aim

The primary objective of this study was to utilise 4D CT scan of 11 LA-NSCLC patients to extract patient specific information regarding intrafractional motion. The extracted data were then used to develop robust treatment plans capable of mitigating the impact of intrafractional motion.

An angle selection algorithm was devised to analyse variations in WEPL along the beam path from planned and evaluated CT scans, enabling the identification of robust beam angles that ensure

adequate tumour coverage. Moreover, the algorithm investigated the irradiated volume for the heart, lungs and spinal cord and incorporated this information into the angle selection process to minimise potential radiation induced organ toxicity. Furthermore, a comprehensive analysis of tumour motion was conducted, encompassing tumour translational displacement, volumetric variation, and the creation of a Tumor Location Probability (TLP) map. Subsequently, treatment plans were generated using both 3D and 4D robust optimisation techniques, with their effectiveness in mitigating motion effects evaluated.

1.2 Hypotheses

To facilitate the investigation of patient specific plan optimisation for IMPT of lung cancer, the study formulated several hypotheses.

1. Statistically significant correlations between variation in the WEPL to the distal edge of the iCTV estimated from the planned and evaluated CT scans, and the resulting dose reduction in iCTV D95 ,dose received by 95% of the iCTV volume, and D98.
2. Percentage of irradiated organ has a statistically significant correlation with accumulated organ dose.
3. 4D robust optimisation outperforms 3D robust optimisation in generating treatment plans that are more resistant to intrafractional effects.

2. Theory

2.1 Lung Cancer

The lungs are a pair of organs situated in the thorax region, and their primary function is to enable the process of gas exchange known as respiration. During respiration, oxygen is taken in from the inhaled air and enters the bloodstream, while carbon dioxide, a waste product of metabolism, is removed from the blood. The lungs are enclosed within the chest wall and are surrounded by a fluid-filled space, which allows from the smooth movement during respiration. Between the lungs, there is a region known as the mediastinum, which houses the heart, systemic blood vessels and lymph nodes. Beneath the lungs, the diaphragm muscle is located. When we inhale, the diaphragm contracts, causing the lungs to expand and creating a pressure difference with the air outside the body, which allows air to enter the body. Conversely, when the diaphragm relaxes, lung pressure increases, resulting in the expulsion of air from the body during exhalation.
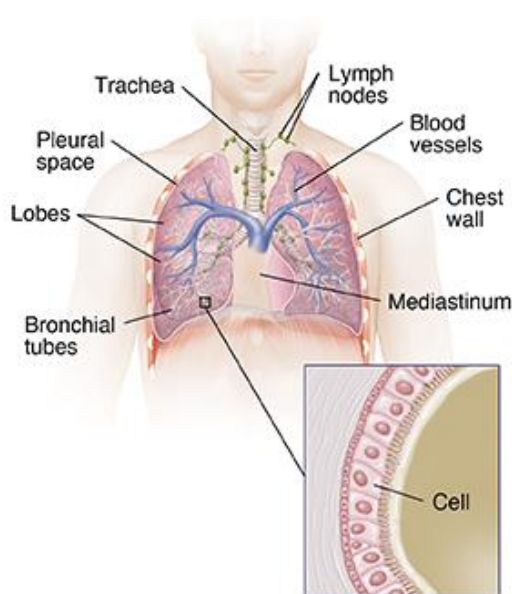
Figure 2.1: Lungs Anatomy. [14]

The lungs like other organs, are composed of various tissue and cell types. Under normal conditions, these cells undergo the controlled process of the cell cycle, where they grow and divide at a regulated pace, ensuring a balanced number of cells in the organ. However, genetic mutations can disrupt the control system of cell division in one or several cells, causing them to divide uncontrollably. This uncontrolled cell division leads to the accumulation of damaged cells, forming tumours. Tumours can be classified in two categories, malignant and benign. Malignant tumours have the ability to invade

surrounding tissues and can spread to other regions of the body through the blood or lymphatic system. These tumours often require treatment due to their potential to cause severe complications in the patient's health. On the other hand, benign tumours do not possess the ability to spread and typically do not pose significant threat. Treatment for benign tumours is usually necessary only when they are located in a malignant position that affects the function of adjacent organs.

The process of cells spreading to other parts of the body is known as metastasis. In the case of lung cancer, common metastasis sites include the lymph nodes in the thorax and particularly mediastinum regions. Distance metastasis occurs when cancer cells break away from the primary tumour and travel to distant organs such as the liver, brain or bones through the lymphatic system or blood vessels.

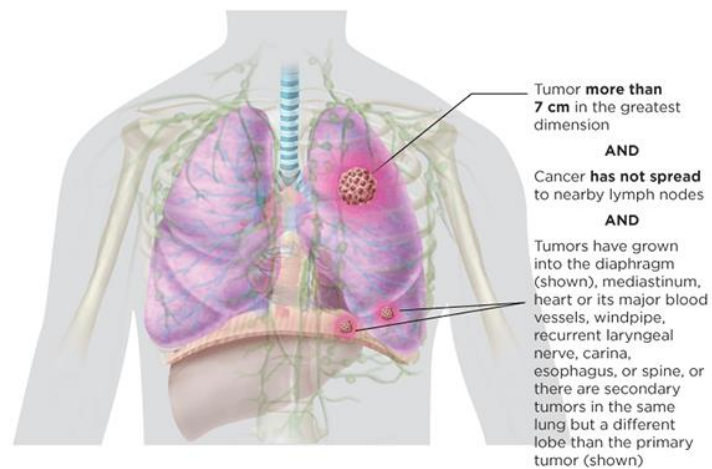## 2.1.1 Non-small cell lung cancer.

There are two main types of lung cancer, categorised by the size and appearance of the malignant cells during histological analysis of the cells. Small cell lung carcinoma is a highly aggressive form of lung cancer that accounts for approximately 15% or lung cancer cases. Non-Small Cell Lung Cancer (NSCLC) is the most common type which accounts for 85% of lung cancer cases.

Non-small cell lung cancer (NSCLC) is staged using the TNM system, based on tumor size and invasion (T), lymph node involvement (N), and distant metastasis (M). The stages range from stage I (localized disease) to stage IV (advanced metastatic disease). In stage I NSCLC, the tumor is small and confined to the lung without lymph node involvement or metastasis. Stage II involves larger tumors or those that have spread to nearby lymph nodes. Stage III NSCLC indicates extensive lymph node involvement or tumor invasion into adjacent structures. Stage IV NSCLC signifies the presence of distant metastasis. Staging plays a critical role in determining treatment strategies and predicting prognosis for patients with NSCLC.

Locally advanced non-small cell lung cancer (NSCLC) refers to a stage of the disease where the tumor has extended beyond the lung to nearby structures or lymph nodes but has not spread to distant organs. The degree of regional metastasis and the size of the primary tumour varies at this stage, with III NSLCS being further divided into IIIA, IIIB, IIIC. Figure 2.2 depicts visualisations of stages IIIA and IIIB

Stage IIIA NSCLC indicates involvement of lymph nodes on the same side of the chest as the primary tumor, while stage IIIB NSCLC signifies either extensive lymph node involvement on the same side or the presence of a tumor that has invaded nearby structures such as the chest wall or the esophagus. Locally advanced NSCLC poses challenges in treatment decision-making, often requiring a multimodal approach that may include a combination of surgery, radiation therapy, and chemotherapy. Accurate staging is crucial for guiding treatment strategies and predicting outcomes in patients with locally advanced NSCLC.

Lung Cancer: **Stage IIIA**

Tumor **more than 7 cm** in the greatest dimension

AND

Cancer **has not spread** to nearby lymph nodes

AND

Tumors have grown into the diaphragm (shown), mediastinum, heart or its major blood vessels, windpipe, recurrent laryngeal nerve, carina, esophagus, or spine, or there are secondary tumors in the same lung but a different lobe than the primary tumor (shown)

Lung Cancer: **Stage IIIB**

Tumor **more than 5 cm** in the greatest dimension

AND

Cancer **has spread** to mediastinal lymph nodes, which include subcarinal nodes, near the lung with the primary tumor

AND

Tumors have grown into the lung's outer lining or nearby sites including the chest wall (shown), phrenic nerve, or the heart's lining, or there are primary or secondary tumors in the same lobe; and/or tumors have grown into the mediastinum, heart or its major blood vessels, windpipe, recurrent laryngeal nerve, carina, esophagus, or spine, or there are secondary tumors in the same lung but a different lobe than the primary tumor (shown)
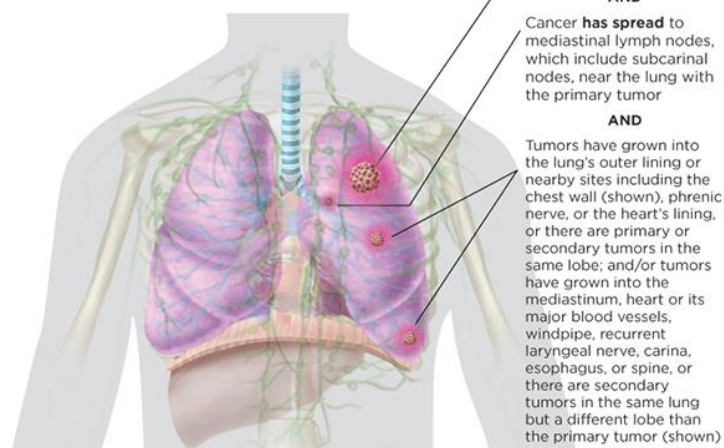
Figure 2.2: Illustrates the staging classification of Stage III Non-Small Cell Lung Cancer (NSCLC). The top figure represents Stage IIIA, characterized by a primary tumor larger than 7mm with invasion into intrathoracic regions. The bottom figure depicts Stage IIIB, which is assigned to tumors smaller than 5cm that have metastasized to regional lymph nodes and potentially infiltrated the main bronchus [16].

2.2 Interactions of Radiation with Matter.

Understanding the fundamental nuclear interactions for photons and protons with matter is essential in comprehending their application in radiation therapy for both treatment and imaging purposes. In radiation the incident radiation possesses sufficient primary energy to induce the liberation of electrons from atoms. Such radiation is referred as ionising radiation and can be further classified into two categories, direct and indirect ionisation. Direct ionisation involves the interaction of fast charged particles, such as protons, with matter. These particles directly transfer energy to the medium through small Coulomb forces, resulting in ionisation of the surrounding atoms. In contrast, photons and neutrons interact indirectly with matter, by first transferring energy to charged particles in the medium, predominantly electrons, which subsequently directly ionise the medium.

Cross Section

In nuclear physics, a Cross Section is used to quantify the probability of interaction between incident radiation and a target nucleus. It represents the effective area, denoted as σ, within which the interaction is expected to occur. This concept can be visualized by considering two spheres, one representing the stationary target nucleus and the other representing the incident particle in motion. Despite the physical sizes of the particles being much smaller, the effective area of interaction is significantly larger due to electromagnetic interactions. The magnitude of the cross section depends on multiple factors, including the properties of the target nucleus and the type and energy of the incoming radiation. It is important to note that while the cross section can be visualized using a classical window analogy, its calculation is based on quantum mechanics. The probability of interaction is thus defined as,

$$P = n\sigma/\Sigma,$$

(2.1)

Where, n is the number of atoms in the medium with area Σ, while the number of interactions can be obtained by multiplying with the number of incoming particles. The differential cross section is defined as the cross section per unit solid angle for particles scattered at an angle from the incident radiation. Through the differential cross section, we obtain information about the angular distribution of scattered particles from the target and understand the nature of the nuclear interaction and properties of the target nucleus.

2.2.1 Photon Interactions.

Photon interactions with matter primarily occur through two fundamental mechanisms: absorption and scattering as visualised in *Figure 2.3*. During absorption, the energy of the photon is transferred to the atom, promoting one of its electrons to a higher energy state or completely removing it from

the atom. Scattering, on the other hand, involves a change in the direction of the incident photon subsequent to a coherent or incoherent interaction with the target atom.
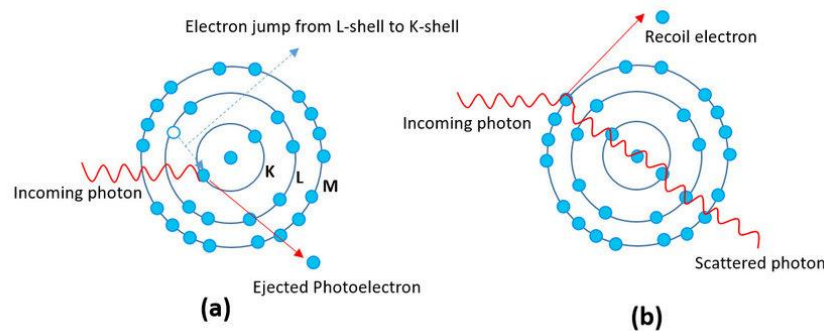

Figure 2.3: Visualisation of the primary interaction mechanisms of photons with matter. On the left (a) depicts absorption of the incident photon and on the right (b) indicates a scattering interaction [17].

2.2.1.1 Photoelectric Effect.

The photoelectric effect is a phenomenon theorised by Albert Einstein, where the incident photon is absorbed by the atom and results in excitation or ionisation based on the incident photon's energy.
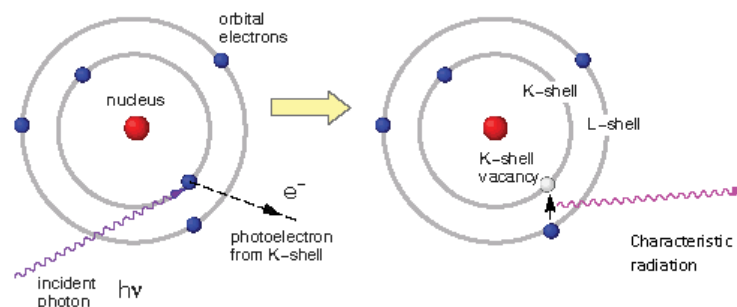

Figure 2.4: Schematic of the photoelectric effect interaction. The incident photon interacts with an atom, resulting in the ionization of the atom and the emission of a characteristic radiation photon [18].

When photons interact with atoms, the outcomes depend on the energy of the incident photons in relation to the binding energies of the atomic electrons. If the energy of the incident photon is below the binding energy, the atom undergoes excitation. In this process, the electron is promoted to a higher energy state within the atom. Following excitation, the atom can subsequently de-excite by emitting a photon and returning the electron to its original energy state. On the other hand, when the incident photon energy exceeds the binding energy of the electron, ionization of the atom occurs. The excess energy of the photon is transferred to the electron, enabling it to break free from the atom's binding forces. As a result, the atom becomes ionized, with the electron being released and the atom carrying a positive charge. The energy of the released electron can be approximated by $T \approx hv - E_b$, where hv is the energy of the incident photon while E_b is the binding energy of the electron. De-excitation of the atoms occurs in two principle ways, through emission of characteristic radiation as

depicted in *Figure 2.4* or by the auger effect. Characteristic radiation is the de-excitation of an electron from a higher to a lower energy state within the atom. For this electronic transition to occur there must be an isotropic emission of a γ-ray, where the photon's energy is depended on the electronic structure and transition probabilities of the target atom. For the auger effect, which dominates in low atomic number targets, the energy release occurs through the ejection of a loosely bound electron. The energy of the released electron equals the de-excitation energy and will result in the atom being positively charged by 2.The atomic cross-section for the photoelectric effect assuming no binding energy is defined as,

$$\frac{d\tau}{d\Omega} = 2\sqrt{2}r_o^2 a^4 Z^5 \left(\frac{m_e c^2}{hv^2}\right)^{\frac{7}{2}} sin^2\Theta \left(1 + 4\sqrt{\frac{2hv}{m_e c^2}}cos\Theta\right) \tag{2.2}$$

Where, r_o is the classical electron radios, a is the fine-structure constant, Ω is the single angle depicting the direction of the ejected electron, m_e is the rest mass of the electron and c is the speed of light. Equation (2.2) demonstrates the complex relationship of the cross section and various factors. However, in the context of medical applications, it is notable that the cross section is primarily influenced by two key factors, the atomic number (Z) raised to the power of 5 (Z^5) and the inverse cubed photon energy *1/(hv)³*. The Z^5 dependence highlights that interactions are more likely to occur with heavier target nuclei that possess a greater number of electrons available for excitation. Furthermore, the cross section decreases as the photon energy increases, indicating that the photoelectric effect becomes the dominant interaction mechanism for low-energy photons. It is important to consider that the specific values of the proportionality factors for atomic number and photon energy will vary due to the differences in electron binding energies among target atoms. A more general formula is depicted in equation 2.3 as,

$$\tau \propto \frac{Z^n}{(hv)^m} \quad 4<n<5, \; 1<m<3 \tag{2.3}$$

Additionally, the direction of the emitted photoelectron is influenced by the energy of the incident photon. *Figure 2.5* illustrates that higher-energy photons tend to result in a more forward direction of the emitted photoelectron.
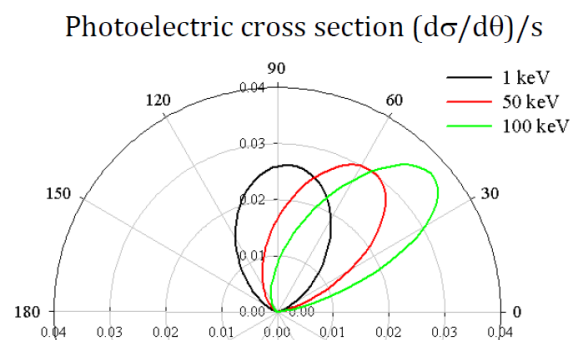

Figure 2.5: Relationship between incident photon energy and direction of emitted photoelectron. [19]

2.2.1.2   Compton Scattering

Compton scattering was discovered by Arthur H. Compton through observations of X-rays scattering from electrons in a carbon target and is characterised by a wavelength shift of the scattered x-ray compared to the incident one as visualised in *Figure 2.6*.
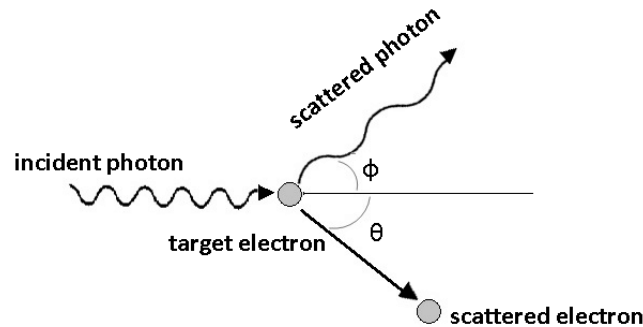

Figure 2.6: Schematic of the Compton scattering phenomenon [20].

Compton's research demonstrated that the extent of this wavelength shift is determined by the scattering angle, as described by the Compton equation.

$$\lambda_f - \lambda_i = \frac{h}{m_e c^2}(1 - cos\ \Phi) \tag{2.4}$$

Where λ_f is the final wavelength, λ_i is the initial wavelength and Φ the scattering angle of the photon. Compton provided an explanation for this phenomenon based on the principles of conservation of momentum and energy. Analysing equation (2.4) reveals that the maximum energy transferred to the electron occurs at a scattering angle of 180 degrees, and this transfer is not influenced by the initial photon energy.

The differential cross section for Compton scattering was derived by Klein and Nishina, considering cylindrical symmetry and integrating over all angles. It is mathematically expressed as,

$$\sigma_e = \int_0^\pi \pi r^2 \left(\frac{V'}{V}\right)^2 \left(\frac{V'}{V} + \frac{V}{V'} - sin^2\theta\right) sin\theta\ d\theta, \tag{2.5}$$

where V', is the frequency of the scattered photon, V the frequency of the incident photon and θ the scattering angle of the photon, with the atomic cross section defined as $\sigma_C = Z\sigma_e$. Therefore, we can conclude that the atomic cross-section is proportional to the atomic number Z and inversely proportional to the photon energy *(1/hv)*. Based on this relationship, we can infer that as the incident photon energy increases, the dominant interaction transitions from the photoelectric effect to Compton scattering. Furthermore, the probability of interaction is influenced by the electron density of the target material, with a higher probability in materials that have more loosely bound electrons.

Finally, we can observe that as the photon energy increases, the scattered photons tend to be more forwardly directed. This observation can be attributed to the scattering angle dependence in Compton scattering. Conversely, at low photon energies, the scattering angle distribution appears isotropic, indicating a relatively uniform distribution of scattered photons in all directions as illustrated in *Figure 2.7*.
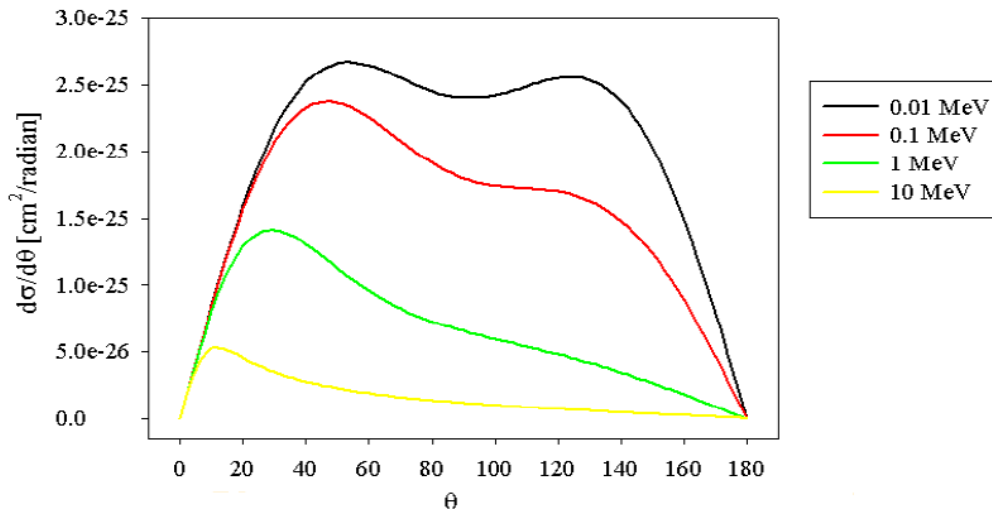

Figure 2.7: Klein- Nishina differential cross section scattering angle distribution for varying incident photon energy. Low energy photons depict an isotropic scattering angle with higher energies indicating a more forward scattered photon.

2.2.1.3 Rayleigh Scattering

Rayleigh scattering is a phenomenon that, similar to Compton scattering, causes a deviation in the path of the incident photon. However, unlike Compton scattering, Rayleigh scattering is a coherent interaction in which the energy of the photon remains unchanged. During Rayleigh scattering, the photon is absorbed by the atom and subsequently re-emitted at a small deflection angle. The probability of this interaction depends on both the atomic structure of the target material and the energy of the incident photon with the atomic cross section defined as,

$$\sigma_R = \left(\frac{Z}{h v}\right)^2 \tag{2.6}$$

Since Rayleigh scattering is an elastic interaction where the energy of the incident photon remains unchanged and the photon path is only slightly deviated, it does not significantly affect the interaction of photons within the medium. Therefore, for practical purposes in the medical sector, Rayleigh scattering is typically overlooked, focusing instead on other more relevant photon-matter interactions.

2.2.1.4 Pair Production.

Pair production represents a significant phenomenon where a high-energy photon undergoes absorption within the nuclear electromagnetic field of an atom, leading to the generation of an electron-positron pair. This intricate process necessitates the incident photon's energy to exceed twice the rest mass energy of the electron, approximately 1.022 MeV, to facilitate the interaction. A schematic representation of this process can be observed in Figure 5.
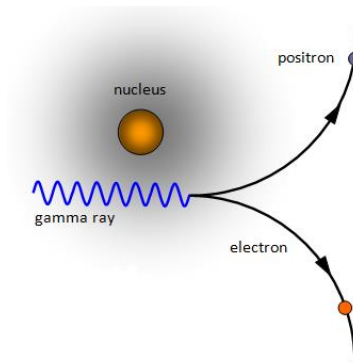

Figure 2.8: Schematic of pair production. The incident photon is absorbed, and an electron positron pair is generated [21].

The determination of the total cross section for pair production is complex and often approximated through theoretical models. It encompasses various factors such as the properties of the target material, the energy of the incident photons, and quantum electrodynamics principles. For the purpose of this study, the atomic cross section of pair production can be approximated by,

$$k \approx a r_0^2 Z^2 \bar{\bar{P}}.$$

(2.7)

By inspection of equation (2.7), it can be inferred that the atomic cross section for pair production is proportional to the square of the atomic number and the energy of the incident photon. This relationship implies that pair production becomes increasingly significant for high-energy photons and in materials with higher atomic numbers.

2.2.1.5 Photon Attenuation

In the context of radiation therapy, it is crucial to exceed the examination of individual photon-atom interactions and consider the collective behaviour of an X-ray beam as it interacts with complex objects such as the human body, which consist of various atoms and densities. Photon attenuation, which refers to the reduction in the intensity of a photon beam as it traverses through matter, plays a fundamental role in this process. The attenuation is quantified by the linear attenuation coefficient (μ), which represents the probability of interaction per unit length and is measured in units of m^{-1}. Consequently, the intensity of the incident beam as a function of the distance travelled can be described by the equation,

$$I = I_0 e^{\mu x}$$

Where I_0 is the initial intensity of the beam and x is the distance travelled by the photon beam in the medium. As entailed by equation (2.8), and depicted in *Figure 2.8*, the beam intensity diminishes with an inverse exponential behaviour.
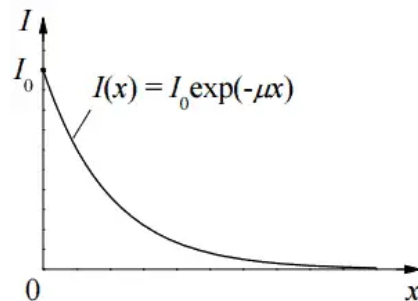

Figure 2.9: Relationship between photon beam intensity and thickness of attenuating medium [22].

It is important to note that the aforementioned behaviour, which considers the removal of any photon interacting with the target, corresponds to a narrow beam measurement as visualised in *Figure2.9*. In such measurements, the energy of the beam remains constant, and only the intensity is reduced as scattered photons are excluded. However, in the context of radiation therapy and imaging, it is essential to account for scattered photons in both dosimetric evaluation and image quality assessments. The presence of scattered photons introduces additional complexities that need to be considered to ensure accurate dose delivery and acceptable image quality.
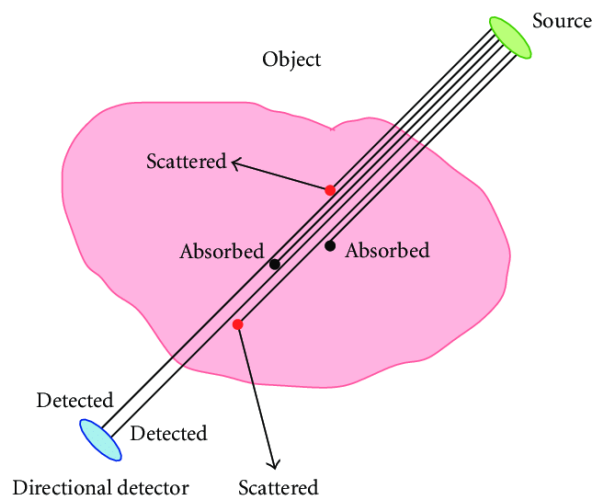

Figure 2.10: Schematic of a narrow beam measurement [23].

The mass attenuation coefficient is a normalisation of the linear attenuation coefficient per unit density of the material to produce a constant value for a given element. As mentioned previously, the probability for a single interaction is quantified through the cross section. Therefore, the mass

attenuation coefficient is the combination of all the partial interaction processes and is characterised as,

$$\frac{\mu}{\rho} = \frac{\sigma_\tau}{\rho} + \frac{\sigma_C}{\rho} + \frac{\sigma_R}{\rho} + \frac{\sigma_P}{\rho} \tag{2.8}$$

Where ρ is the density of the target, and σ_i is the cross section for the mentioned photon interactions. The principal interaction is thus dependent on the ratio of the cross sections and is affected by their proportionality factors. As depicted by *Figure 2.11*, the primary interaction for low energy photons is the photoelectric effect, with Compton scattering dominating the mid-energy section and pair production for high energy photons.
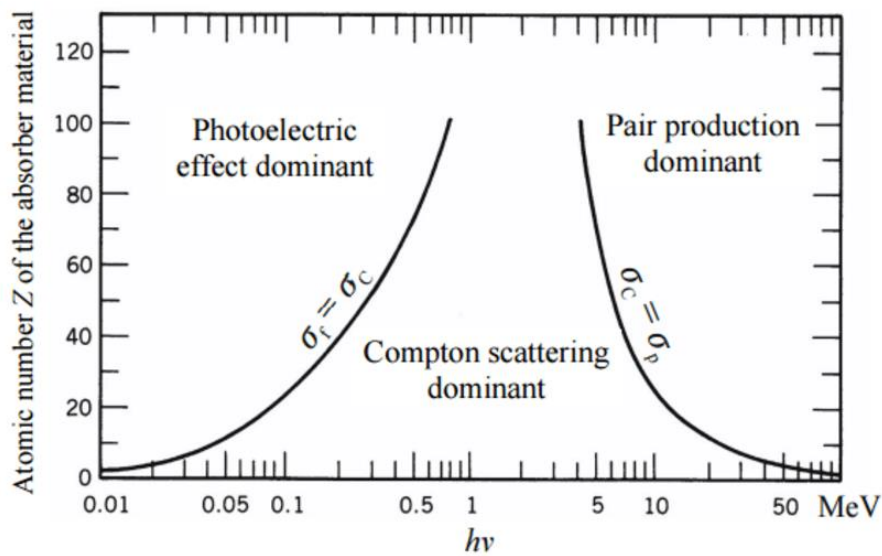
Figure 2.11: Photon beam atomic cross section as a function of photon energy and atomic number of the absorber.

To account for a mixture of atoms in the attenuating material, we can utilise the attenuation coefficient's additive characteristic. Specified by the Bragg's rule, the attenuation coefficient for non-homogeneous targets is defined as,

$$\frac{\mu}{\rho} = \sum_{i=0}^{n} \left(\frac{m_i}{\sum_i m_i} \right) \left(\frac{\mu}{\rho} \right)_i \tag{2.9}$$

Where, m_i is the mass of each constituent. The mass attenuation coefficient of each element is thus normalised by its percentage mass contingent to calculate a cumulative coefficient of the target. The same method can be used to identify the electron density of composite material that is defined as,

$$\rho_e = \rho N_A \sum_i \omega_i \frac{Z_i}{A_i} \tag{2.10}$$

Where ω_i is the normalising sum of the constituents' mass as depicted in equation.

2.2.2 Proton Interactions.

Protons, being charged particles, have the ability to directly ionize and excite the medium which they traverse. In the field of proton therapy, the typical energy range of proton beams falls between 70 and 250 MeV, and these beams are generated using cyclotron or synchrotron accelerators. The interactions of protons with matter can be categorized into two main types, collisions and radiative losses. Understanding both collision and radiative processes is crucial for accurately predicting the behaviour of proton beams in matter. These interactions play a significant role in determining the dose deposition and range of protons in the patient's tissues.
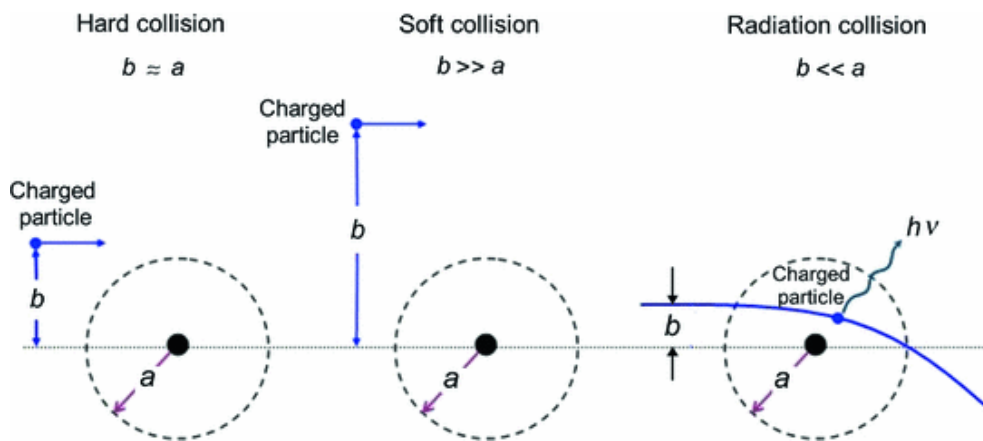

Figure 2.12: Schematic representation of charged particle interactions with an atom. The impact parameter (*b*) indicates the distance of closest approach during the interaction, while the classical atomic radius (*a*) represents the size of the atom [25].

2.2.2.1 Collisional losses.

The collisional losses with matter are dominated by coulombic interactions with electrons rather than the atoms nucleus. The strength of this collision will be determined by the distance between the proton and atom and is further sub-categorised into soft and hard or elastic and inelastic collisions. As illustrated in *Figure 2.12*, the determining factor for the type of collision is defined by the comparison of the impact parameter *b* and the classical atomic radius *a*.

Elastic Collisions

For Elastic collisions, the main assumption made is that the electron is stationary, thus the total energy of the interaction is governed by the incident proton. As with the photon interactions, we should analyse the angular differential cross section of elastic collisions to gain an insight on the probability of the scattered protons angular distribution.

$$\frac{d\sigma}{d\Omega} = \frac{Z^2}{4} \frac{r_e^2 c^2 m_e}{\beta^2} \frac{1}{sin^2(\Theta)}$$

(2.11)

Where, r_e depicts the distance to the electron, β is the proton velocity normalised by the speed of light and Θ is the deflection angle of the proton. The cross section, as depicted in equation (2.11), exhibits a proportional relationship to Z^2, indicating that higher atomic number targets and, consequently, higher electron densities significantly increase the probability of interaction. Moreover, considering the electromagnetic nature of particle interactions, the velocity of the incident proton determines the timescale of the interaction. A slower velocity results in a longer interaction time, leading to an increased cross section, as denoted by the $1/\beta^2$ factor in the equation. Furthermore, the factor of $1/sin^2\Theta$ signifies that protons tend to scatter at small angles with minimal energy transfer. This behaviour arises from the substantial mass difference between the proton and the electron it interacts with.

Of significance is also the energy transfer spectrum for elastic collisions that can be obtained by differentiating the cross section with the transferred energy. The energy differential cross section is proportional to $1/E^2$, however as indicated in Figure *2.13* this behaviour ceases to exist for low energy transfers. The drop is governed by quantum mechanics as the proton has to either ionise or excite the atom in order to interact with it which insinuates a minimum but non-zero energy $E_{min.}$
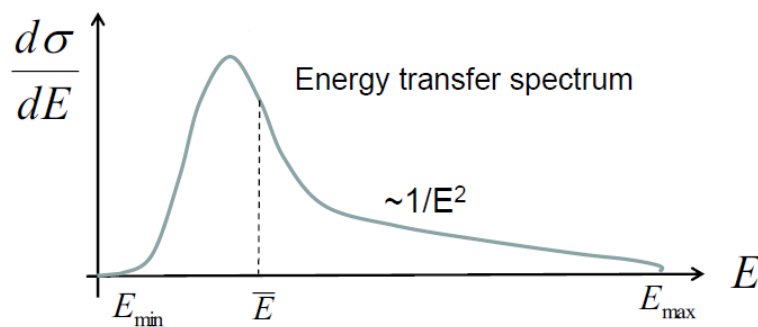
Figure 2.13: Energy transfer spectrum for proton collisional interactions [19].

2.2.2.2 Collisions Stopping power.

Another crucial property to consider in proton interactions is the stopping power, which quantifies the energy loss per unit length as a charged particle travels through a medium. The stopping power depends on both the charge and velocity of the projectile, as well as the properties of the target material. The total stopping power is defined as,

$$S = n_v \int_{E_{min}}^{E_{max}} E \frac{d\sigma}{dE} dE$$

(2.12)

Where n_v is the number of electrons in the medium and E is the energy transferred from the interaction.

Soft Collisions

Soft collisions as illustrated in *Figure 2.12* occur when the proton interacts with the atom at a large distance. These collisions are considered inelastic, predominantly leading to excitations of the atom with some minor ionisations. The energy transfer during soft collisions is relatively small and falls within the range between E_{min} and $\bar{E}$. This type of interaction is the primary interaction that occurs when protons transverse through matter. The resulting stopping power can be described by the Bethe formula, which accounts for the energy loss of the proton per unit length and is defined as,

$$\frac{S_{c,Soft}}{\rho} = \frac{N_A Z}{A} \frac{2\pi r_0^2 m_e c^2}{\beta^2} \, ln[2m_e c^2 \beta^2 H - \beta^2 I^2 (1 - \beta^2)]$$

(2.13)

Where N_A is the Avogadro's number, A is the atomic number and $N_A Z/A$ described the number of electrons per gram in the medium. Additionally, I is the mean excitation potential which reflects the binding energy of the structure and is the amount of energy required to raise the energy level of an electron, while H is the maximum energy transfer by soft collisions.

Hard Collisions.

For hard collisions, the proton passes through the atom with the impact parameter being approximately equal to the atom radius. These interactions are not as prominent as soft collisions but lead to a higher energy transfer in the range of $\bar{E}$ to E_{max}. They may be considered elastic collisions between free particles as the binding energy is negligible compared to the incident proton energy. The stopping power for hard collisions is described by,

$$\frac{S_{c,Hard}}{\rho} = \frac{N_A Z}{A} \frac{2\pi r_0^2 m_e c^2}{\beta^2} \left[ln \left[\left(\frac{E_{max}}{H} \right) - \beta \right] \right],$$

(2.14)

Where H is the minimum energy transferred by hard collisions while the first part remains the same as the soft collisions.

Total Collisional Stopping Power

Total stopping power resulting from collisional losses can be derived by the summation of the two interactions. Therefore, the total stopping power is estimated by,

$$\frac{S_c}{\rho} = \frac{S_{c,Soft}}{\rho} + \frac{S_{c,Hard}}{\rho} = \frac{N_A Z}{A} \frac{2\pi r_0^2 m_e c^2}{\beta^2} \left[ln \left[\left(\frac{2m_e c^2 \beta^2}{(1 - \beta^2)I} \right) - \beta^2 \right] \right],$$

(2.15)

An important observation from the collisional stopping power depicted in equation 2.15, is that it is directly proportional to the square of the atomic number Z, indicating a stronger interaction with

higher atomic number materials. Conversely, the collisional stopping power decreases with the square of the proton velocity and the mean excitation potential of the target material. Therefore, as the proton loses energy and consequently slows down while traversing through the medium, the collisional stopping power increases significantly.

2.2.2.3 Radiative Losses.

Radiative interactions, also known as Bremsstrahlung, involve the emission of a photon when a charged particle undergoes acceleration in the presence of the magnetic field of an electron or nucleus. The radiative power can be derived using Larmor's frequency from classical electromagnetism. However, it is important to note that for heavy particles such as protons, radiative interactions are not significant compared to their interactions with atomic electrons. Electrons, on the other hand, experience prominent radiative interactions. While we will not focus on radiative interactions in the context of proton interactions, they should ne taken into consideration for electrons as they play a crucial role in the production of high-energy X-rays utilised for imaging and radiotherapy.
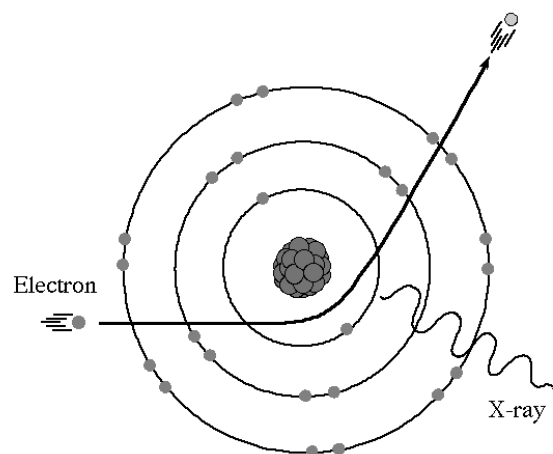
Figure 2.14: Schematic representation of charged particle radiative losses [26].

2.2.2.4 Nuclear Interactions

Nuclear interactions are inelastic processes where high energy protons can excite the nucleus resulting in the scattering of the primary proton and the emission of a neutron, proton, or an alpha-particle. It is important to note that for a proton to excite the nucleus, a significant amount of energy is required. Consequently, nuclear interactions are not prominent for proton energies below 10 MeV. However, as mentioned in section 2.2, the initial proton energies in proton therapy are sufficiently high to induce nuclear interactions, leading to the generation of additional protons in the beam. The

probability of these nuclear interactions is proportional to the proton energy, and therefore, they are more likely to occur at the initial stage of the beam path where the proton energies are highest.

2.2.2.5 Proton Range

The projected range of charged particle is characterised by the expectation value of the largest depth it can transverse through matter along its incident direction. For heavy charged particles like protons the projected range will be approximately equal to the actual range as protons experience minor scattering angles.
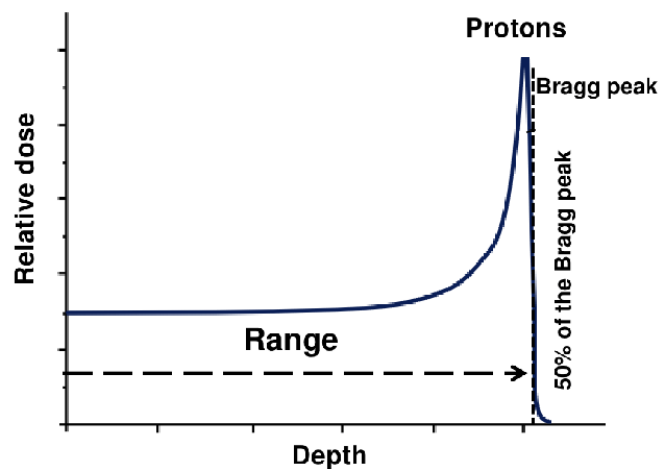
Figure 2.15: Visualisation of the energy deposition as a function of depth curve of a proton beam [27].

As indicated by *Figure 27*, protons deposit the majority of their energy at the end of their path at the so-called Bragg Peak. As discussed in the stopping power section, as the proton travels through the medium it loses energy through collisions losing energy and slowing down. This generates an avalanche effect as the lower the proton velocity the higher the stopping power, resulting to a naturally high energy deposition at the end of its path. The width of the Bragg peak is proportional to the variations in energy deposition along the beam path and is defined as beam straggling. Lastly, the range of the proton beam depends on the initial energy of the protons as well as the electron density and mean excitation of the absorber as discussed above. In proton therapy, we have information for the latter from the CT images therefore by altering the incident beam energy we can accomplish a very localised dose deposition.

2.3 Radiation Therapy

Radiotherapy is the use of ionising radiation to control or kill malignant cancer cells. Damage in radiotherapy arises from the effect of radiation on the DNA. Other parts of the cell such as the proteins and enzymes will also be damaged, but only damage to the DNA is considered to be lethal and/or cause mutations.

2.3.1 Radiobiology

Radiation damage is classified into three categories; *lethal* when the damage is irreversible and will lead to cell death, *potentially lethal* when damage can become lethal if not repaired on time and *sublethal* when under normal circumstances can be repaired but given another sublethal damage could lead to accumulative lethal effect. For an interaction to be lethal, an asymmetric DNA damage is required where both DNA strands brake. In the case of a single strand brake, the opposite strand could be used as a template for repair. However, two separate single strand interactions can also induce cell death if they are close in time and space.

To quantify cell survival curves the *Linear-Quadratic Model* (LQ) is utilised where both effects are taken into consideration. Both incidents are described by Poisson statistics and the main assumption of the model is that the cell is inactive when both DNA strands are damaged. The overall LQ equation is defined as,

$$S = e^{-\alpha D - \beta D^2}$$

(2.16)

Where S is the surviving cell fraction with α and β depicting the average probability per unit dose that a single-particle or two particle interaction induces a double strand brake respectively. Of special interest is the dose at which the log-surviving fraction of both processes are equal. The α/β ratio represents the curviness of the survival curve portrayed in *Figure 2.16* with a higher ratio indicating a more linear relationship. Such cells like tumors exhibit considerable irreparable damage and are classified as early responding tissues. While low α/β ratio cells like healthy tissue depict a high capacity for repairs and are classified as late responding tissues. By inspecting *Figure 2.16* we can identify that there is a small "window of opportunity" at low doses where late responding cells have a higher surviving fraction than early responding tissues [28]. Therefore, there is a significant therapeutic gain when utilising dose fractionation instead of depositing all the dose at the same time.

By allowing time for full repairs to occur between fractions we minimise damage to healthy tissue while maintaining significant tumor damage. As the α/β ratio varies significantly depending on tumor and surrounding reacting tissue the fractionation schedule is dependent on the type and location of the tumor. A conventional fractionation schedule is one treatment depositing around 2Gy per day for 5 days a week. Hyper-fractionation where dose per fraction is less than 2Gy is commonly used for head and kneck cancers, while hypo-fractionation where dose per fraction is greater than 2Gy is commonly utilised for prostate and breast cancers [29,30].

Fractionated radiotherapy offers an additional advantage in terms of tumor oxygenation. Tumors often exhibit chaotic structures, resulting in the presence of hypoxic (low oxygen) regions within the tumor. These hypoxic regions arise due to limited blood supply, with inner cells being more distant from blood vessels compared to outer cells. It has been extensively demonstrated in various studies that hypoxic cells are more resistant to radiation compared to well-oxygenated cells [31]. This increased radio resistance is attributed to the ability of oxygen molecules to fix the damaged DNA and inhibit its repair processes. In fractionated radiotherapy, the presence of multiple treatment sessions with intervals between them allows for tumor re-oxygenation to occur and subsequently decrease the radio resistance of tumour cells.
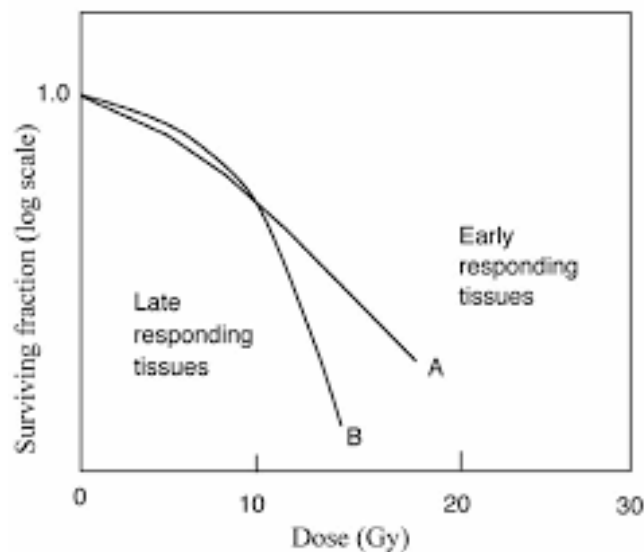
Figure 2.16: Illustration of surviving fraction curves for early and late responding tissues acquired from the LQ model.

2.3.2 Linear Energy Transfer and Relative Biological Effect.

The quantity that characterizes the energy deposition of incident radiation in a unit mass of tissue is known as absorbed dose, which is measured in Gray (Gy). However, different types of radiation interact with matter in distinct ways, leading to variations in the distribution of deposited energy along their paths. To facilitate this variation, the concept of Linear Energy Transfer (LET), which quantifies the amount of energy deposited per unit length as the radiation traverses a material is employed in radiation dosimetry. High-energy heavy charged particles, such as protons and alpha particles, exhibit a high LET as they deposit a significant portion of their energy in a close proximity to their tracks. In contrast, low-energy X-rays possess a lower LET value. When these X-rays interact with tissue, they generate secondary electrons that exhibit more erratic trajectories and deposit energy further away from the primary beam path.

A higher LET instigates a more direct damage to the DNA as the energy deposition is more compact, significantly increasing the probability of a double DNA strand brake. Therefore, to accumulate an identical effect with a low LET particle beam, a higher dose is required as indicated by *Figure 2.17*.
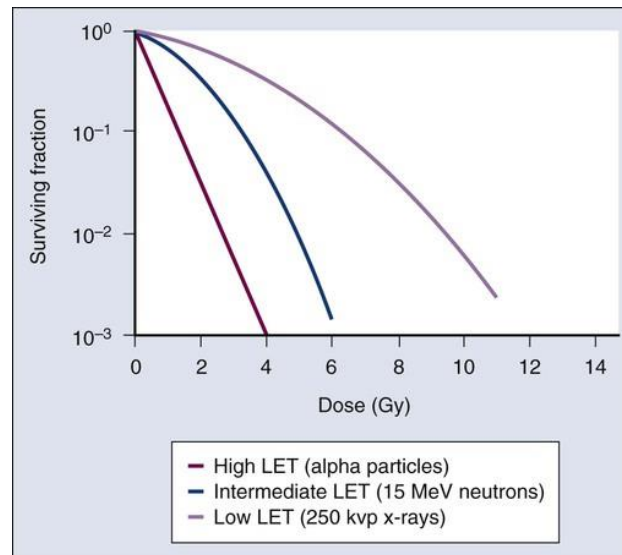

Figure 2.17: Dose response curves for radiation of varying LET [32].

To compare the biological effects of radiation with different qualities, such as the Linear Energy Transfer (LET), it is necessary to define the Relative Biological Effectiveness (RBE).RBE is defined as the ratio of iso-effective dose of two radiation types. For purpose of computing the equivalent dose accumulated by an organ or tissue we can utilise a radiation weighting factor W_R, as stated by the International Commission on Radiological Protection 2007 (ICRP) [33]. The radiation weighting factors convert the absorbed dose measured in Gy to biological equivalent dose in sieverts (*Sv*) with reference the 250 kV x-rays with weighting of unity. In the ICRP 2007 a scaling factor of 2 is stated for protons, however, in a clinical environment a more conservative and constant factor of 1.0-1.1 is utilised [34]. Several studies demonstrated experimentally that the RBE of protons varies depending on several biological and physical quantities with ongoing research on the development of variable RBE dose conversion [35]. The doses stated in this study are defined as Gy(RBE) reflecting the absorbed dose multiplied with an RBE scaling factor of 1.1.

2.3.3 Photon vs Protons

As discussed in section 2.1, photons interact with matter indirectly. The incoming photons will thus deposit energy to generate free radicals, fast-moving secondary particles like electrons which in turn will damage the DNA. The depth dose curve for photons is determined by the Kinetic Energy Release per Mass (KERMA) and is defined as the expectation value of the energy transferred per unit mass in

a point. KERMA accounts both for collisional and radiative losses, with the beam energy losses in radiotherapy primarily being governed by collisions as Compton scattering is the primary interaction for the utilised photon beam energies. *Figure 2.18* depicts a photon depth dose curve example where we can inspect an inverse exponential behaviour similar to the photon attenuation graph from section 2.1.5. At low depths the absorbed dose is low as the photon beam needs to ionise the medium to generate the free radicals that deposit energy. The deposited dose increases in the build-up region up to a maximum point where the depth dose curve follows the KERMA predictions. Protons on the other hand directly ionise the medium and instigate DNA damage. Additionally, as discussed previously protons' deposit most of their energy at the end of the path at the so-called Bragg peak as visualised in *Figure 2.18.*
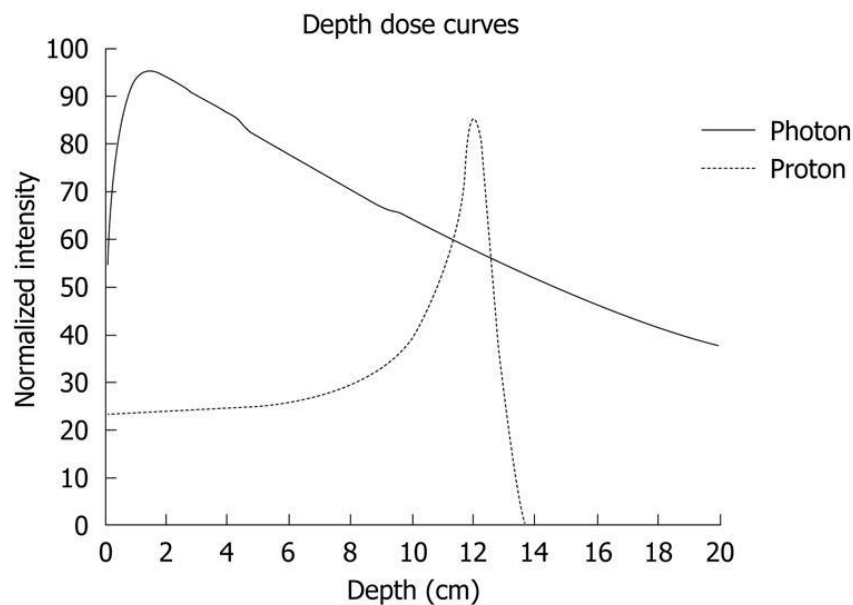

Figure 2.18: Proton depth dose curved for a proton and photon beam [36].

By comparing the two depth dose curves we can infer that protons have a much more localised dose deposition and a zero-exit dose. The proton beam energy can be adjusted such that the Bragg peak is located within the tumor boundaries with almost no dose delivered behind the tumor. Secondary particles generated from the proton beam as well as beam straggling will extend the depth dose curve of the proton beyond the tumor, but the dose is significantly less than that of a photon beam. This effect is most prominent in lung cancer cases where the secondary electrons have a notably higher range compared to other organs in the human body. Additionally, the more localised dose distribution from protons enables the treatment planner to significantly reduce dose to surrounding organs at risk, while maintaining a comparable tumor dose coverage. In *Figure 2.19* we can observe a comparison of a proton and photon beam treatment plan for a lung cancer patient. By examining the isodose lines we can see that the proton plan significantly reduces dose to organs at risk and minimises the low dose regions in the lungs. Dose distribution to the heart, esophagus and lungs was significantly lower for the proton plans as reported from the depicted study [37]. A lower dose and irradiated volume of organs at risk drastically reduces organ toxicity complications improving the treatment outcome.

The localised dose from protons however comes with certain disadvantages that need to be accounted. Proton transport in tissue is sensitive towards anatomical changes that can occur both throughout the duration of the treatment, *interfractional* or during the dose delivery *intrafractional.* Interfractional motion are changes in anatomy during the fractionated course of the treatment where the planned energy and fluence distribution of the proton beam may not be sufficient to provide the desirable tumor coverage. Such changes transpire gradually, occurring over days, weeks or even months and can be assessed by repeat CT scans with plan adaptations occurring when necessary. Intrafractional motion is anatomical changes occurring during the delivery of radiation and are induced mainly by respiration. Intrafractional motion describes the movement of the tumor, organs, and bone structures within the thorax region in the case of lung cancer. These fast alterations are even more challenging to handle in proton therapy than conventional radiotherapy due to the aforementioned proton sensitivities and will lead to plan degradation if not accounted for.
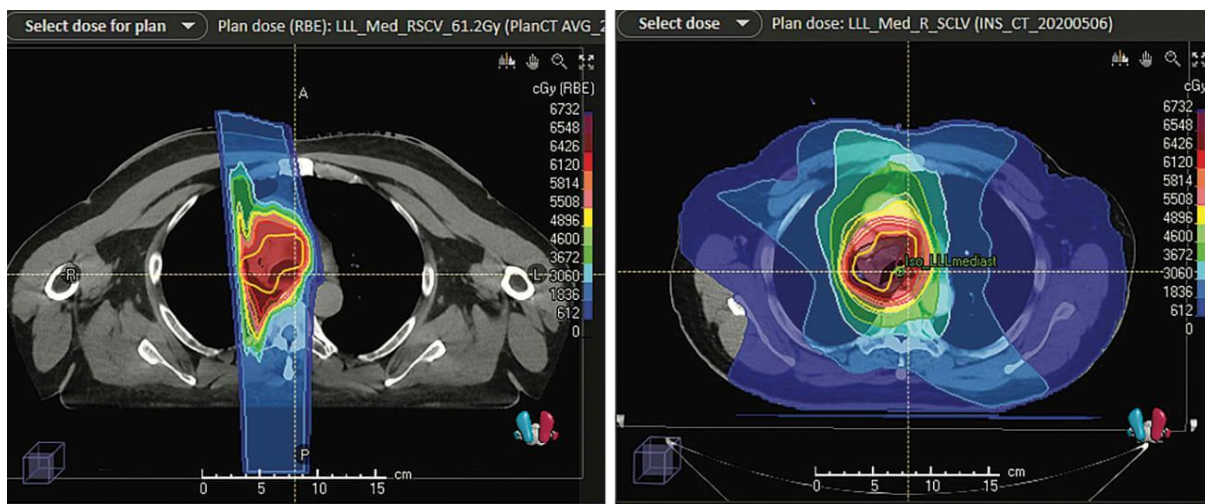
Figure 2.19: Comparison of an Intensity Modulated Proton Therapy (IMPT) treatment plan on the left and Intensity Modulated Radiation Therapy (IMRT) treatment plan on the right for a lung cancer patient [37].

2.3.4 Proton Therapy Treatment Modalities.

Currently in proton beam therapy, there are two prominent and clinically utilised radiation delivery techniques that we can implement for lung cancer patients. First is Passive Scattering Proton Therapy (PSPT) and second is Intensity Modulated Proton Therapy (IMPT) utilising an active Pencil Beam Scanning delivery system.

Passive Scattering Proton Therapy

In PSPT, as illustrated in *Figure 2.20*, a single or double scattering can be utilised to spread out the proton beam into a uniform beam laterally. For lower uniform field sizes, single scattering may be

employed, while a double scattering system is needed for greater uniform field sizes. The radiation field that impinges on the patient can then be shaped by lateral collimation of the beam's edges. Additionally, patient specific range compensators have to be manufactured in order to shape the field according to tumor geometry and beam orientation. The beam energy can change over time thanks to a rotating range modulator wheel, which causes the protons' energies to fluctuate. The resulting dose distribution is a spread-out Bragg peak. Although the various energies are not all delivered at once, they are all delivered within the range modulator wheel's single cycle, which rotates at a typical frequency of 10 Hz. As a result, the temporal variance of the energy delivery system is substantially lower than that of a typical breathing cycle.
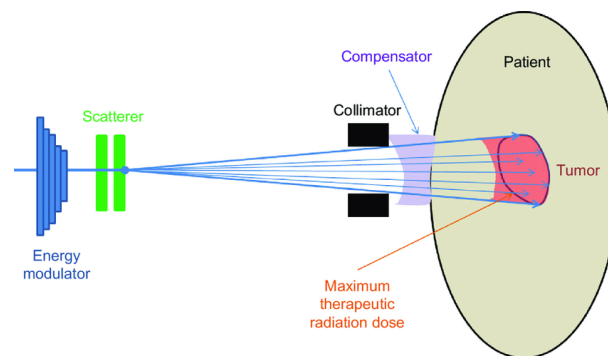
Figure 2.20: Schematic illustration of passive scattering delivery system of proton therapy [38]

Active Scanning Proton Therapy

In pencil beam scanning, focused beams of protons of varying energy and intensity are magnetically scanned across the field. This technique enables the proton beam to be directed precisely so that the energy is deposited at an exact desired spot in the tumor. By superimposing dose from several spots within the tumor boundaries, a homogeneous radiation dose can be accomplished. This scanning technique enables the delivery of this conformal dose without the need of extra apparatus. Brass apertures are not necessary as the treatment field's lateral extent can be preserved by selecting the right spot locations. Additionally, since the energy can be controlled, it eliminates the need for field-specific range compensators and allows the resulting beams to conform to the proximal and distal shapes of the target.

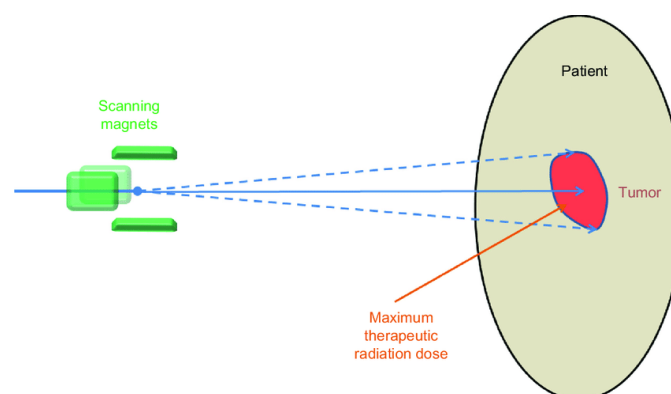Figure 2.21 Schematic illustration of an active scattering delivery system of proton therapy [38]

Intensity modulated proton therapy is the preferred method by many clinical institutions and the one we will be using in this study for several reasons. First, the need for field-specific hardware makes PSPT more expensive, time consuming and resistant to plan adaptations. In cases of lung cancer, it has been reported that tumor and patient anatomical geometry can be significantly altered within the treatment period [39]. This instigates the need for new range compensators to be generated for the same patient, making the adaptive capabilities of PSPT more complicated. On the other hand, the lack of patient-specific apparatus for IMPT, enables the treatment planner to make adaptive alterations on a more frequent basis than with PSPT to ensure a more accurate dose delivery to the patient. Additionally, several studies indicated that pencil beam scanning not only improves dose distribution to the target but also reduces dose to healthy tissue when compared to both PSPT and IMRT [40,41].
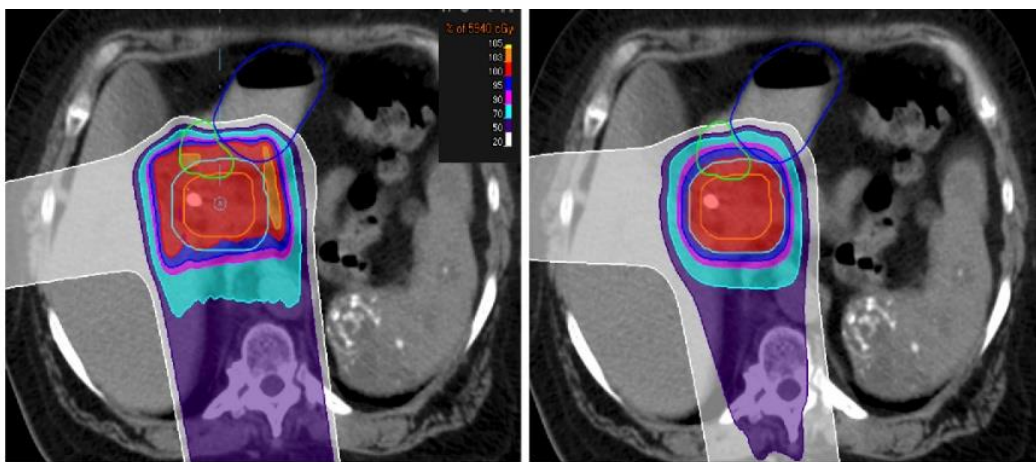
Figure 2.22: Dose distribution of PSPT plan (left) and IMPT plan (right) for a pancreatic cancer patient. Volumes presented by the study were IGTV in orange, ICTV in cyan, duodenum in green and stomach in blue [42].

2.3.5 Imaging in Radiotherapy.

Medical imaging plays an essential role in radiotherapy both for diagnosis and treatment planning purposes. The advancement of treatment planning was greatly aided by the discovery of computed tomography (CT). CT is still the most prominent three-dimensional imaging modality utilised for dosage computation, despite certain drawbacks. Secondarily employed in the treatment-planning process are more recent image modalities like positron emission tomography (PET) and magnetic resonance imaging (MRI) [43]. When compared to CT planning alone, MR improves tumour definition due to its superior soft tissue contrast and resolution. With the rise of MR-Linacs in recent years several transformation tabulated data have been identified that enable the extraction of electron density information from the image. Utilising this dose calculations can be performed through MRI images, though, they are solely implemented on x-ray radiotherapy [44]. In addition to anatomical information from CT and MR, metabolic data is also provided by PET. We can identify biological characteristics of the tumours non-invasively by administrating various radiolabelled chemicals. From the PET images we can identify biologically active regions of the tumor enabling the prevention of

irradiation of tissues that do not contain tumor cells such as atelectasis for lung carcinoma, which could not be detected by CT or MRI. Additionally, response adapted therapy could be pragmatized with alterations of the target volumes during treatment from PET information [45].

Imaging of organs in the thorax area where respiration induces motion, four-dimensional CT (4D-CT) scans can be incorporated. Utilising external respiration tracking apparatus, several images can be acquired and binned into respective breathing phases. A series of 10 3D-CT scans is reconstructed where each scan represents a phase in the breathing cycle of the patient.

Lastly, imaging is used to ensure that patient positioning is consistent and in accordance with the planning image and treatment machine coordinate system for each fraction. All photon and proton delivery systems include an orthogonal X-ray radiograph system, where most of them have gantry-mounted onboard scanners that can be used for cone beam CT (CBCT) acquisition. For lung cancer treatment CBCT is most frequently used, where in addition interfractional anatomical changes can be identified [46].

2.4 Computed Tomography

The fundamental principle underlying Computed Tomography (CT) scans involves mathematically transforming a collection of measured two-dimensional projections into a three-dimensional image. The CT scan employs a rotating gantry housing an anode and a detector array, which allows for rapid and accurate image acquisition from multiple angles. Similar to X-ray projection systems, the CT scan gathers 2D back projections of the target. However, through techniques such as filtered back-projection and iterative reconstruction, as illustrated in *Figure 2.23*, the acquired information can be processed to generate a three-dimensional image.
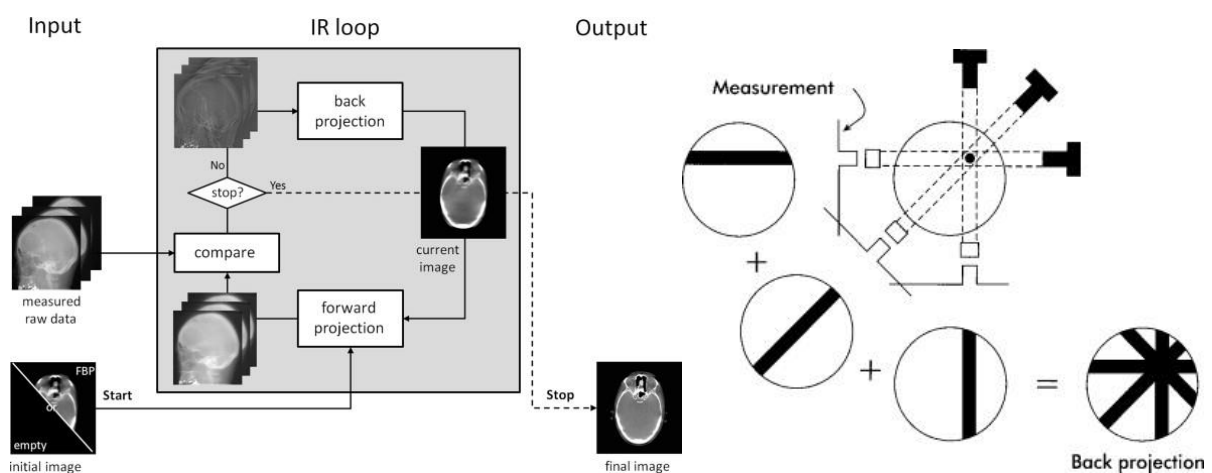

Figure 2.23: Schematics of CT reconstruction techniques with Iterative Reconstruction on the left [48] and Back Projection on the right [47].

2.4.1 X-ray Production and Hounsfield Units

The generation of X-rays in a CT tube is achieved through the phenomenon of radiative losses, as explained in section 2.2.3 , and the radiation produced is comparable to that from an X-ray projector. Electrons are liberated by thermionic excitations of the cathode filament and then accelerated towards the direction of the anode as depicted in *Figure 2.24*. Bremsstrahlung and characteristic radiation are released as a result of the interactions between the electrons and the anode.
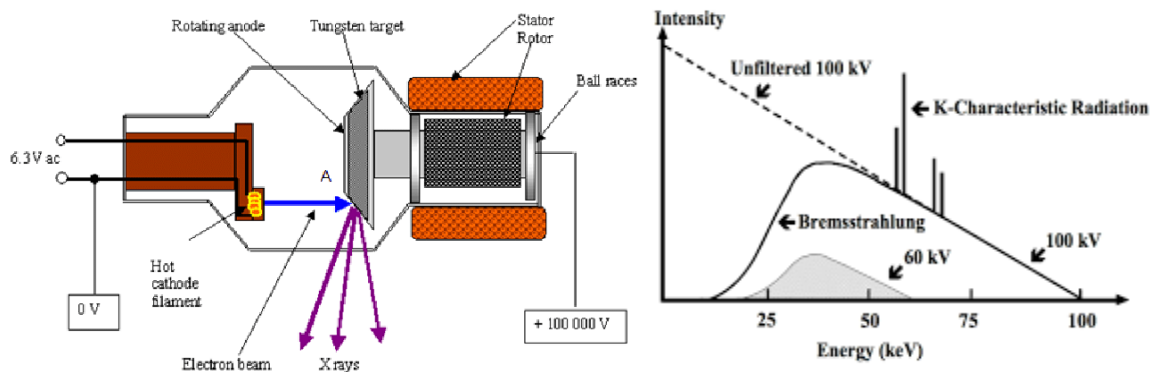
Figure 2.24: Schematic of an X-ray gun on the left [49] and visualisation of the unfiltered and filtered photon energy spectrum generated from the X-ray gun on the right [50].

The unfiltered energy fluence of the generated photon spectrum is described by Kramer's rule. As the electrons traverse through the anode and they are attenuated, the beam energy decreases with depth. As a result, generated photons from higher penetrating depth electrons are observed with a lower energy. Kramer's rule depicts a triangular spectrum weighted towards lower energies and is defined as,

$$\Psi_{hv} = KZ(hv_{max} - hv) \tag{2.17}$$

where, *K* is a proportionality constant, *Z* is the atomic number of the absorber and hv_{max} and hv are the maximum and current photon energy of the beam. Visualised in *Figure 2.24* is the unfiltered bremsstrahlung spectrum in comparison with a measured spectrum example. By comparison of the two, we can infer that characteristic radiation is not included in the Kramer's spectrum and that low energy photons are not present in the output field. As lower energy photons are not able to penetrate the human body, they do not affect image quality but only increase the dose received by the patient. Attenuating materials placed in front of the beam in conjunction with the CT tube casing, absorb these low energy photons.

The photon energy spectrum is described by the maximum photon energy and is within the range of 70 - 150KeV. For diagnostic purposes the photon energies used are relatively low so as the dominant photon interaction to be the photoelectric effect. As stated earlier, the cross section of the photoelectric effect is proportional to the atomic number cubed Z^3, resulting in a significant contrast

between air, soft tissue, and bones. Additionally, certain tissues may exhibit the same x-ray attenuation at one energy level but differ at another. To address this, dual-energy CT scans can be employed to differentiate between such tissues, thereby enhancing the diagnostic capabilities of CT imaging. However, for proton therapy treatment planning, the single-energy CT remains the standard imaging method.

.
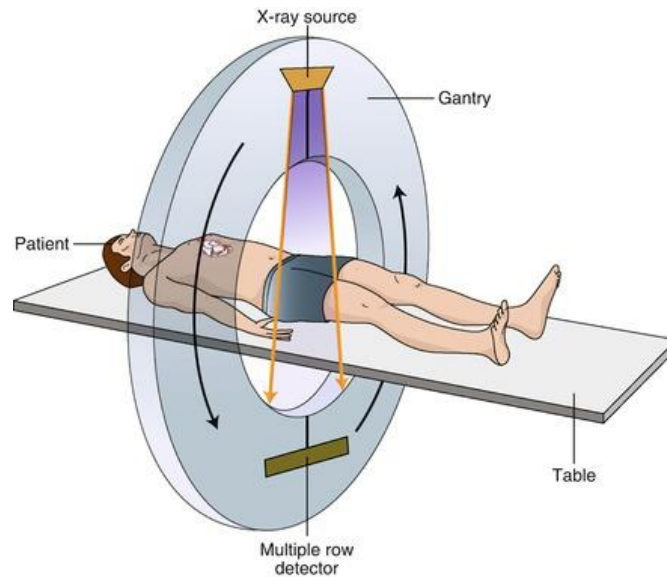
Figure 2.25: Schematic illustration of a CT scan [51]

During the rotation of the gantry around the patient, the patient is simultaneously translated through the gantry opening to capture images of the targeted region as visualised in *Figure 2.25.* The resulting reconstructed image is a three-dimensional matrix, composed of multiple axial scans with set pixel spacing and slice thickness. Each voxel in the CT represents the degree of attenuation experienced by the x-ray beam as it traverses through the tissue, and this attenuation is quantified through the Hounsfield Units (HU). The CT voxel numbers establish a correlation between the attenuation coefficient of the medium/voxel and that of water. These voxel numbers are thus defined as,

$$HU = \left(\frac{\mu_v - \mu_W}{\mu_W}\right) \times 1000 \qquad (2.18)$$

Where μ_v is the attenuation coefficient of the voxel and μ_w is the attenuation coefficient of water. Air registers at a HU value of -1000, while dense bone registers at +1000. Soft tissues can be distinguished from one another by their HU values, which fall within this range and include the HU values of organs, muscle, and fat. CT scans are typically portrayed in grayscale where the colour of the voxel is based on the HU value where black represents -1000 and white 1000.

2.4.2 Four-Dimensional CT scan.

As described in section 2.3, when imaging moving regions such as the thorax, a 4D CT scan can be utilised to capture the dynamics of intrafractional motion. In a 4D scan, multiple images are acquired over time, enabling a sequential playback of the scan as a video. This approach allows for the observation of physiological processes and the tracking of internal movements, providing valuable insights into the dynamic behaviour of the imaged region.

The unprocessed image projection data are thus acquired while the patient is in free breathing. Image reconstruction is then retrospectively gated according to recorded phase information acquired from an external respiration signal. An extensive camera system in conjunction with a marker block placed on the chest of the patient is used to acquire the respiratory information. This information is subsequently used to bin the raw data with a time-based phase sorting technique. To ensure that the patient breathes at a consistent period, audio-visual feedback can be used to guide the patients breathing during image acquisition. *Figure 2.26* portrays an image of the marker block on the left and a camera system illustration on the right. The camera system is portrayed in a Linac set-up; however, it would be the same during image acquisition on the CT scanner and during radiation delivery of the proton beam.

Figure 2.26: Illustration of the Real-time Tracking and Motion Management system from Variant on the right and picture of the maker block on the left [51]

The resulting 4D image comprises of ten 3D scan, where each scan represents a specific phase in the respiratory cycle of the patient. The first phase, referred as phase 0% , corresponds to the end of inhalation, while phase 50% represents the end of exhalation. *Figure 2.27* provides a visualisation of the breathing curve, depicting the corresponding scans at each time point along the respiratory cycle.
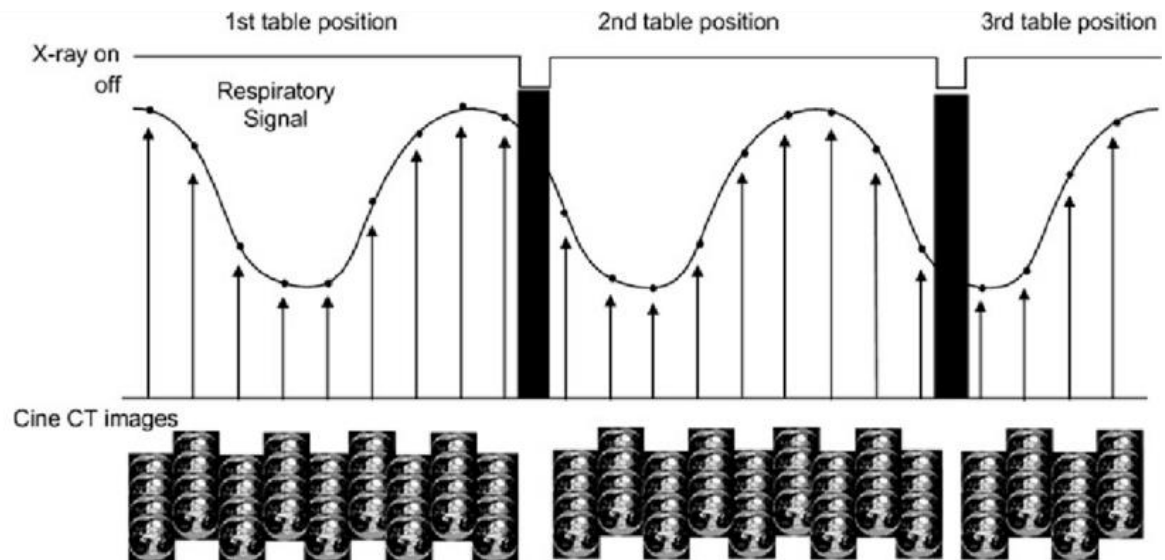
Figure 2.27: Breathing curve and CT images binned along the respiratory cycle to generate 4D CT [52].

2.4.3 4D Scan Representations

In radiation therapy, both for treatment planning and quality assurance procedures in thoracic regions, a 3D representation of a 4D CT scan can be generated. Treatment planning involves constructing a plan based on a 3D snapshot representation of the body at a specific point in time. By utilising a CT scan reconstructed from all phases of the breathing cycle, we can incorporate the effects of intrafractional motion in the planning process. Among the various multiplanar reconstructed scans, the three most prominently used are the Average Intensity Projection (AIP), the Maximum Intensity Projection (MIP), and the Minimum Intensity Projection (MinIP). These techniques aid in visualising and analysing the intensity characteristics of the imaged structures.
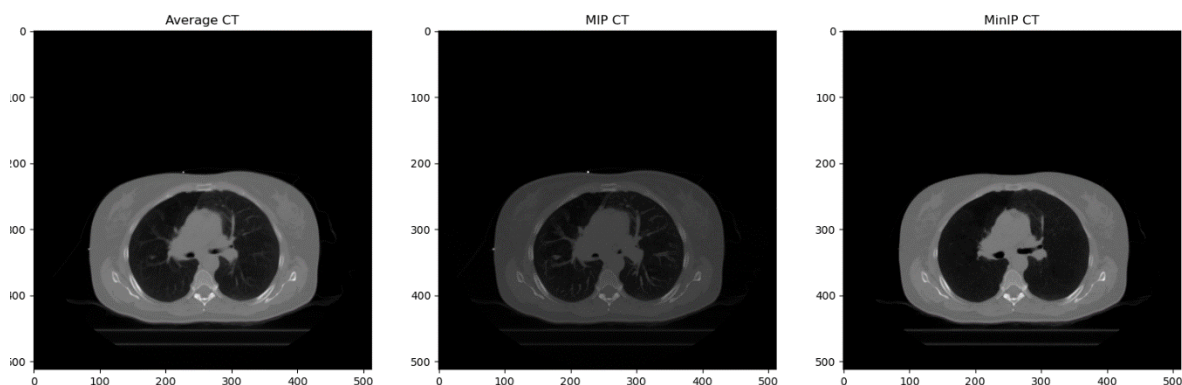
Figure 28: Visual representation of the AIP (left), MIP (middle) and MinIP(right) constructed scan for

The Average Intensity Projection (AIP) displays the average attenuation of all voxels at a specific location (index). The resulting AIP scan appears smoother, with some blurring occurring in areas affected by motion, such as the ribs. Previous studies have shown that AIP is a suitable representation

planning CT for proton therapy, with minimal variations between planned and delivered dose distributions [53].

On the other hand, the Maximum Intensity Projection (MIP) portrays the voxel with the highest attenuation in a given index. This technique enhances high-attenuation structures like bones or blood vessels, especially when contrast media is administered. However, MIP plans tend to exhibit poor 4D target coverage for treatment planning due to the conservative density estimation along the proton beam path [8]. As the MIP emphasises the voxel with the highest attenuation, the estimated stopping power is overestimated, leading to observed iso-dose lines shifting distally when evaluating the plan across the entire breathing cycle. While the MIP is not ideal for treatment planning, it is commonly used for structure delineation [54]. It provides clear identification of thoracic bone structures and lung tumors, but if the tumor and background have similar Hounsfield Unit (HU) values, the tumor may not be well-defined. Consequently, when dealing with tumors near the chest wall or overlapping with the diaphragm, the MIP scan alone may be insufficient, and corrections need to be made as depicted in *Figure 2.29* [55].

In contrast, the Minimum Intensity Projection (MinIP) displays the voxel with the minimum attenuation in a given index. This projection method is useful for detecting low-density, low-contrast structures within a volume. While it can be utilised to identify cystic lung diseases and bronchial dilation in thoracic scans, it is primarily employed for liver and pancreas scans [57]. Similar to the MIP scan, the MinIP is not an optimal representation for treatment planning, as the observed iso-dose lines tend to shift proximally.
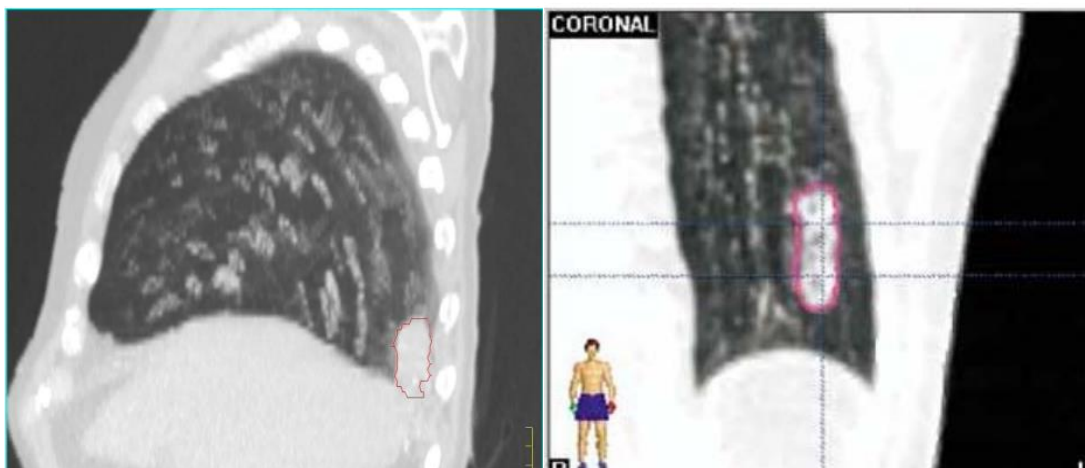
2.29: Illustrations of MIP projection scans of lung cancer patients [56].

2.3.4 Hounsfield Look-Up Table

As discussed previously, CT voxel value is a representation of the voxel's photon attenuation with respect to the attenuation of water. For the purposes of proton beam therapy however, since the interaction mechanisms of the two radiation types vary, a conversion from HU to proton Relative Stopping Power (RSP) needs to be performed. From section 2.2 we can identify that there is no direct

physical relation between the two processes. However, they both exhibit a linear dependency with the relative electron density of the medium. An accurate calibration of the CT scan to acquire relative electron density values can be achieved through a stoichiometric calibration as described by Schneider et al [58].

Stoichiometric calibration is a method to determine CT calibrations for biological tissue based on measurements of tissue equivalent materials. For low energy photons used in diagnostical imaging, an accurate parameterisation of the cross-sections was derived by Rutherford where he defined the attenuation coefficient as,

$$\mu = \rho N_g(Z, A)[K^{ph}Z^{3.62} + K^R Z^{1.86} + K^C Z] \tag{2.19}$$

Where K^{ph}, K^R and K^C are constants characterising the cross-sections of the photoelectric, Rayleigh and Compton interactions, Z it the atomic number of the attenuator and ρN_g described the electron density of the medium [59]. The energy dependence factor of each interaction is included in the coefficients with pair production being excluded as we only consider low energy photons. The ratio of the effective attenuation coefficients of compound materials and water can be expresses as,

$$\frac{\mu}{\mu_w} = \frac{\rho}{\rho_w} \frac{\sum_i \frac{\omega_i}{A_i}\left(Z_i + k_1 Z_i^{2.86} + k_2 Z_i^{4.62}\right)}{\left(\frac{\omega_H}{A_H}\right)(1 + k_1 + k_2) + \left(\frac{\omega_0}{A_o}\right)(8 + k_1 8^{2.86} + k_2 8^{4.62})} \tag{2.20}$$

Where the denominator reflects the attenuation of water based on its chemical composition of hydrogen and oxygen. This ratio is commonly referred in literature as the "reduced HU". Utilising the electron density for a mixture of molecules described in equation (2.10), the relative electron density of the material with respect to water can be inferred as,

$$\widehat{\rho_e} = \frac{\rho \sum_i \omega_i \left(\frac{Z_i}{A_i}\right)}{\rho_w (\omega_H \frac{Z_H}{A_H} + \omega_O \frac{Z_O}{A_O})} \tag{2.21}$$

Combining equations (2.21), (2.20) with the HU equation (2.18), one can infer that the CT number depends linearly on the relative electron density, with a proportionality constant σ.

By determining the relative electron densities of various tissue substitutions, taking into consideration their chemical composition, one can identify the proportionality constant σ for the specific CT scan. Since the characterisation of each CT scan is unique, the calibration has to take into consideration the polychromatic x-ray spectrum and detector energy dependency of the scanner. Most common approach is to identify the fitting parameters k_1 and k_2 from equation (2.20) through analysis of several scans of known element composition materials in phantoms. Once the fitting parameters are identified, synthetic HU values for any human tissue with known properties can be estimated through equations (2.18) and (2.20). The synthetic values reflect the HU value one would get if such tissues where scanned with the calibrated scanner.

The tissue substitution calibration curve for protons follows the same procedure as the one discussed for x-rays. Proton relative stopping power with respect to water is characterised by the Bethe-Bloch formula and is depicted as,

$$\rho_s = \frac{\widehat{\rho_e}\left\{\log\left[\frac{2m_e c^2 \beta^2}{I_m(1-\beta^2)}\right] - \beta^2\right\}}{\left\{\log\left[\frac{2m_e c^2 \beta^2}{I_w(1-\beta^2)}\right] - \beta^2\right\}} = K\widehat{\rho_e} \tag{2.22}$$

Where, I_m is the mean ionisation energy of the medium or CT voxel and I_w is the mean ionisation energy of water. For a mixture of atoms, Braggs additivity rule was utilised to identify I_m from the ionisation energy I_i of each element in the mixture similar to equations (2.9) and (2.10) [60]. Therefore, equation (2.22) indicates that the RSP of protons is linearly proportional with the relative electron density of the medium. The main error in the RSP calculation is the uncertainty in the ionisation potential of the voxel. However, studies indicated that the proportionality constant K is rather insensitive to the ionisation potential. Schneider reported a RSP change of less than 1.5% from a 10% variation of the ionisation potential [58]. Additionally, the fact that K is close to unity implies that the relative electron densities and relative proton stopping power track another closely.

To conclude, Stoichiometric calibration can be utilised to convert from HU to RSP generating a Hounsfield Unit Look Up Table (HULT). The calibration has to be performed on individual CT scanners, based on phantom measurements and tissue substitution values to identify both coefficients *σ* and *K*. Usually a bi-or tri-linear relationship is utilised for the conversion of HU to RSP dividing the spectrum into three sections. The first section represents lung data, the second section is a mixture lung, fat and organs and the last one for bone tissue. There are no definite HU values to separate these regions and the range of each one should be determined based on calibrated scans.

2.5 Intrafractional motion

Intrafractional motion refers to the internal motion of anatomical structures, including the tumour, organs and bone structures such as the ribs for cases of thorax tumours. This motion is primarily caused by the respiration cycle of the patient during irradiation. Understanding and quantifying intrafractional motion is crucial for evaluating its effects on treatment plan quality. The effects of intrafractional motion on pencil beam scanning treatment plans encompass several factors, including geometrical misses, proton range uncertainties due to organs and ribs moving in and out of the beam path and interplay effects.

Geometrical misses occur when the movement of the thoracic tumour causes deviations from the planned position within the treatment plan aperture. This unaccounted tumour motion leads to spatial misalignment and potential underdosage of the target volume. Therefore, it is essential to have a thorough understanding of the tumour motion, including both translational displacement and volumetric variation in order to accurately account for it in the treatment planning procedure.

In addition, the dynamic motion of organs such as the heart, diaphragm and ribs can cause fluctuations in the proton range. As these structures move in and out of the beam path during tumour irradiation, the overall stopping power of the beam deviates from the expected during treatment planning. Additionally, density alterations of lung tissue due to respiration along the beam path, could potentially impact the overall beam stopping power, introducing uncertainties in the delivered dose. Significant anatomical variation during irradiation can lead to an insufficient tumour coverage and overall plan degradation.

Furthermore, interplay effects arise from the relative motion between the tumour and the scanning proton beam and can cause deviations in the delivered dose distribution compared to the planned. The timing and position of the proton beam spots do not match the planned position due to tumour movement. This can lead to dose homogeneities and the creation of regions of over- and under-dosage within the target volume.

2.6 Water Equivalent Path Length

Employing the converted RSP values obtained from the calibrated CT scan, the determination of water equivalent path length (WEPL) for protons in tissue becomes possible. The WEPL represents the cumulative RSP values adjusted to estimate the depth of water that would produce an identical proton stopping power. To approximate WEPL using the transformed RSP-CT scan data, the following mathematical formula was utilised,

$$WEPL = \sum_i RSP_i x_{i,} \qquad (2.23)$$

where subscript i denotes the voxels along the path of the beam and x represents the chord distance in mm travelled by the beam through the voxel. The WEPL serves as a single parameter that characterises the stopping power of the proton beam within the patient from the CT images.

A significant clinical application of the WEPL is to identify robust angles that mitigate the effects of intrafractional motion on plan quality [61]. In proton therapy of lung cancer, treatment plans are generated based on a static representation of the patient and do not explicitly consider anatomical changes due to respiration. Therefore, by analysing variation in the WEPL between planned and evaluated CT scans, it is possible to quantify anatomical changes that occur along the beam path during irradiation. An increased WEPL along the proton path results in an undershooting of the Bragg peak, while a decreased WEPL leads to an overshooting. Both scenarios induce variations in the deposited dose distribution compared to the planned treatment, potentially resulting in underdosage of the target volume and/or overdosage of adjacent organs at risk. WEPL analysis is performed to identify optimal beam angles that experience minimal anatomical variations.

An additional clinical application of WEPL is to monitor and evaluate the impact of anatomical variations occurring during the course of the treatment, by comparing WEPL changes between the

planned and subsequent repeat CT scans [62]. Variations in tissue densities along the beam path of the proton beam, reflected in WEPL variations, can influence proton ranges and distribution of deposited dose similar to intrafractional effects. If significant alterations in WEPL are observed, the ability of the current treatment plan to deliver adequate tumour dose may be compromised and plan adaptations may be required. However, the use of WEPL as a tool to monitor interfractional anatomical variations for adaptive strategies is out of the scope of this study.

2.6.1 Angle Selection Algorithms

The advantages of employing intensity-modulated proton beam therapy (IMPT) for lung cancer treatment have been evident, as it can improve dose conformality and spare healthy tissue. However, uncertainties related to proton range and tumour motion pose greater challenges for IMPT compared to passive scattering proton therapy (PSPT) and intensity-modulated radiation therapy (IMRT). To address these uncertainties, several studies focused on identifying robust beam angle arrangements and robust plan optimisation.

Zhou et al reported on the number of publications regarding angle optimisation for particle therapy with comparison the number of particle therapy centres [63]. The figure indicates a positive relationship, emphasising the significant need for robust angle identification in this field, with the water equivalent path length (WEPL) method demonstrating great promise.
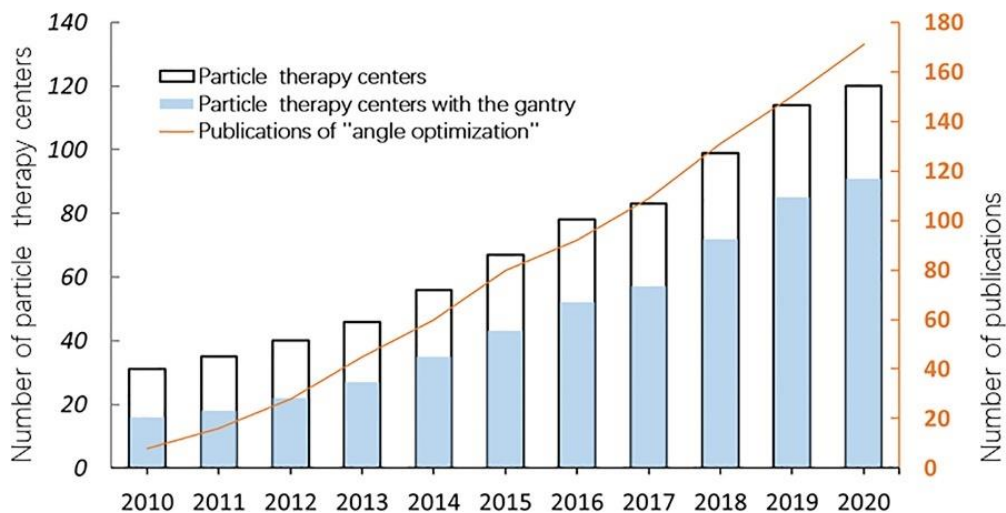

Figure 2.30: Number of particle therapy centres in operation and publications on "angle optimization" in the past 10 years (2010–2020) reported by Zhou et al [63].

2.6.2 Correlation of WEPL with Dose Degradation from Literature.

In 2014 Chang et a published the first, to the best knowledge of the authors, clinical implementation of IMPT for thoracic malignancies [64]. They explored various factors, including the potential use of WEPL to identify robust beam angles by estimating the average variation in WEPL (ΔWEPL) of the beam. However, their study did not report on the effect of incident beam geometry on target dose degradation and only investigated angle combinations with a couch angle of zero. Additionally, Magaz et al conducted a study that demonstrated a correlation between the average ΔWEPL and reduction in iCTV dose, assessed by evaluation the iCTV V95, percentage volume that accumulated 95% of prescribed dose, of nominal and evaluated plans [65]. Their study identified a strong correlation, with correlation coefficients reported within the range of 0.92 and 0.98, although it is important to note that they only considered three patients with right-sided lung tumours. Moreover, their use of the maximum intensity projection (MIP) CT scan as planning CT posed does not reflect clinical applications as discussed in section 2.4. Furthermore, the evaluation of WEPL was limited to the iso-centre plane, without consideration of the distal edge of the tumour.

More recent studies have evaluated the effect of ΔWEPL with dose degradation, utilising metrics such as D95 reduction of the iCTV. Zhou et al. demonstrated the effectiveness of WEPL in identifying robust angles for thoracic cancer cases, including lung, esophageal and pancreatic cancers [63]. Additionally, Yu et al also demonstrated a strong correlation between average ΔWEPL and D95 iCTV dose reduction in a dataset of 11 esophageal cancer patients [66]. Their study emphasized the patient-specific nature of WEPL curves. However, for the investigated beam geometries, all with a couch angle of 0, they found that posterior angles exhibited the lowest ΔWEPL and experienced the least dose degradation.

The utilisation of WEPL analysis for identifying robust treatment angles has been demonstrated in the literature, indicating a strong correlation between ΔWEPL and tumour dose degradation. However, to the best knowledge of the authors, currently no angle selection algorithm takes into consideration both tumour coverage and dose to organs at risk.

2.7 Treatment planning

2.7.1 Delineations

The first step of treatment planning is the delineation of the target volumes and organs at risk on the planning CT scan. The visible tumour delineated by an experienced oncologist is defined as the Gross Tumour Volume (GTV). Demonstrating the extend and size of the tumour, the GTV encompasses the primary tumour and other metastases that may occur. To account for subclinical microscopic malignant regions that are not visible in the GTV, an isotropic margin is imposed to generate the Clinical Target Volume (CTV). Internal Target Volume (ITV) is utilised to account for internal physiological movements, size, and shape variation of the tumour. ICRU report number 65,

recommend an additional margin to be imposed on the CTV to generate the ITV [67]. However, for lungs cancer patients, where a 4DCT scan is acquired, the iGTV and iCTV can be constructed by a geometric summation of all GTV and CTV from each phase of the breathing cycle. Patient set-up and motion uncertainties are accounted through an additional margin on the iCTV to generate the Planning Target Volume (PTV). Typical orans at risk delineated for LA-NSCLC cases are the lungs, heart, spinal cord, trachea, esophagus and brachial plexus.
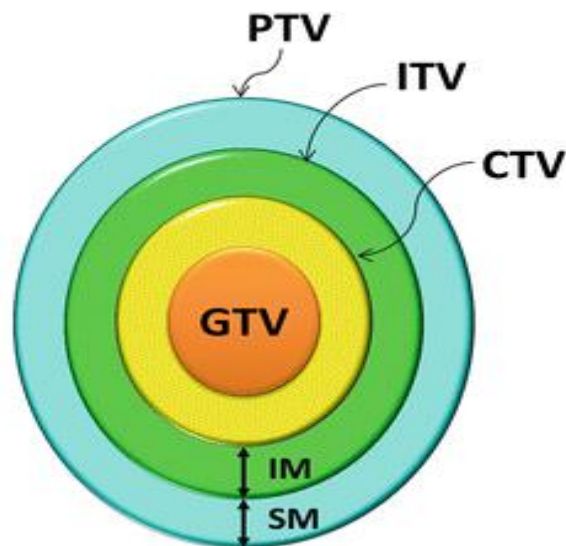
Figure 2.31: Schematic visualisation of the treatment planning volumes utilised in radiation therapy. [68]

2.7.2 Treatment setup

Following the delineation of all relevant volumes, the next step in treatment plan setup is to define the desired treatment qualities. These qualities encompass several essential factors, including the desired treatment volume, prescribed dose, number of treatment fractions, and dose normalisation. These variables depend on the type and location of tumour and whether the treatment purpose is palliative of curative and may vary from clinic to clinic based on the treatment protocols used. In addition, the treatment phase also involves configuring the number of beams and angles of the incident radiation. The angle selection procedure is done manually based on the experience of the treatment planner. By carefully choosing optimal beam angles, the treatment planner aims to optimise the effectiveness of beam delivery, while minimising impact to healthy tissue.

2.7.3 Plan optimisation

In radiation therapy, the treatment planning procedure is defined as inverse planning, where the desired treatment outcome is known, but the optimal approach to achieve it is determined mathematically through plan optimisation. For pencil beam scanning proton therapy, the optimisation procedure is twofold, encompassing the identification of spot positions and spot intensities. This is accomplished through the minimisation of a quadratic cost function portrayed as,

$$C = \sum_{i}^{N} I_i \, (D_i - D_i^P)^2$$

(2.24)

Where D_i represent the dose delivered to the ith voxel, D_i^P is the prescribed dose for the ith voxel, N the total number of voxels and I_i the importance factor associated with the voxel. Objective parameters set by the treatment planner affect the D_i^P and I_i variables to ensure desired dose to the target while imposing dose constrains on organs at risk and healthy tissue. Additionally, to ensure adequate tumour coverage, the iCTV and iGTV volumes are incorporated into the optimisation function. There volumes account for tumour motion and variation during beam irradiation, ensuring that an acceptable tumour coverage is achieved. During the optimisation procedure, the spot intensities are adjusted iteratively to minimise the cost function, by taking into consideration the plan objectives and associated weighting factors set by the treatment planner.

2.7.3 Robust Optimisation

To ensure an acceptable dose coverage of the CTV despite uncertainties in proton range, patient set errors, target, and organ motions, the PTV margin is employed in conventional radiotherapy. However, for IMPT where the position of the Bragg peak can shift individually, conventional margins may not be effective. As reported by Lomax, setup and range uncertainties for highly modulated IMPT and VMAT plans induce distortions in the dose distribution and even though conventional margins cope well with rigid dose shifts, more sophisticated tools are required for uncertainty management for these modalities [69,70].

In robust optimisation, the minmax optimisation algorithm is employed to incorporate systematic, random and intrafraction uncertainties. The objective of the robust optimisation procedure is to minimise the penalty associated with the worst-case scenario in each iteration, thereby identifying parameter values that exhibit robustness. The worst-case scenario describes the extreme value realisation of the uncertainty. Subsequently, treatment simulations are conducted for all considered scenarios, and the average robust objective score is computed, ensuring adequate tumour coverage and organs at risk sparing when subjected to perturbations.

In the context of proton therapy, uncertainties induced from the conversion of Hounsfield Units to mass density introduce errors in proton range, which must be addressed in the robust optimisation procedure. To account for range uncertainties, a scaling approach is employed where the mass density is modified in both positive and negative direction by a predetermined percentage. Furthermore, uncertainties arising from setup errors can be considered in all treatment fractions through directional uncertainty modelling. Additionally, if a 4D CT scan or a simulated organ motion dataset is available, intrafractional errors can be incorporated in the optimisation algorithm. To address these uncertainties, their extreme values are discretised and included as input scenarios to the minmax optimisation algorithm, which then aims to identify spot weights that exhibit the least sensitivity to these uncertainties, ensuring plan robustness.

In 3D robust optimisation, the optimisation procedure does not incorporate intrafractional uncertainties. It solely takes into account the planning CT scan and evaluates 7 patient shifts, including nominal plan position along with 3 density shifts. As a result, a total of 21 worst-case scenarios are generated, and the minmax optimisation identifies the robust objectives. In contrast, the 4D robust optimisation takes into consideration intrafractional uncertainties such as tumour and organ motion and tissue alterations along the beam path, by incorporating all breathing phases in the optimisation procedure. The 21 evaluated scenarios in the 3D robust optimisation are then extended to encompass the 10 phases of the 4D CT scan and the planning CT scan, resulting in a total of 231 scenarios being evaluated. The inclusion of all breathing phases in the 4D robust optimisation allows for a more detailed analysis of the potential errors, particularly in the case of IMPT for lung cancer. However, it should be noted that this increased level of analysis comes at the cost of significantly longer computation times due to the increased number of evaluated scenarios.

2.7.4 Dose Algorithms

In radiation therapy, the calculation of dose distribution can be achieved by utilising either a Monte Carlo simulation or a pencil beam algorithm. These methods aim to accurately describe how incident radiation traverses through tissue and how energy deposition occurs, including dose contribution of secondary electrons. Monte Carlo simulations provide a numerical approach that closely approximates the ground truth by tracking individual particles and their interactions. Although Monte Carlo simulations are computationally intensive and relatively slow, they are considered the most accurate method for dose calculation in radiotherapy.

On the other hand, pencil beam algorithms are kernel-based and offer quick computation times. They assume that the incident radiation beam can be represented as a combination of infinitely thin pencil beams. The dose distribution around the interaction point is described by a point-spread kernel, which contains information about the expected dose deposition from both primary and secondary radiations. These kernels are typically generated analytically, often based on results obtained from Monte Carlo simulations. The generated dose distribution utilising a pencil beam algorithm is identified through a preconvolution process, where the point spread kernel is multiplied with the

beam fluence to generate the pencil beam kernel. The preconvolution accounts for the dose distribution around the infinitely thin pencil beam.

Heterogeneities along the path of the radiation beam can significantly impact the scattered conditions, requiring adjustments in the kernels used in pencil beam algorithms. While pencil beam fluence can be corrected for forward scattered radiation by elongation of the kernel, it is unable to adequately account for lateral scatter. Consequently, when the radiation beam traverses from a higher to a lower density, the lateral transport will be underestimated and conversely overestimated from a lower density to a higher density.

Secondary electrons in lung tissue, have a significantly higher range and tend to deposit radiation at larger distances from the beam. Consequently, utilising a narrow beam geometry, a reduction in the dose is observed. However, due to the underestimation of lateral transport in lung tissue, pencil beam scanning algorithms fail to identify this phenomenon, resulting in an overestimation of the dose. These limitations in pencil beam algorithms can lead to inaccuracies in the dose distribution that significantly affect treatment plans in the thorax region. Due to the overestimation of the deposited dose in lungs, underdosage of lung tumours will not be identified by the pencil beam algorithm. Therefore, Monte Carlo simulations are the preferred dose calculation algorithm in situations involving complex tissue heterogeneities, to provide a more reliable and precise result.

3. Methodology

3.1 Patient Data

For this study, free breathing 4D CT scans of locally advanced non-small cell lung cancer patients, acquired from the open-source dataset of *Hugo et al* were considered [71]. Part of The Cancer Imaging Archive, the dataset consists of 4DCT and 4DCBCT scans of 20 patients for the purpose of image guided radiotherapy, but for this study only the 4D CT scans were considered. Images where acquired on a 16-slice helical CT scanner (Brilliance Big Bore, Philips Medical System) with an external respiratory corelation system (Real-time Position Management, Varian Medical Systems). Additionally, audio-visual biofeedback was utilised to minimise breathing irregularities as discussed in section 2.3. The raw data were sorted into 10 breathing phases with phase 0% corresponding to the end of inhalation. The reconstructed slice thickness was 3mm for all images, with the in-phase pixel spacing varying from patient to patient within the range of 0.98 to 1.17mm.

Delineation of all targets and organs at risk was performed by an experienced radiation oncologist. For all images the gross tumor volume was delineated, however, due to the large size of the dataset, organs at risked were contoured only on a subset of the images [72].
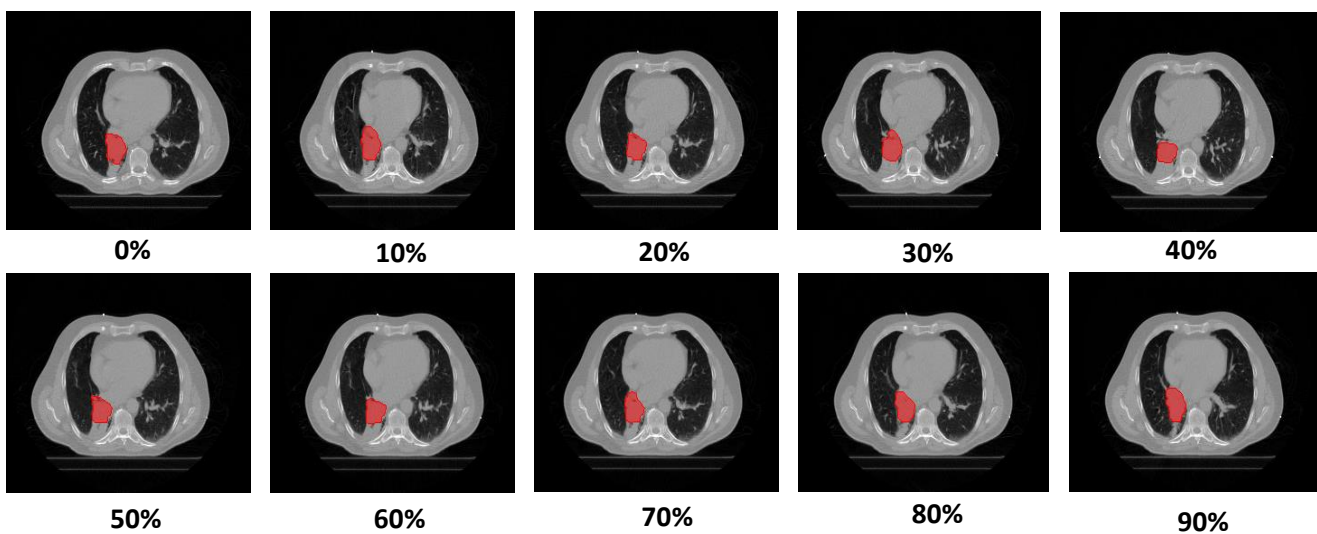
Figure 3.1: Visualisation of the 4D CT scan for patient 101. GTV is portrayed with red on all CT scans

For a patient to be considered in our study, delineations of the heart, both lungs and the spinal cord should be present in at least one phase of the CT scan. Other important organs at risk like the trachea and esophagus in the thorax region were not considered, due to lack of delineation in most of the images. Additionally, several anatomical and motion constraints where implemented. One patient was excluded from the study as no tumor motion was observed, while another patient with a more superficial tumor was excluded as a range shifter had to be used to acquire an acceptable treatment plan. *Figure 3.2* depicts the average CT scan of the latter patient where we can visualise how the iCTV

and iGTV volumes encompass the ribs of the patients. By including a range shifter to reduce the proton beams energy we introduce a great amount of secondary electrons that our following algorithms do not account for. These limitations were imposed to have consistency in our data and from the twenty patients of the dataset only eleven were utilised.
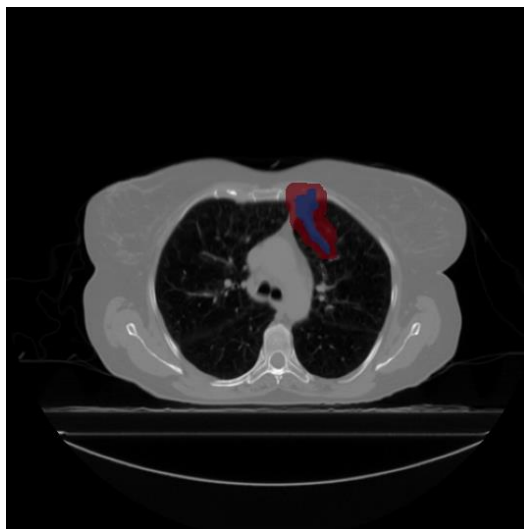
Figure 3.2: Average Intensity CT of patient 116. Portrayed in blue is the iGTV and in Red the iCTV.

Our sample size consists of patients with varying tumor location and overall cancer stage better representing clinical applications. Clinical information for each subject can be found in the accompanying paper of Huge et al and is portrayed in the *Table 3.1* with patient number kept identical to the referenced paper for continuity purposes [72].

Patient	Overall Stage	Location
100	IIIB	RUL
101	IIIB	RUL
102	IIIB	LUL
104	IIIB	LLL
105	IIIA	LLL
106	IIIA	Mediastinum
107	IIIA	LUL
108	IIIA	RUL
110	IIIB	RLL
111	IIIA	RLL
114	IIIA	RUL

Table 3.1: Overall cancer stage and location of the tumour for the patients utilised in this study. Tumour location is categorised in regions, Right Upper Lung (RUL), Left Upper Lung (LUL), Right Lower Lung (RLL), Left Lower Lung (LLL).

3.2 Pre-Processing Algorithm

A pre-processing algorithm was constructed to transform the images and contour structures in a more flexible format. Subsequently image and delineation transformations were performed.

3.2.1 DICOM to Array

Images were acquired in a standard Digital Image Communication in Medicine (DICOM) format with the contours in a DICOM-RT structure file type. Medical images can be manipulated by several libraries in python such as *pydicom* and *imageio*, however, for the RT structures the process is more complicated. Conventional libraries like the aforementioned do not directly extract the information from the RT structure, and the ones that do, have minimal versatility both on applicable actions and compatible libraries. Therefore, we decided to convert both the images and delineations in a 3D array format utilising an existing code from GitHub Depository designed by Kerem et al [73].

The algorithm converts both the image and structure files to arrays providing us with a higher flexibility to manipulate and extract information. The image is transformed to a 3D array where the voxel coordinates indicate the geometric location, and the voxel value is the HU. The delineations are portrayed in an identical size array as the image, with voxel value of 1 portraying the masked contour.

Within our dataset, there were several instances where the oncologist accidentally registered a single voxel as part of the delineation of the tumor or organ in a slice. The algorithm used however, could not handle contours with less than two points within a slice, resulting in an error with no information for that contour being extracted. An additional *if* statement was written that does not take into consideration all slices less than three contour points in accordance with the policy employed by RayStation as depicted in *Code 3.1*. The alter function of the GitHub algorithm is depicted here.

```python
1. def poly_to_mask(polygon, width, height):
2.     """Convert polygon to mask
3.     :param polygon: list of pairs of x, y coords [(x1, y1), (x2, y2), ...]
4.      in units of pixels
5.     :param width: scalar image width
6.     :param height: scalar image height
7.     :return: Boolean mask of shape (height, width)
8.     """
9.     # added if statement.
10.    if len(polygon) > 3:
11.        return np.zeros((height, width), dtype=bool)
12.
13.    img = Image.new(mode='L', size=(width, height), color=0)
14.    ImageDraw.Draw(img).polygon(xy=polygon, outline=0, fill=1, width=0)
15.    mask = np.array(img).astype(bool)
```

Code 3.1: Altered poly_to_mask python function from Kerem et al algorithm.

3.2.2 AIP, MIP and MinIP.

As discussed in section 2.4.2 several 3D scan representations of the 4D scan can be employed in radiation therapy. An algorithm was constructed to generate the AIP, MIP and MinIP CT scan of the patient from all the phases of the 4D scan. *Figure 3.3* illustrates the generated CT scans for patient 104 where the differences discussed in section 2.4.2 can be identified.

(a)   **(b)**   **(c)**
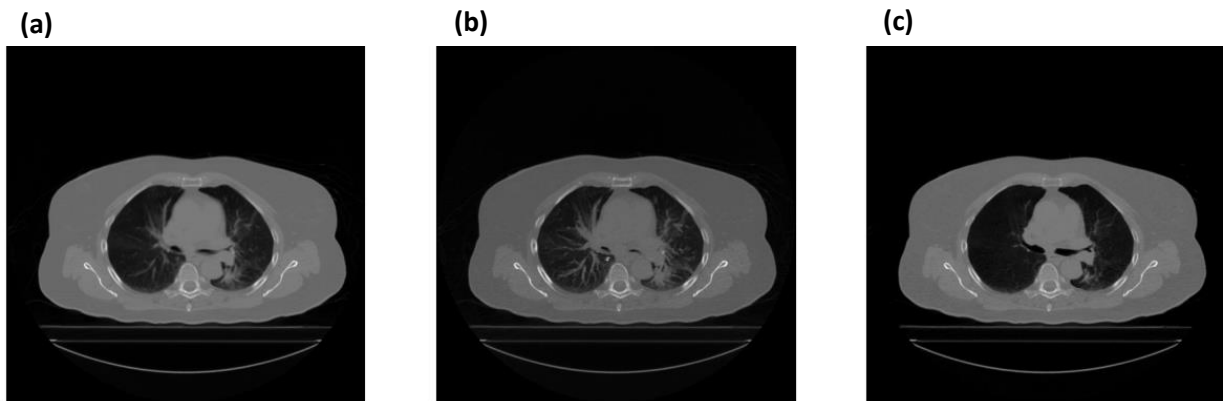
Figure 3.3: Generated AIP **(a)** , MIP (**b**) and MinIP **(c)** CT scans from patient's 104 4D CT scan.

3.2.2 Hounsfield units to Relative Stopping power.

In section 2.4.3 we discussed the physical relations between photon attenuation and proton relative stopping powers, and how one can employ stoichiometric calibration to generate a HULT. Even though we had no access to the CT scanner utilised for image acquisition of the open-source dataset, HU to relative electron density data have been presented [72]. Therefore, to convert the CT voxel values to proton relative stopping power the proportionality constant *K* from equation (2.22) had to be inferred. Since, physical measurements of relative stopping power (RSP) for calibration purposes could not be conducted, the K-factor was acquired from Schneider et al [58]. In the referenced paper chemical compositions of both phantom calibration equipment and biological tissues where acquired from ICRP 1989 and 1975 respectively. The relative electron density and proton stopping power was then reported for photon beam energy of 120kVp and proton beam energy of 219 MeV. The photon spectrum energy of the used CT scanner is identical with the one utilised for image acquisition of our dataset, while the proton beam energy is analogous to energies used clinically [74]. The conversion factor K was then identified for the corresponding relative electron density values of our dataset and the RSP was thus inferred.
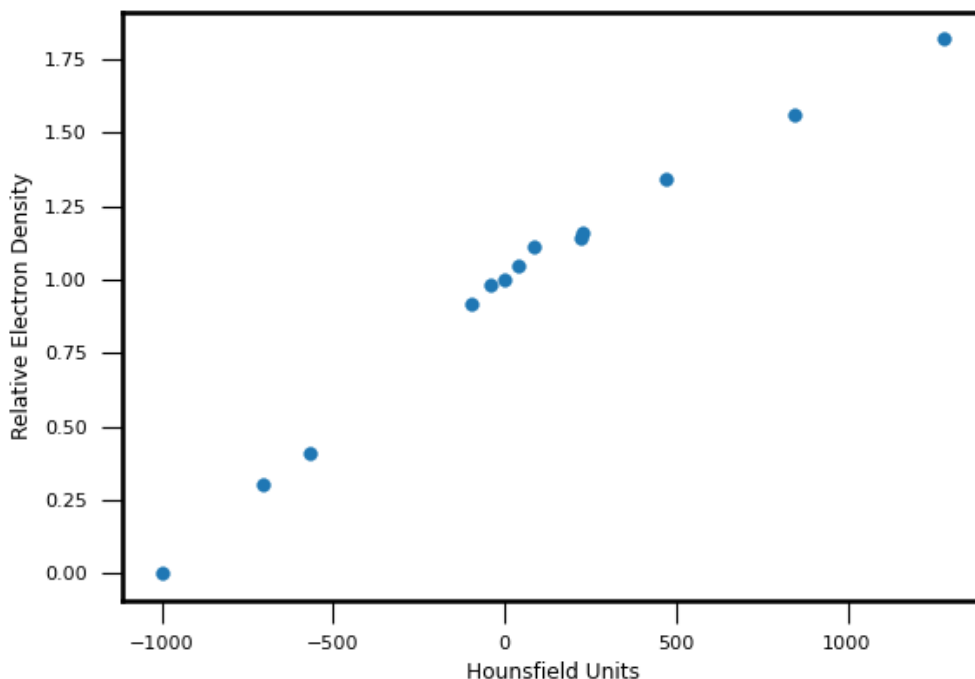
Figure 3.4: Relative Electron Density against HU of the imaging CT scan acquired from Huge et al [72].

Figure 3.4 depicts the provided Hounsfield Units to electron density values from Hugo et.al. Furthermore, the conversion factors K and corresponding estimated relative stopping power can be identified in Table 3.1. The HULT was thus constructed via a linear regression algorithm utilising 2 brake points and was utilised to convert CT voxel numbers to analogous proton relative stopping power.

HU	ED	RSP	K
-1000	0.00	0.00	0.000
-705	0.30	0.31	1.025
-569	0.41	0.42	1.025
-95	0.92	0.94	1.017
-42	0.98	0.99	1.013
0	1.00	1.00	1.000
20	1.03	1.03	1.004
40	1.05	1.05	1.005
86	1.11	1.13	1.02
225	1.14	1.15	1.019
227	1.16	1.18	1.019
473	1.34	1.33	0.998
845	1.56	1.52	0.975
1283	1.82	1.77	0.975

Table 3.2: Hounsfield Units and corresponding relative electron densities obtained from Hugo et al [72], with the linear coefficient K estimated from Schneider et al [58]. The relative proton stopping power was estimated utilising equation (2.22).

Conversion of all CT-voxels from HU to RSP was performed on all phases of the 4DCT, the AIP and the MIP. A visualisation of the converted CT scans for patient 104 is depicted in *Figure 3.5*.
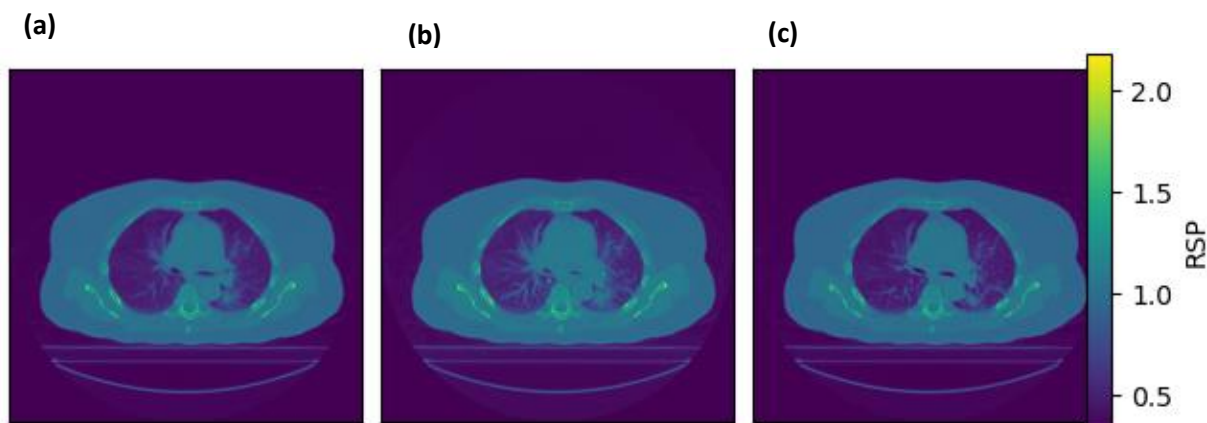
Figure 3.5: RSP converted **(a)** AIP, **(b)** MIP and **(c)** Phase 0% CT-Scans for patient 104.

3.2.3 Delineation Geometries.

Delineations of the tumor and organs at risk were extracted and converted into 3D arrays from DICOM RT structure. An algorithm was constructed to generate the delineated volumes used in radiation therapy as mentioned in *Section 2.7.1*. A 5mm isotropic margin on the GTV was utilised to convert to the CTV for all CT phases. Subsequently a geometric sum was performed both on the GTVs and CTVs to generate the iGTV and iCTV respectively, which takes into account the varying size and position of the tumor in each phase.

For the organs at risk, a similar geometric sum was performed to generate a single contour encompassing the voxels where the organ will be present during irradiation. If delineations were present on only a single phase, then only those volumes were taken into consideration. Additionally, as both lungs were delineated separately, a total lungs contour was generated and cropped around the CTV margin. All structure delineations are portrayed in *Figure 3.6* for patient 104.
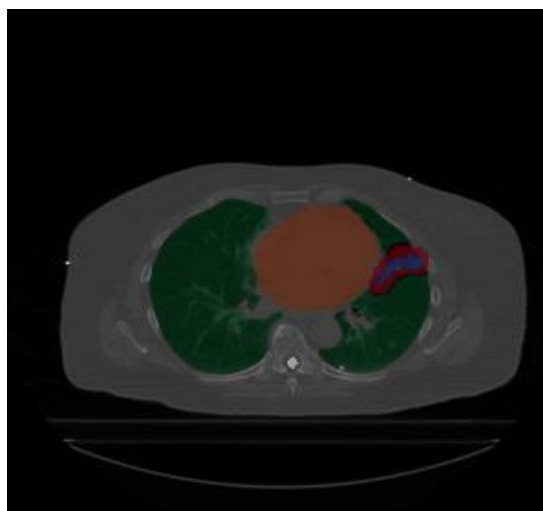
Figure 3.6: Visualisation of patient 104 delineations. Portrayed in blue is the iGTV, red the iCTV, green the lungs, orange the heart and white the spinal cord.

3.3 Tumor Motion

Intra-fractional tumor motion implicates alterations of the tumor location during irradiation of the patient. These changes encompass both movement and volumetric variation of the tumor within the breathing cycle. Utilising the delineation of the tumor from all phases we generated a code that extracts in-depth information on the tumor motion.

3.3.1 Volume Variation.

Volume tracking of the tumor is performed by inspecting the number of voxels within the delineations of the GTV and multiplying by the voxel volume of the image. All volumes are portrayed in cubic centimetres *cc*, as it is the standard clinical format. By evaluating the volume of the GTV in all phases of the breathing cycle, we can gain an understanding on the patient specific tumor variation. Tumor volume against phase is plotted as visualised in figure 3.5, where we can depict the volume bar graphs for patient 100 on the left and 104 on the right.
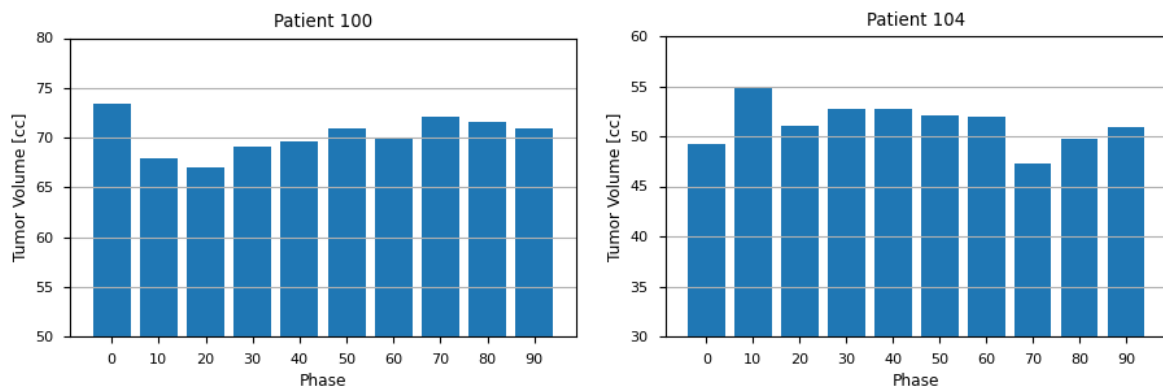
Figure 3.7: Tumor Volume in cc against Phase for patient 100 (left) and patient 104 (right)

To account for the varying tumor size of the patients within our dataset, the percentage volume variation metric was established. Percentage Volume Variation (PVV) enables us to compare volume variations of different patients and is defined as,

$$PVV = \frac{V_{max} - V_{min}}{V_{mean}} \times 100 \tag{3.1}$$

Where V_{max} and V_{min} are the maximum and minimum volumes of the tumor and V_{mean} the average volume from all ten phases. Utilising PVV we can compare the expansion and contraction of the tumor relative to the average volume, and thus, enable us to compare tumors of varying sizes.

3.3.2 Motion Amplitude.

Tumor motion amplitude describes the maximum movement of the tumor within the breathing cycle of the patient. To quantify this metric we constructed two algorithms, one utilising the tumour's centre of mass displacement and the other being an image deformation algorithm.

Centre of Mass.

The first method is based on tracking the position of the Centre of Mass (CoM) of the tumor from each phase and employing Euclidean geometry to identify the maximum displacement. The CoM of the GTV was measured for all phases, assuming a uniform tumor density, and was plotted in a 3D scatter plot to visualise tumor motion. Subsequently the displacement between tumor phases was calculated by scaling the Euclidean distance between the centre of mass coordinates with the voxel dimensions. Maximum motion amplitude was identified by identifying the maximum displacement between all phase combinations. In figure 3.6 we can visualise the centre of mass scatter plots for patient 100 (left) and 104(right). The axes are portrayed in voxel numbers in the directions Right-Left (RL), Anterior-Posterior (AP) and Superior-Inferior (SI).
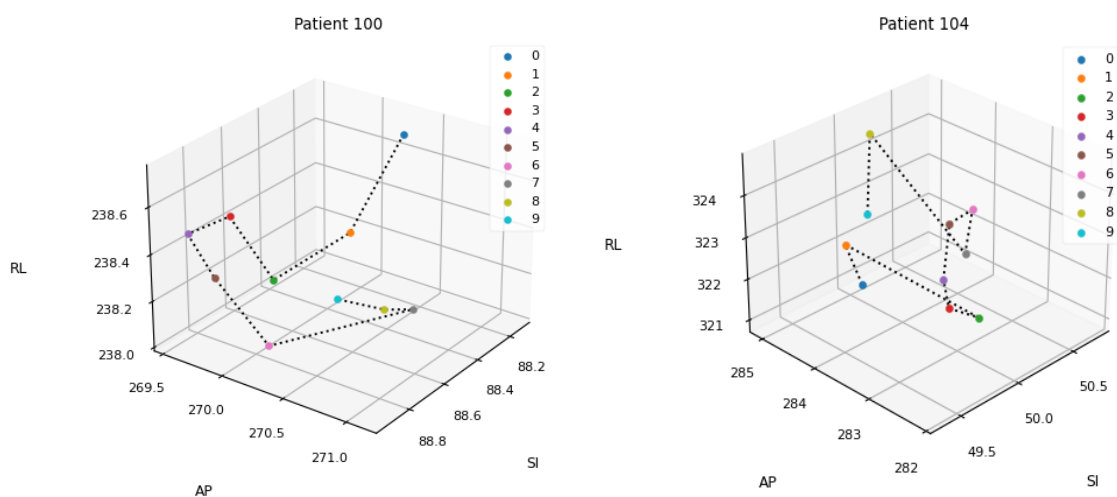
Figure3.8: Centre of Mass tracking plot for patient 100 (left) and 104 (right). Legend depicts the phase of the CoM point and axes are depicted in voxel number.

Image Deformation

The image deformation algorithm identifies the tumor motion amplitude through image registration, which involves aligning the tumor regions in different phases to quantify their motion. A deformation vector is then calculated enumerating the motion between two phases relative to an origin point. The reference point utilised for image registration is the centre of mass of the iCTV which corresponds to the iso-centre position of the treatment plan. Additionally, the image voxel dimensions are included so the calculated displacements were in mm. For this algorithm the multi-dimensional image analysis python library SimpleITK was utilised [75].

A registration framework is defined that aims to minimise the mean squares metric. This metric measures the dissimilarity between the reference tumor frame and the current tumor frame by averaging over the squared difference of corresponding pixels of the two frames. The optimisation

algorithm used is regular step gradient descent, which iteratively adjusts the parameters of a transformation model to minimise the metric. The aim is to find the optimal transformation that best aligns the tumor regions in the reference and current frames. To minimise computation times, a bounding box that encompasses the iGTV with a 5mm margin was constructed to act as the region of interest as depicted in *Code 2*. The computations were thus performed on this region and not the whole array of the tumors.

```
1.     # Generate a ROI as the itv bounding box (add some margins)
2.     itv_bb = itv.nonzero()
3.     z_min, z_max = np.min(itv_bb[0])+5, np.max(itv_bb[0])+5
4.     y_min, y_max = np.min(itv_bb[1])+5, np.max(itv_bb[1])+5
5.     x_min, x_max = np.min(itv_bb[2])+5, np.max(itv_bb[2])+5
```

Code 2: Generated Region of Interest (ROI) around the iGTV to minimise computational times.

The transformation model used in the code is a translation transform, which represents motion in terms of displacements along the RL, AP, and SI axes. The optimiser then adjusts the translation parameters during the optimization process to minimise the metric. During each iteration of the optimisation, the code computes the similarity between the reference and current frames based on the metric and updates the transformation parameters. The process continues until the optimisation converges to a desired similarity or reaches the maximum number of iterations which was set to 200.

Once the optimisation is completed, the final transform represents the deformation between the two tumor frames. The deformation vector is thus extracted from the final transform, which indicates the displacement of the tumor region between the two phases. Deformation vectors obtained for all frames combinations were accumulated and the maximum tumor motion amplitude displacement was thus inferred by interpolating the magnitude of the vectors. Additionally, directional tumor displacement can be extrapolated by determining the peak-to-peak difference of the deformation vectors along each of the three axes.

To conclude, the image deformation is achieved through the iterative optimisation of a transformation model to align tumor regions from different phases. Tumor displacement is thus quantified through deformation vectors where the motion amplitude and maximum directional displacement can be extrapolated.

3.3.4 Tumor Location Probability Map.

As tumor motion within the thorax involves both movements and volumetric variations, a metric that takes into consideration both processes had to be identified. The Tumor Location Probability (TLP) map was generated, where it represents the likelihood of finding the tumor at each voxel during the breathing cycle. Each voxel in the map corresponds to a specific location within the imaging volume, with the voxel values representing the probability of finding the tumor at that particular voxel during the entire breathing cycle.

To illustrate how the TLP map was generated, let us consider a more simplified two-dimensional example with only two tumor delineations. Each tumor delineation corresponds to the tumor

coordinates at various time points in the breathing cycle. First, a transformation of the input arrays was performed were tumor presence pixels were assigned a value of 1/N, where N is the number of phases. Tumor absence pixels were assigned a value of 0. Portrayed in *Figure 3.9* we can visualise the transformed tumor arrays for our 2D tumor examples. The red and yellow lines outline the tumor boundaries in the respective phase, with the tumor pixels being assigned a value of 0.1 for both, as the number of phases in the 4D CT were 10. As we can observe, the tumor in phase 2 exhibits a translation of one pixel towards the positive x-axis.
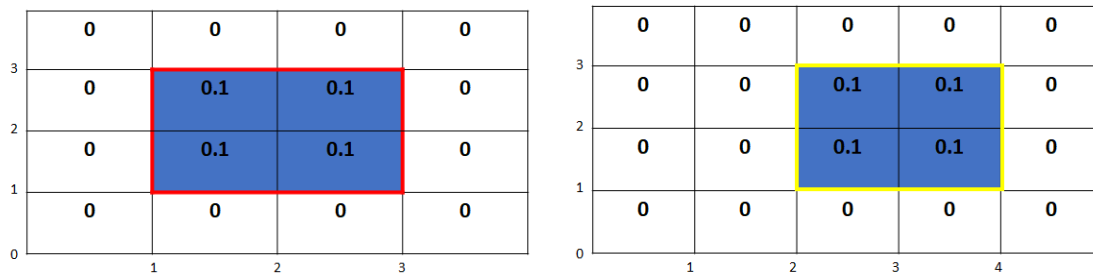
Figure 3.9: 2D representations of the tumor array with phase 1(left) and phase 2 (right). The red and yellow outlies depict tumor boundaries of the respective tumors.

Subsequently, a geometric sum of the two arrays was executed which results in the overlap voxels of the two tumor phases to be represented with a value of 0.2. By inspecting *Figure 3.10* we can visualise and identify the overlap area of the tumors and we can acquire information on the specific pixel probabilities.
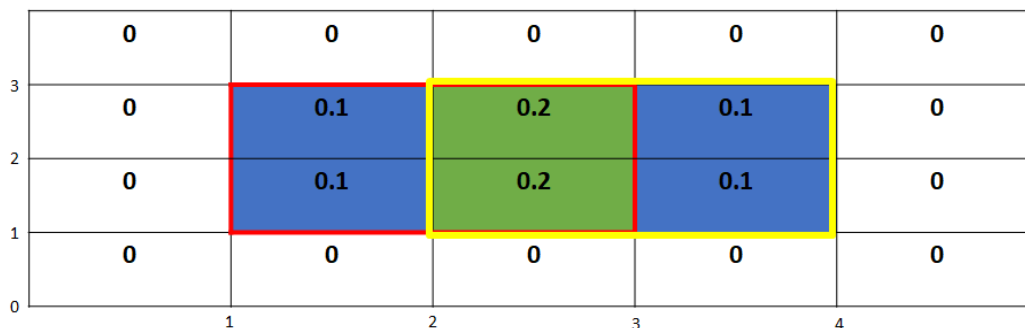
Figure 3.10: Illustrates the geometric summation of the 2D maps presented in Figure 3.9. The pixel values of 0.1 indicate the presence of the tumour exclusively in one map, whereas a value of 0.2 signifies the tumour's presence in that pixel across both phases.

By extrapolating this methodology in three-dimensions and geometrically summing over all 10 phase representations, the tumor location probability map is constructed. Geometrically, the TLP is identical with the ITV as it encompasses all the tumor voxels present from the ten GTVs. However, voxel values were transformed to tumor location probabilities and are within the range of 0.1 and 1, with 1 indicating that the tumor was always present in that voxel. Analysis of the TLP voxels enables us to comprehend in-depth the nature of tumor motion. Both volume variation and tumor movement metrics extract information based on the extreme measurements from corresponding phases. On the contrary, the TLP weights the motion equally in each phase incorporating both movement

mechanisms and provides information on the progression of the tumor motion in a single variable. Additionally, the TLP map enables us to compare and differentiate patients that exhibit similar extreme motion parameters.

Figure 3.8 depicts the three-dimensional plots of the of the TLP maps for patient 100 on the left and 104 on the right. The voxel probabilities are colour coded with the legend on the right with dark blue representing the probability value of 0.1 and light blue the value 1.0. Inspecting figure 3.8 we identify differences in the overall shape of the tumours ITV volume, but the nature of the 3D representation provides information only on the outer tumor cells. Therefore, it is useful to inspect cross-sections of the probability map. In figure 3.9 we visualise the three cross-sectional planes of the TLP maps at the iso-centre position, the location of the iGTV centre of mass. The top graphs are the axial, coronal and sagittal plane for patient 100 and the bottom graphs for patient 104. The iso-centre position is represented with the blue x in all images. The axes are portrayed in voxel numbers for all graphs, similar to *Figure 3.8.* In addition to cross-sections, we can extract a probability histogram to quantify the frequency of each probability value within the TLP map. We can visualise these histograms in figure 3.10 with the probability histogram of patient 100 on the left and 104 on the right.
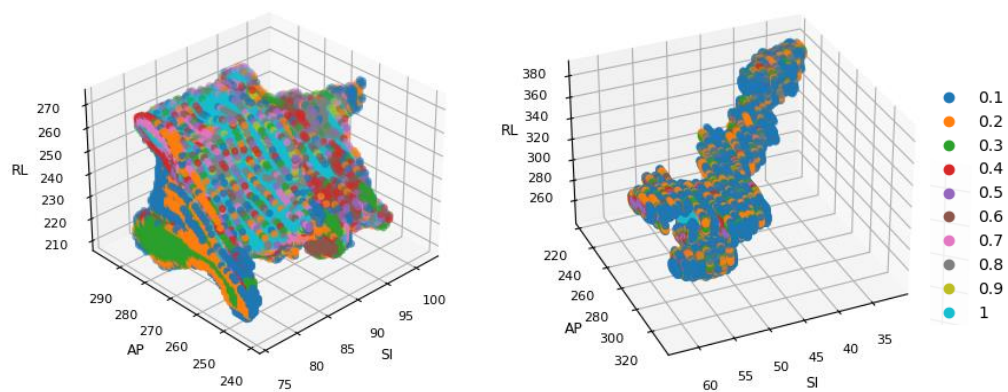
Figure 3.11: Visualisation of the TLP maps for patient 100(left) and 104(right)
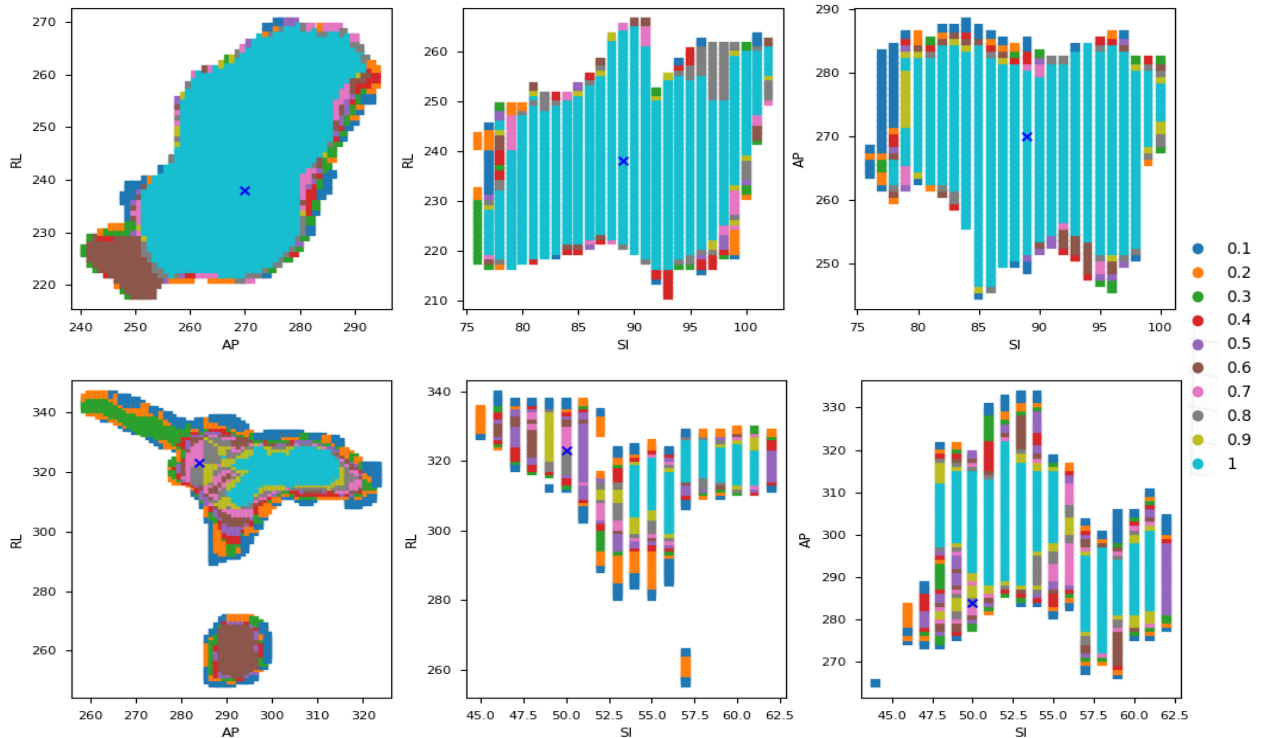
Figure 3.12: Cross section of the TLP maps for patient 100 (top) and 104 (bottom). Slices from left to right depict the axial, coronal and sagittal planes.
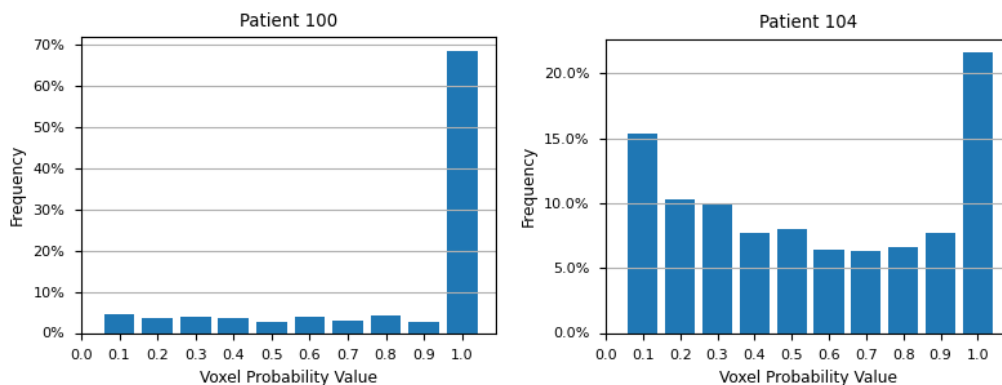
Figure 3.13: Probability histograms for patient 100 (left) and 104(right). The frequency of each voxel probability within the TLP map is portrayed.

3.4 4D Angle Selection.

In previous sections we discussed the proton transport sensitivities to tissue alterations. In proton therapy of lung cancer these variation along the beam path arise from respiration, resulting in alteration of lung tissue, movement of organs and thorax bone structures along the beam path. As mentioned before several studies utilised Water Equivalent Path Length (WEPL) analysis to minimise the effect of intra-fractional motion on deposited dose to the target region. To accomplish that, an optimal incident beam angle geometry was identified by minimising the tissue variations between planned and evaluated CT scans. A 4D semi-automatic angle selection algorithm was constructed that

takes to consideration both tumor coverage robustness as well as minimisation of dose to organs at risk. The tumor delineation employed for this algorithm was the iCTV to accurately simulate clinical proton treatment plans. Treatment plans for proton therapy of lung cancer are generated with treatment volume the CTV of the planned CT scan and evaluated on the CTVs of all evaluated phases. By incorporating the iCTV in our simulation we geometrically considered all CTV's. Additionally, the Average Intensity Projection CT scan was utilised as the planning CT, with all the breathing phases as the evaluated CT scans.

3.4.1 Distal Edge and Beam Simulation

To investigate the effects of incident beam geometry on plan quality, one should first identify the irradiated voxels of each spot for every arbitrary beam geometry. Therefore, the first step of our angle selection algorithm was to identify the tumour distal edge based on gantry and couch angle orientations and simulate the proton beam paths.

The relative beam direction is governed by the assigned couch and gantry angles which alter the patient orientation comparative to the beam. To simulate these orientation alterations, rotation transformation matrices where employed for the corresponding planes. Extracted from our Dicom_to_Array algorithm, the orientation of the output images was along the SI,AP,RL direction. Therefore, the transformation matrices utilised to represent the couch and angle rotations are,

$$Gantry\ Angle = \begin{pmatrix} 1 & 0 & 0 \\ 0 & \cos(GA) & \sin(GA) \\ 0 & -\sin(GA) & \cos(GA) \end{pmatrix}, Couch\ Angle = \begin{pmatrix} \cos(CA) & 0 & -\sin(CA) \\ 0 & 1 & 0 \\ \sin(CA) & 0 & \cos(AA) \end{pmatrix} (3.2)$$

Where *GA* an *CA* are the gantry and couch angles. Since applying these transformations on both the planned and evaluated CT scans would be very time consuming, considering that we want to iterate over several angle combinations, a more efficient approach was employed. Instead of transforming the scans directly, a method inspired by the random walk technique commonly utilised in Monte Carlo simulations was implemented. In this technique, the beam path was divided into discrete steps initiating from the distal edge point and simulated in a direction opposite the beam path. To determine the direction of each step, in terms of voxel traversal, the transformation matrices were applied on a directional vector of unity. The directional vector (0,-1,0) was utilised, such that for gantry and couch angles of 0 degrees, the beam will transverse normally towards the patient from the anterior direction. The origin point of the 3D image was set at the extreme anterior-right-inferior direction. Therefore, in conjunction with the fact that we inversely simulate the beam with starting point the tumor, we concluded to the aforementioned directional vector simulating the beam toward the anterior direction. For instance, when both gantry and couch angles were set to 0 degrees, the generated steps were (0,-1,0), while a gantry angle of 90 degrees yielded steps of (0,0,1). Employing this mathematical

formulation, the algorithm provided us with sufficient information to successfully identify the distal edge of the tumour and simulate the beam rays.

The identification of the tumour's distal edge for various angle combinations was accomplished using a binary search approach. The algorithm employed the estimated step distance, derived from the beam geometry, in conjunction with the tumour's spatial coordinates to conduct the search in the opposite direction of the step distance. Initiating the search from each voxel within the tumor, the algorithm evaluated the adjacent voxel along the beam path. This binary search process iterated until the algorithm encountered non-tumor tissue or surpassed a predetermined threshold upon reaching the tumor boundary. Successful execution of the binary search involved saving the coordinates of the last tumor voxel, resulting in the formation of an array exclusively comprising the distal edge of the tumor.

Subsequently, beam rays were simulated in an inverse manner, leveraging the estimated distal edge of the tumour in conjunction with the beam step distance. Employing a method that commenced from the identified distal edge points, the algorithm analytically generated lines representing beam trajectories by incrementing the coordinates towards the inverse beam direction. Instigating from the distal edge points, the algorithm generated the line by adding steps in the opposite direction of the beam ray. This iterative process was repeated until the proton ray reached the boundaries of the image, encompassing all distal edge points. To address steps with decimal places, only the coordinate corresponding to a unique voxel traversed by the beam was rounded up, while the rolling sum of coordinates retained decimal precision. The resulting output was a list of lists where each inner list consisted of the irradiated voxel along the proton rays path terminating at a distal edge point.

To conclude, the tumour distal edge and subsequent beam paths could be identified using the mentioned mathematical transformations, for all gantry-couch angle combinations. Depicted in figure 3.9, we can visualise two simulated proton beams for patient 100(left) and 104(right). For patient 100 the distal edge and proton rays were simulated for couch angle 0^0 and gantry angle 220^0, while for patient 104 the gantry angle was altered at 45^0. The calculated steps for the two patients were (0, 0.766, -0.642) and (0, -0.707, 0.707) respectively. The simulated rays are portrayed in blue with the iCTV and distal edge in red and yellow accordingly. For visualisation purposes, the distal edges depicted in figure 3.9 were expanded by 5mm.
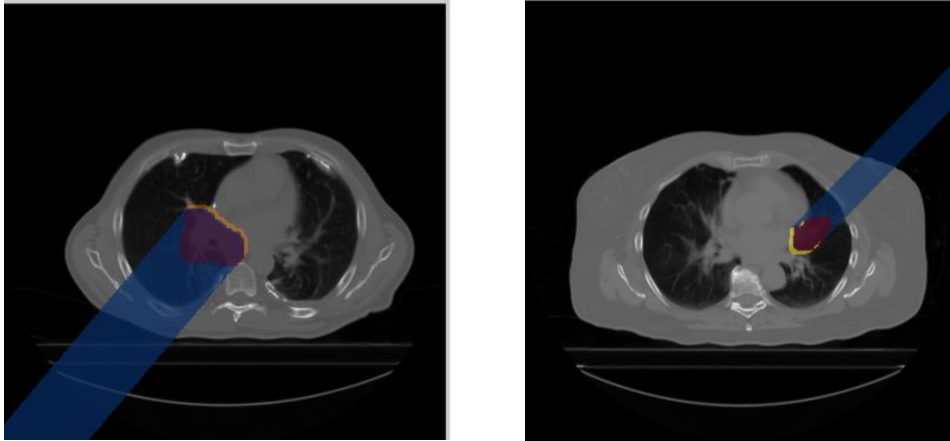
Figure 3.14: Visualisation of the distal edge and beam for couch angle 0 and gantry angles 220 for patient 100 (left) and 45 for patient 104(right). The iCTV is depicted in red, expanded distal edge in yellow and simulated proton rays in blue.

3.4.2 ΔWEPL and OAR irradiation maps

Optimal incident proton beam geometry should take into consideration both robustness of tumor coverage and minimisation of dose to organs at risk. Tumor coverage evaluation was performed through Water Equivalent Path Length analysis while for the organs at risk we evaluated the percentage of irradiated organ.

As previously mentioned, the Water Equivalent Path Length (WEPL) depicts the equivalent path traversed by a proton beam through water and is computed by summing the relative proton stopping power ratio, multiplied by the length of each step, cohort length. In the context of proton beam therapy for lung cancer, treatment planning is performed on a static representation of the target volume. A key objective is to minimise the variations in WEPL along the planned and evaluated beam paths, aiming to reduce uncertainties in proton range. In this study we refer to beam path initiated for a single distal edge point as a proton ray while all rays generated for a specific gantry-couch angle are defined as the proton beam.

In our study, we developed an algorithm to compute the variations in Water Equivalent Path Length (ΔWEPL) for a given couch-gantry angle combination. The reference WEPL was estimated by utilising the converted relative stopping power - average intensity projection (RSP-AIP) CT scan and performed a voxel-wise summation over the incident proton ray's path. The cohort length was determined by estimating the length of the proton beam path within each voxel. In simple cases like couch-gantry angles of 0-0, the cohort length is equal to the AP voxel dimensions, but this is not the case for more complex angle combinations. This process is repeated on the converted RSP - CT scans of all breathing cycle phases, and the evaluated WEPL for each proton ray was calculated. To quantify the difference in WEPL for each ray, we subtracted the absolute value of the reference WEPL from the evaluated one. Considering that positive and negative ΔWEPL correspond to overshoot and undershoot of the Bragg peak for a specific proton ray, the absolute value guaranteed that both instances were

accounted equally. Additionally, several instances could portray a positive ΔWEPL for some phase and an equally negative one for other. Consequently, the averaged ΔWEPL over the whole breathing cycle will be minimal if the absolute value is not considered and will not be representative of the observed variations. Ultimately, the ΔWEPL were averaged over all proton rays to identify a final value representative of the whole beam. The final ΔWEPL value was estimated and stored as a measure of the impact of the specific couch-gantry angle combination on the tumour coverage.

To assess the impact of incident beam geometry on accumulated dose for organs at risk, the percentage of irradiated organ volume was observed. The extend of overlap between the incident beam and organ was measured and normalised with respect to the total organ volume. Therefore, the percentage volume of the organ that was irradiated was estimated. In our study, we concentrated on three organs at risk, the heart, spinal cord, and lungs, as mentioned previously. Employing this approach, we stored the percentage irradiation of each organ as a measure of the effect of the specific couch-gantry angle combination.

Both ΔWEPL and OAR irradiation estimates were iterated for various couch-gantry angle combinations. Deliverable beam orientations are dependent both on the size and location of the tumour as well as physical constraints for each patient. A general template yielding 350 unique couch-gantry angle combinations was generated and utilised for all patients. Within our template, a 10° increment was employed for the gantry angle and a 15° for the couch angle. Values of the ΔWEPL and OAR irradiation were measured for all 350 combinations and are visualised in *Figure 3.15*. On the top the 2D maps for ΔWEPL and OAR irradiation, for patient 100 are portrayed and on the bottom for patient 104.
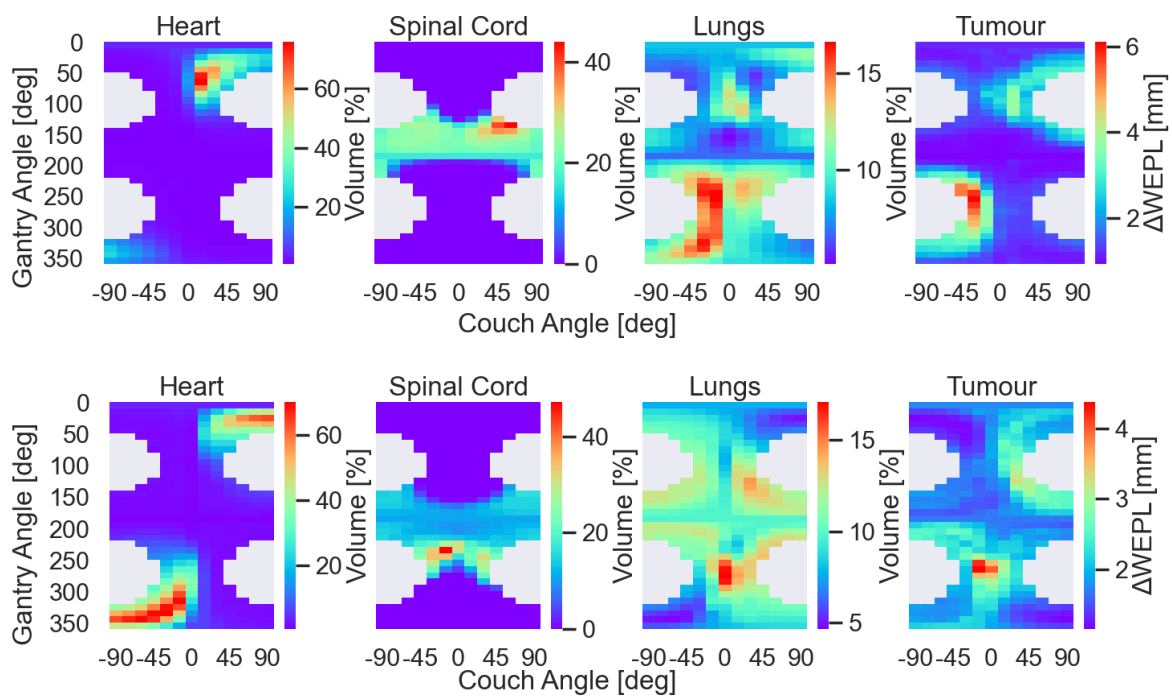
Figure 3.15: Organs at risk irradiation and tumor ΔWEPL maps for patient 100(top) and 104(bottom) are presented for the 350 unique beam geometries.

3.4.3 Z-Score Normalisation.

To integrate the information from the Water Equivalent Path Length difference (ΔWEPL) and Organ at Risk irradiation maps, we employed the Z-score statistic. This statistical method enabled us to standardise the values of each map such that their effectiveness could be combined in a single metric. The Z-score is mathematically defined as,

$$Z = \frac{x_i - \mu}{\sigma} \tag{3.3}$$

Where x_i is the ith pixel element of the map, μ is the mean and σ the standard deviation of the sample. The Z-score conversion was performed on each pixel of the maps depicted in *Figure 3.15*. Pixel values were thus transformed to a relative variable, representing the deviation from the population average in terms of standard deviation, as expressed by equation (3.3). Positive Z-scores indicated values above the mean, while negative Z-scores indicated values below the mean. The transformed Z-score maps for patient 100 (top) and 104 (bottom) are visualised in *Figure 3.16*. Comparison of Figures *3.15* and *3.16* illustrated that the 2D maps exhibited consistent behaviour, with only the pixel values varying. These maps provided a depiction of the relative impact of incident beam geometry on the corresponding target volume.
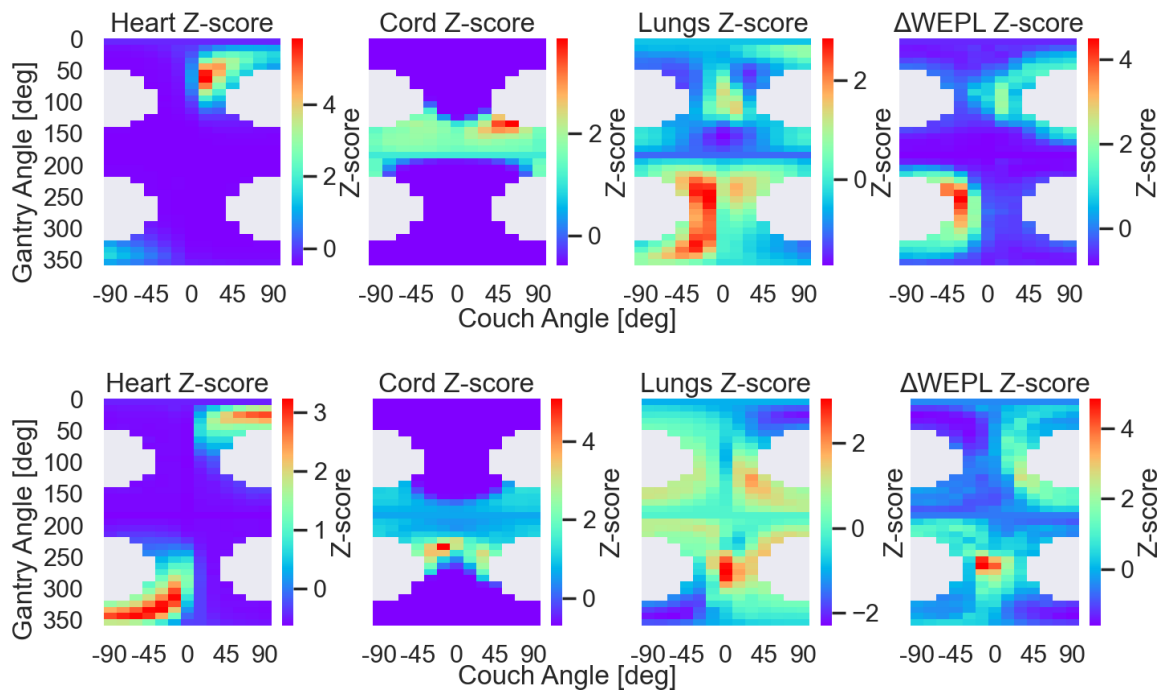
Figure 3.16: Transformed Z-Score maps for the organs at risk irradiation and tumor ΔWEPL analysis for patient 100(top) and 104(bottom).

To generate a comprehensive singular metric, all maps were multiplied with varying weighting factors and summed over to construct a Final Z-score map. This approach was inspired by the optimisation

process during treatment planning, where the significance of plan parameters can be altered utilising individual weighting factors. Patient-specific weighting factors for each map were determined based on observations of patient anatomy, such as the tumour's proximity to organs at risk, and analysis of the Z-score maps.

Weighting factors utilised for patient 100 were 2.0 for the tumor, 1.5 for the heart, 0.5 for the spinal cord and 1.0 for the lungs. A factor of two was assigned to the ΔWEPL map to ensure an adequate tumor coverage, while a compromise to the dose delivered on the spinal cord was performed to provide the flexibility for accumulated heart dose minimisation. As the tumour was located adjacent to the heart for patient 100, we decided to minimise dose to the heart from direct irradiation to account for the accumulated dose through scattered radiation. Additionally, as the spinal cord is further away from the irradiated target (Bragg peak of the proton ray) and is considered a serial organ, a more direct irradiation could be performed while maintaining the accumulated dose within the accepted margins. Subsequently, the weighting factors utilised for patient 104 were 2.0 for the tumor, 1.0 for the heart, 0.5 for the spinal cord and 1.5 for the lungs. Inspection of the Z-score maps for this patient depicted a contradiction between optimal geometries for the tumor and the lungs. A higher lung weighting factor was thus imposed on the final Z-score to identify optimal incident angles that maintain sufficient tumor coverage while minimising lung irradiation. The same methodology was imposed for the spinal cord, providing the flexibility for more direct irradiation to achieve the desired outcome if necessary. Visualised in *Figure 3.17* are the final z-score maps for patient 100 (left) and 104 (right).
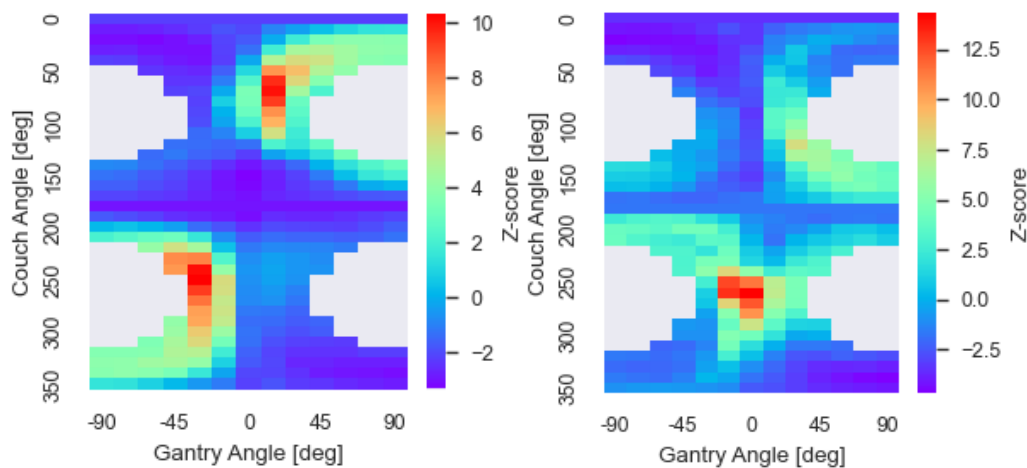
Figure 3.17: Final Z-Score maps for patient 100(left) and 104(right) utilising patient specific weighting factors for each map.

Final Z-Score map served as a unified representation of the combined information from the individual maps, enabling the identification of the optimal beam angles that minimised the effect to critical structures while maximizing the desired therapeutic outcome. Additionally, with our methodology, the treatment planner maintains the ability to adjust and compromise between plan objectives based on patient specific generated data and patient anatomy during the angle selection procedure.

3.5 Proton Therapy Treatment Planning

Proton therapy treatment plans conducted for this study were executed through RayStation 12A treatment planning software (RaySearch, Stockholm). In all generated treatment plans, a prescribed median CTV dose of 66Gy was administered over 33 equally weighted fractions of 2Gy. The average intensity projection CT scan was employed as the planning CT for all treatment plans. Deformable registration of all breathing phases on the AIP planning CT scan was performed. Depicted in Figure 3.18 is the deformable registration map of the AIP CT scan with phase 0% CT scan for patient 114. Employing the deformable registration all structure delineations were transferred onto the AIP scan. Patients with delineation of organs at risk only on a single phase, where firstly deformably transferred on the AIP and then transferred on all other phases for evaluation purposes.

Figure 3.18: Deformable registration map of Phase 0% CT scan on the AIP CT scan of patient 114.

Dose calculations were performed using the build-in Monte Carlo algorithm of RayStation with a predetermined set uncertainty of 1% for all treatment plans. The accumulated dose received by organs at risk was constrained within the dose tolerance limits of each organ outlined in the Oslo University Hospital guidelines. Once the composed treatment plan satisfied the predetermined criteria both for tumor coverage and dose constraints for organs at risk, the 4D evaluated dose was computed. The nominal planned dose was evaluated across all breathing phases and the deformed dose was then estimated for all CT scans by implementing the deformation map on the dose distribution of each breathing phase. Finally, the 4D evaluated dose was calculated by averaging over

all ten deformed doses and visualised on the AIP CT scan. Thus, the evaluated dose represented the cumulative dose distribution when intrafractional motion is taken into consideration.

3.5.1 Angle-Selection Validation Plans

Single field non robustly optimised treatment plans were developed and evaluated over the entire breathing cycle utilising the scripting capabilities within RayStation, in accordance with the aforementioned plan characteristics. Purposed to validate our angle selection algorithm results, dose information was extracted from the evaluated 4D dose distribution (4DD). The assessment of tumor coverage was performed by evaluating the D95 and D98 doses for the internal clinical target volume (iCTV). For the heart and spinal cord, the evaluated average dose and D05 were utilised, while for the lungs, the mean dose and V20 were employed. A script was created to generate treatment plans using a universal plan parameter template. The subsequent plan was scored across all breathing phases, and the relevant dose characteristics were extracted. The initial couch and gantry angles were set at 0° for both, with the procedure iterated with 10º gantry angle interval in accordance with our angle selection algorithm. Consequently, a total of 36 plans were acquired for each patient.

3.5.2 Robust Optimisation Strategies

In previous sections we examined the various optimisation strategies employed in active scanning proton therapy, to address set up, proton range and organ motion uncertainties. The efficacy of both 3D and 4D robust optimisation strategies in managing intrafractional motion effects was evaluated. For each patient, a 3D and 4D robustly optimised treatment plan was constructed and assessed. Robustness criteria applied included a 5mm isotropic expansion of the CTV and a 3.5% range uncertainty, which were only imposed on the target dose plan parameters.

Utilising the final Z-score map of each patient, the three optimal treatment angles were extracted and employed for treatment planning. The optimal treatment angles were determined by identifying the three-angle combination with the lowest Z-score, while imposing a minimum 20º angle separation between them. Beam separation was evaluated through the Central Angle theorem that describes the angular separation of two point located on the surface of a sphere. The two points in our case were the incident beams initiating points described by the couch and gantry angle combination. The central angle is mathematically described as,

$$CA = \arccos\left(\sin(GA_1)\sin(GA_2) + \cos(GA_1)\cos(GA_2)\cos(|CA_1 - CA_2|)\right) \qquad (3.4)$$

where subscripts 1 and 2 depict the gantry and couch angle of the two assessed points. A 90-degree gantry angle transformation was imposed when implementing the central angle calculation to transform the reference frame in accordance with the planning reference frame along the AP plane.

Plan parameter optimisation was performed for each patient during the 3D robust optimisation, and the same parameters were maintained for the 4D robust optimisation plan, provided that the nominal plan was within the acceptable criteria. Subsequently, the 4D deformed dose distribution was constructed and the evaluated dose characteristics were accumulated through a secondary RayStation script.

Robustness towards respiratory motion uncertainties was evaluated from the dose distribution of the evaluated deformed dose. Both optimisation strategies were analysed and compared on their ability to maintain sufficient tumor coverage through the criteria depicted on table. Criteria 1 depict the preferred dose distribution characteristics of the plan, with criteria 2 indicating acceptable levels.

	Criteria 1	Criteria 2
CTV – V95	>99%	>98%
iCTV – V95	>98%	>97%
iCTV – D95	>98% [6448cGY]	>97% [6402cGY]
iCTV – D98	>97% [6402cGY]	>96% [6336cGY]
iCTV Homogeneity index (HI)	<6%	<7%
iCTV DVH Bandwidth Low Dose	>100cGY	>150cGY
iCTV DVH Bandwidth High Dose	>100cGY	>150cGY

Table 3.3: Preferred and acceptable tumour coverage dose criteria utilised in evaluation of 3D and 4D robust optimisation treatment plans.

The following robustness evaluation criteria were derived from the HERAN 2 (Heterogeneously Hypo fractionated Radiotherapy of Locally Advanced NSCLC) clinical study conducted by Aarhus University Hospital and several other proton therapy plan robust optimisation studies [5,6,7]. Homogeneity index (HI) is an objective measurement to analyse the uniformity of dose distribution in the target volume and is defined as,

$$HI = \frac{D_{98} - D_2}{PD} \times 100$$

(3.5)

where PD is the plan prescribed dose of 66Gy in our study. The HI was calculated from the deformed dose of all breathing phases with the worst-case scenario being representative of the plan. Further analysis of the dose volume histogram (DVH) bandwidth of the CTV for low and high doses provides additional information on dose distribution in each breathing phase. Bandwidth is extracted from all ten scenarios of the DVHs at dose X% by identifying the maximum dose variation. The low and high bandwidth represent the variation of the DVHs at doses lower and higher than the prescribed dose and are defined as,

$$BW_{Low} = \frac{BW \ at \ D_{98} + BW \ at \ D_{95}}{2} \ , BW_{High} = \frac{BW \ at \ D_5 + BW \ at \ D_2}{2}$$

(3.6)

In conjunction with plan robustness, subsequent dose to organs at risk was measured and compared. Investigated organs at risk were again the heart, lungs and spinal cord with the mean dose being estimated for all, in addition to heart D5, spinal cord D2 and lungs V20.

4. Results

4.1 Hounsfield Units Look-Up Table.

Utilising the HU to relative electron density data provided by Huge et.al for our dataset, the corresponding relative proton stopping powers values have been estimated [72]. Employing the RSP values portrayed in *Table 3.2* as a calibration dataset, a piecewise linear HULT was then estimated utilising a linear regression algorithm with three linear regions. The two utilised brake points where at HU = 20 and HU = 80 and the following equations describing the HULT were derived,

$$RSP = \begin{cases} HU \times 0.001014 + 1.01373, & HU \leq 20 \\ HU \times 0.001488 + 1.00042, & 20 < HU \leq 80 \\ HU \times 0.00054 + 1.08604, & HU \geq 80 \end{cases} \qquad (4.1)$$

Portrayed in figure 4.1 is the derived HULT linear regression model utilised for the conversion of all CT scan employed in the WEPL analysis.
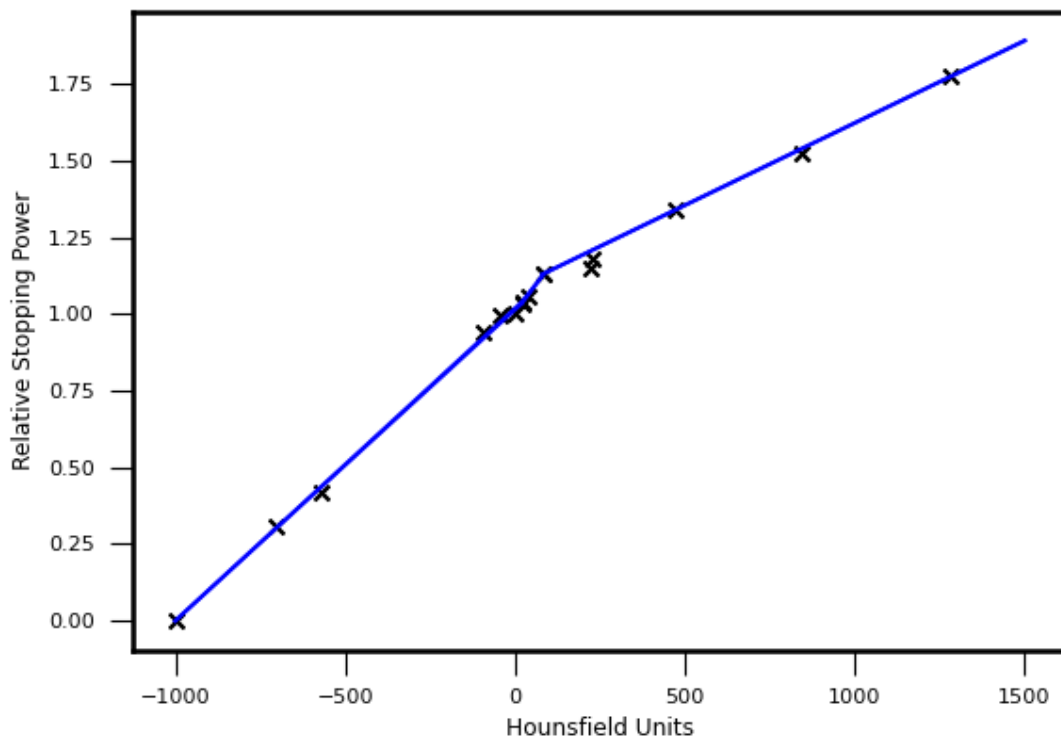

Figure 4.1 : HULT utilised for the conversion of HU to RSP in this study. The two break points utilised where at HU = 20 and HU = 80.

4.2 Tumor Motion

The following section presents the results obtained from the application of the tumor motion algorithm on our dataset of 11 patients. The algorithm employed two distinct approaches for analysing tumor translational displacement: the centre of mass (CoM) displacement method and the maximum displacement based on vector deformation method. Additionally, volume tracking was implemented with the average tumor volume and percentage volume variation presented. Finally, the average voxel probability and standard deviation extracted from the tumor location probability maps are presented. Tumor motion information extracted for all patients are reported in *Table 4.1.*

Patient	CoM [mm]	Def [mm]	RL [mm]	AP [mm]	SI [mm]	Volume [cc]	*PVV [%]*	Prob.	St.Dev.
100	2.4	2.3	0.43	1.74	1.93	70.2	9.1	0.8356	0.2837
101	7.5	10.9	2.15	2.95	9.04	27.7	16.16	0.6613	0.3348
102	2.4	9.9	0.57	1.82	9.81	182.9	5.83	0.8818	0.2576
104	5.3	4.0	1.96	3.55	2.13	51.25	14.7	0.5576	0.3327
105	7.9	5.6	5.35	2.95	4.41	36.9	13.46	0.5864	0.3393
106	5.8	13.3	3.66	8.75	13.19	150.4	4.2	0.7934	0.3239
107	2.5	3.3	1.70	2.84	1.26	19.07	12.46	0.8541	0.2897
108	2.9	11.1	1.53	1.59	10.98	11.35	39.71	0.6211	0.3552
110	7.0	10.4	5.05	8.47	4.10	57.27	23.85	0.6826	0.3249
111	5.8	9.4	5.55	6.69	5.88	78.89	14.2	0.7414	0.3229
114	11.4	5.1	5.06	2.22	1.90	186.86	13.61	0.7722	0.3094

Table 4.3: Results obtained from the tumor motion algorithm are presented for all patients of our dataset. CoM indicated the motion amplitude acquired with the centre of mass algorithm while Def the motion amplitude from the image deformation algorithm.

4.2.1 Motion Amplitude

By inspection of table 4.1 we identify significant variation in the tumor translation displacement from the two approaches utilised in this study. Even though both the centre of mass and vector deformation are mathematically valid approaches in identifying maximum tumor displacement, they exhibit different aspects of the tumor motion due to their underlying assumptions.

The centre of mass method estimated tumor displacement by considering the average position of tumor voxels. The provided estimate is based on the distribution of the tumor voxel and assumes that the tumor moves as a rigid body. On the other hand, maximum displacement calculated with the vector deformation takes into consideration local deformations of individual voxels. By observing each voxel individually, it assumes that the tumor can deform and change shape between breathing phases. This voxel-level analysis obtained from the image deformation method, depicts a more

comprehensive and representative evaluation of the tumour motion during the breathing phase. The rigid body motion assumption employed by the centre of mass approach, may not adequately identifying   intricate variations on tumor geometry during respiration. Therefore, through consideration of displacements at the level of individual voxels, the image deformation approach provides a more accurate assessment of the tumor spatial dynamics.

Comparative tumor motion analysis of patients 107 and 108 is of particular interest due to their similar tumour size and location. By inspection of *Tables 4.1* and *3.1* we identify that both tumors are located on the upper lungs' region, with the tumor for patient 107 on the LUL and 108 on the RUL. Additionally, tumour average volume was reported at 19cc and 11cc respectively. In accordance with the CoM method, the maximum tumor displacement of the two patients was reported at 2.5mm and 2.9mm respectively. In contrast, the image deformation approach yielded a 3.3mm and 11.1mm motion amplitude for respective tumours. The CoM reported motions suggested that the two tumours exhibit similar motion amplitudes, while the deformation vector distinguishes between them, indicating a significantly higher motion for patient 108. The latter observation is supported by the probability maps depicted in Figure 4.2, where patient 108 demonstrates a more pronounced motion. Additionally, the average voxel probability for both tumours further corroborated this finding, with reported values of 0.85 and 0.62 for patient 107 and 108 respectively. It is evident that tumor motion for patient 108 exhibited substantial geometrical variations during respiration, resulting in an underestimation of the motion by the CoM method, which inaccurately reports identical motion for both patients. Conversely, by utilising vector deformation, we were able to recognise and differentiate the motion levels between the two patients more accurately.
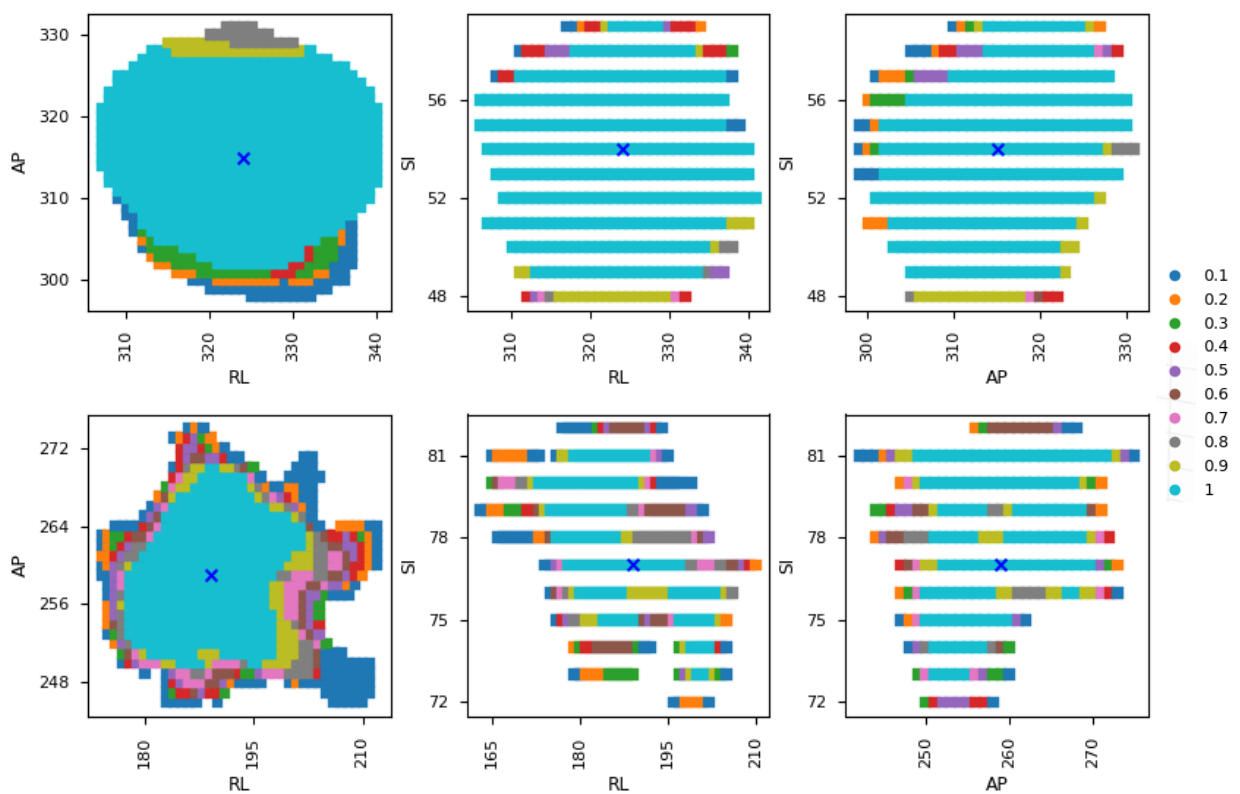

Figure 4.2 Probability map cross sections at the iCTV centre of mass for patient 107(top) and 108(bottom).

4.2.2 Volumetric Variation.

In addition to the translational displacement approaches, it is important to consider volumetric variations experiences by the tumour during respiration. This aspect of tumour motion is not accounted for by either the centre of mass or image deformation approaches. Inspection of *Table 4.1* and *Figure 4.3* provides insights into this aspect, depicting that patient 108 exhibits a significantly higher percentage volumetric variation of 40% compared to 12% for patient 107. While the deformation vector approach allowed for the consideration of alterations in tumour geometry, it does not take into account variations in tumour volume. Therefore, to obtain a comprehensive understanding of the tumour motion, it is crucial to evaluate both the motion amplitude and volumetric variation variables.
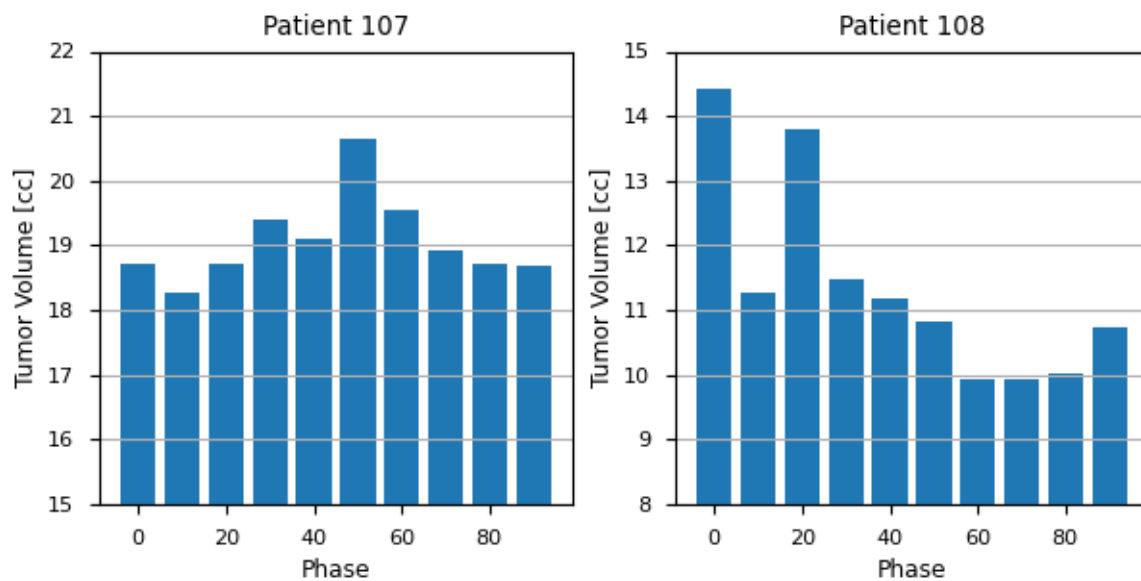

Figure 4.3: Volume in cc against phase for patient 107 (left) and 108(right).

4.2.3 Tumor Location Probability map.

Tumor Location Probability (TLP) map portrays a comprehensive representation of tumour motion, by considering both tumour displacement and volume variations during respiration. The TLP map provides valuable information through average and standard deviation values, which reflect the impact of motion on voxel probabilities, as well as through visual inspection. Additionally, unlike motion amplitude and percentage volume variation, which are extreme variables acquired from a two-phase comparison, the TLP map describes tumour motion by weighting each breathing phase equally. Moreover, this method takes into account the initial size of the tumour when assessing motion variables. A comparison of patients 105 and 114 demonstrates the influence of tumour motion relative to average tumour volume. Despite similar motion amplitudes of 5.63mm and 5.11mm, and comparable percentage volume variations of 13.46% and 13.61%, patient 114 exhibits a significantly

larger average tumour volume of 186.86cc compared to the 36.90cc of patient 105. *Figure 4.4* depicts the probability maps at the iCTV centre of mass for patient 105(top) and 114(bottom). While both patients exhibit similar motion characteristics, the larger volume of patient 114 results in seemingly less pronounced motion.

The visual observations are in accordance with the findings extracted from the probability map, which is reflected with the average voxel probability of 0.59 for patient 105 and 0.77 for patient 114. The TLP histograms portrayed in *Figure 4.5* further support these findings indicating that patient 114 has nearly double the number of voxels with probability value of 1 within the ITV when compared with patient 105. The distribution of other probability values is similar for both patients , with frequency values below 10%, except for slightly higher occurrence of 0.1 and 0.2 probabilities for patient 105.

In conclusion, the tumour location probability map serves as a comprehensive metric that incorporates both tumour displacement and volumetric variations. Furthermore, the extend of tumour motion is normalised based on the average tumour size, resulting in more pronounced motion for smaller tumours with similar motion parameters. The voxel-wise analysis provided by the probability map enables the accurate characterisation of tumour motion during respiration.
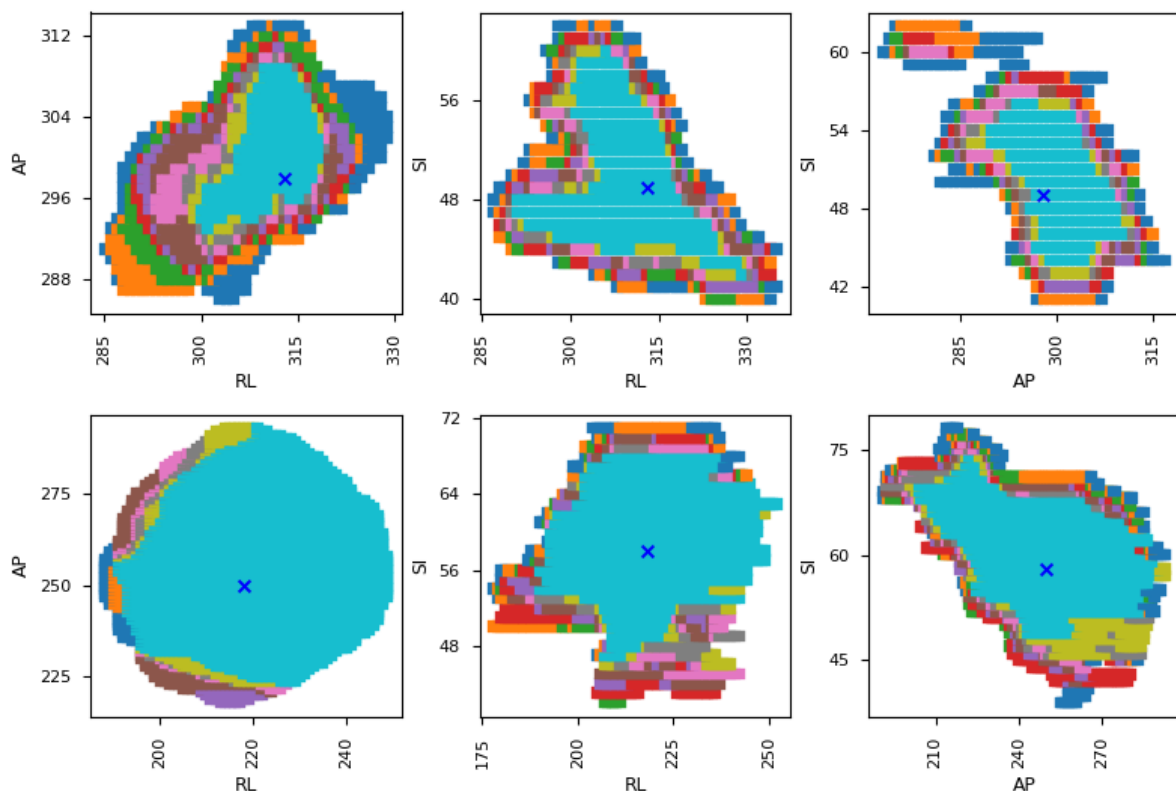

Figure 4.4: Probability map cross sections at the iCTV centre of mass for patient 107(top) and 108(bottom).
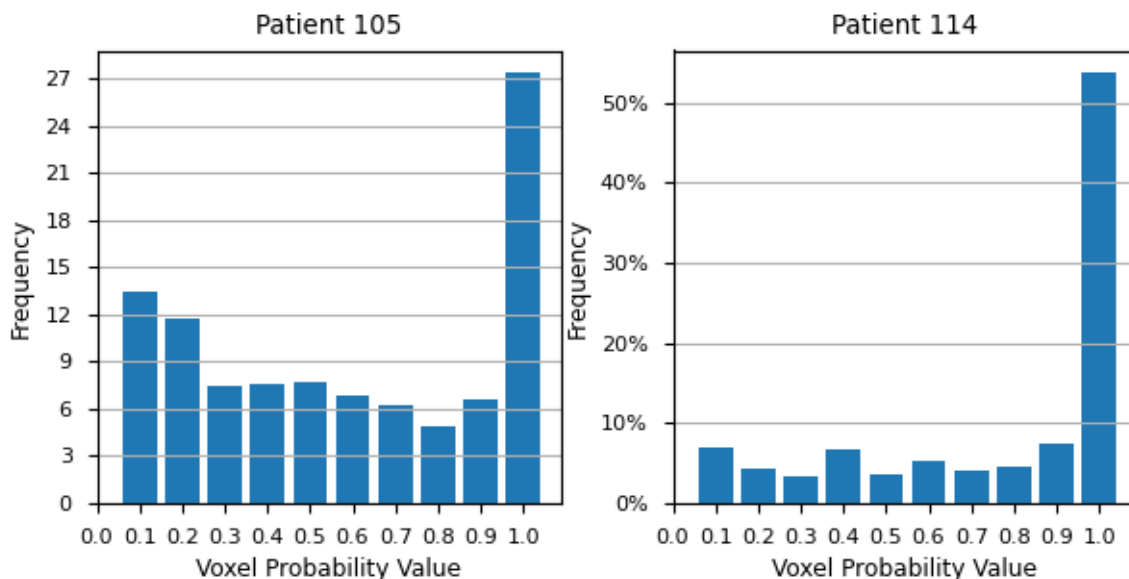
Figure 4.5: Frequency of voxel probability values within the TLP map of patient 105(left) and 114(right)

4.3 Angle Selection Validation

The constructed angle selection algorithm for proton beam therapy, utilised variations in water equivalent path length (ΔWEPL) and organs at risk percentage irradiation volume to optimise beam geometries against intra-fractional effects. To validate the effectiveness of our algorithm to identify plan quality, 36 single beam uniform treatment plans were generated for each patient. The RayStation script considered different beam geometries with couch angle fixed at 0° and gantry angle varied in 10° increments. Dosimetric information was accumulated from the deformed evaluated dose, incorporating all breathing phases.

Tumor coverage was assessed using dose reduction of the D95 and D98 metrics from the iCTV. The calculated dose reduction was obtained by subtracting the evaluated dose from the nominal plan dose as indicated in equation 4.2. A comparative analysis of the iCTV dose reduction as a function of ΔWEPL was thus performed.

$$iCTV\ Reduction\ _{D95,98} = D_{nominal} - D_{evaluated} \qquad (4.2)$$

Furthermore, accumulated dose to organs at risk was analysed by comparing dose parameters obtained from the deformed evaluated dose with the organs at risk percentage irradiated volume. Dose parameters considered for the inspected organs in this study were previously defined in section 3.5.1.

The obtained results plotted as a function of angle, demonstrated the impact of varying incident beam angle configurations on the evaluated dose parameters and predicted beam simulation results. Additionally, Pearson Correlation Coefficient (PCC) analysis was performed to quantify the linear statistical correlation between the extracted dose and corresponding beam simulation metrics for the tumor and organs at risk.

Visualisation of the graphs for patient 100 are depicted in Figure 4.6 and 4.7. Graphs on the left denote the effect of the incident beam geometry on the tumor in Figure 4.7 and organs at risk in Figure 4.6, where the top graph was our algorithm results and the ones beneath depict the extracted dose metric from each plan. Additionally, on the right we inspect the correlation graphs between the simulated and evaluated dataset for the tumour and all organs at risk investigated.
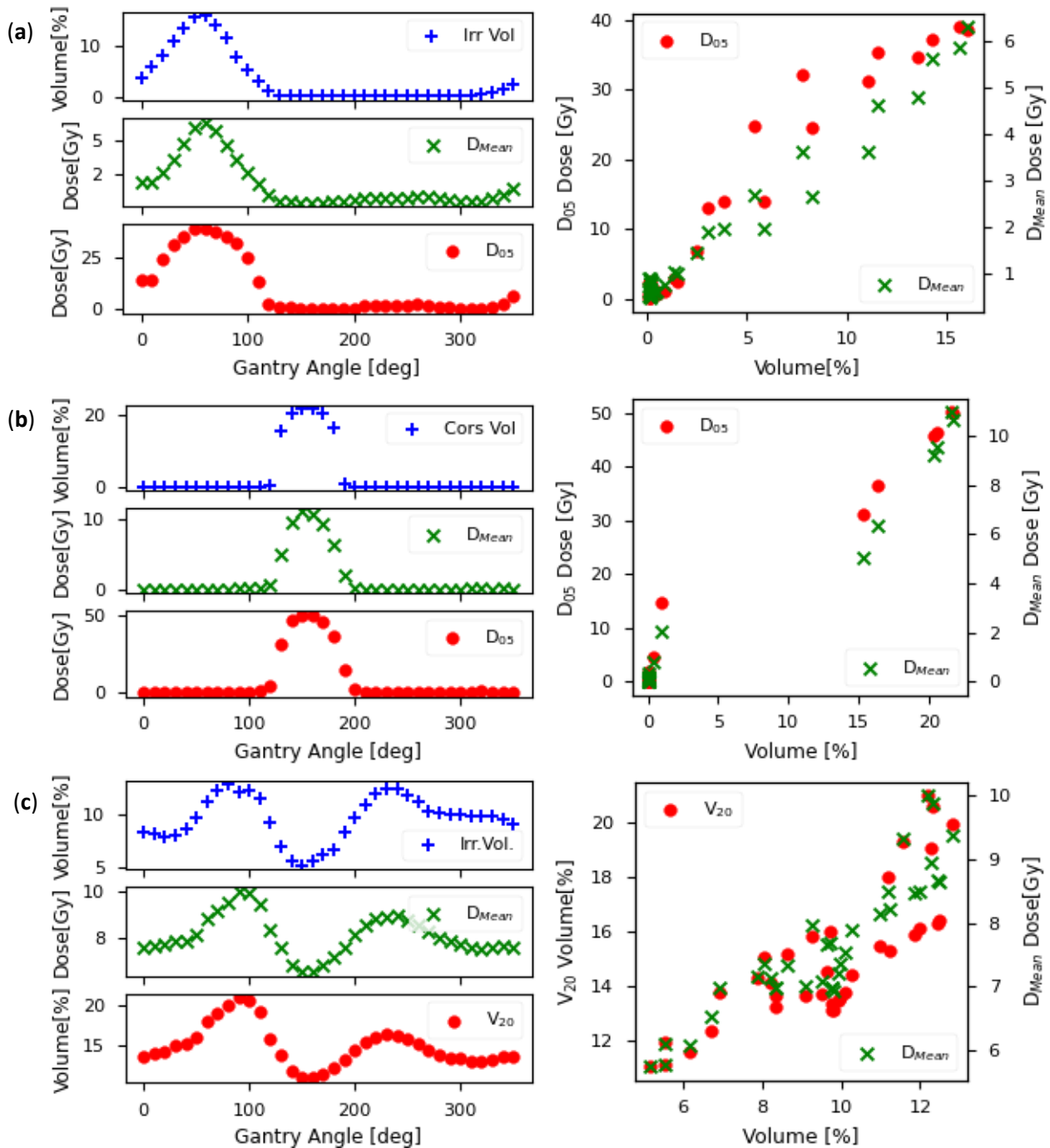
Figure 4.6: demonstrates the validation plan dose analysis for angle selection. The effects of incident beam geometry on the heart (a), spinal cord (b), and lung (c) are depicted on the left side of the figure. The top portion shows the percentage of the irradiated organ, while the plan dosimetric evaluation is presented below. The right side of the figure displays the correlation between the expected and measured effects of the incident angle.
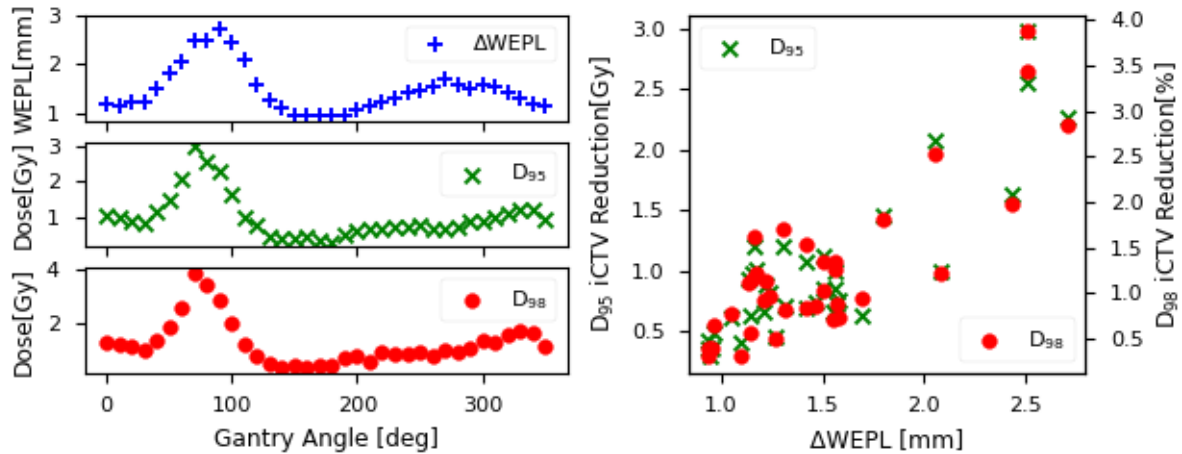
Figure 4.7: Angle selection validation plan dose analysis. Effects of incident beam geometry on tumour dose degradation, with ΔWEPL, ΔD95 ΔD98 on the left. Correlation between ΔWEPL and dose degradation right

With dose information being accumulated for all patients within our dataset, the PCC statistical test was performed with the respective findings of the angle selection algorithm. Figure 4.8 depicts the evaluated correlation values from the whole dataset for all dose variables. Correlation between computed ΔWEPL with tumour dose degradation and organ irradiation with accumulated dose is consistently high across the dataset. Patients 107 and 108 were excluded from the heart correlation calculations, as they exhibited no heart irradiation for the investigated beam angles. In all investigated cases, the suggested measure indicated a strong correlation with the corresponding dose variable, across all examined beam angles. Observed positive correlation validates that the effectiveness of the angle selection algorithm in identifying robust beam angles against target dose degradation from breathing induced alterations. Additionally, the algorithm depicted the ability to identify incident angles that exhibit relatively reduced dose to inspected organs.
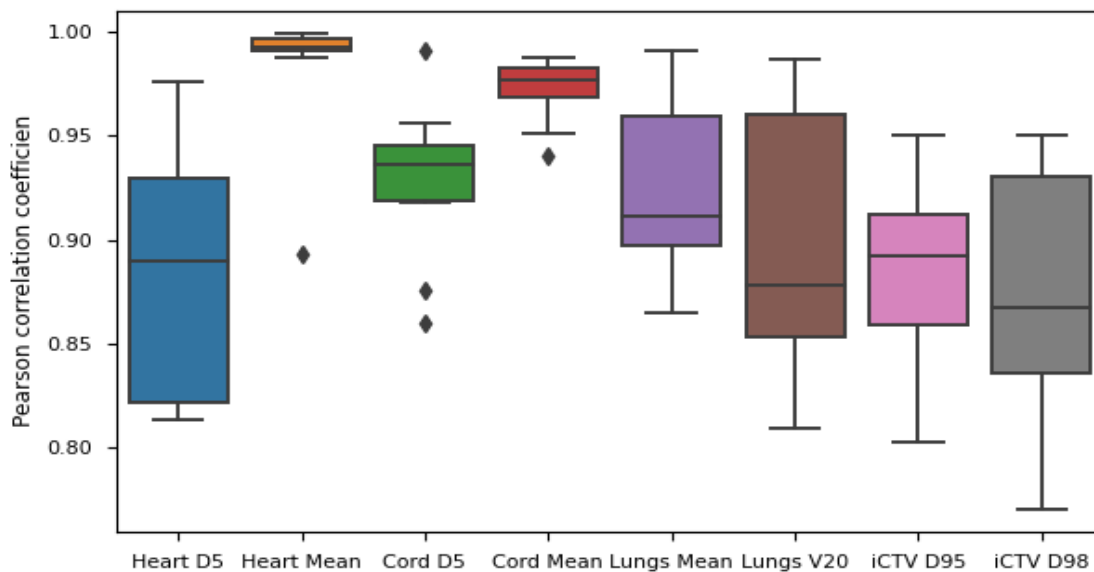

Figure 4.8: PCC between ΔWEPL and iCTV dose reduction and OAR percentage irradiation with organ dose paramteres for all investigated organs at risk.

4.3.2 Patient Specific Optimal Beam Geometry.

The constructed angle selection algorithm was able to identify optimal beam angles for a single variable such as tumor coverage. In a clinical treatment planning process however, the treatment planner must assess plan objective and make appropriate compromises. From inspection of the organ irradiation and ΔWEPL analysis maps in section 3.4.2 we identify that there is no optimal beam angle that minimises dose to all organs at risk while maintaining robustness of tumour coverage. For example, dose to spinal cord was compromised in the angle selection for patient 100, enabling the use of beam angles that irradiate the cord to some extend to maintain high quality of other parameters. Therefore, comparison of treatment plans utilising optimal beam angles (OA) and worst beam angles (WA) geometries was performed, to evaluate the Z-score maps ability to identify optimal beam angle combinations.

Optimal and Worst angle combinations are a three-angle combination that maximises and minimises the cumulative Z-score respectively. Since we impose a 20° angle separation on the optima angles to negate beam overlap, the same assumption will hold true for the worst angles. For patient 100, the three optimal couch, gantry combinations were (0,150), (0,190) and (-60,20) while the three worst combinations were (15,70), (-30,240) and (-30,260). The two generated treatment plans are portrayed in *Figure 4.9*, with the optimal beams on the left and worst beams on the right.
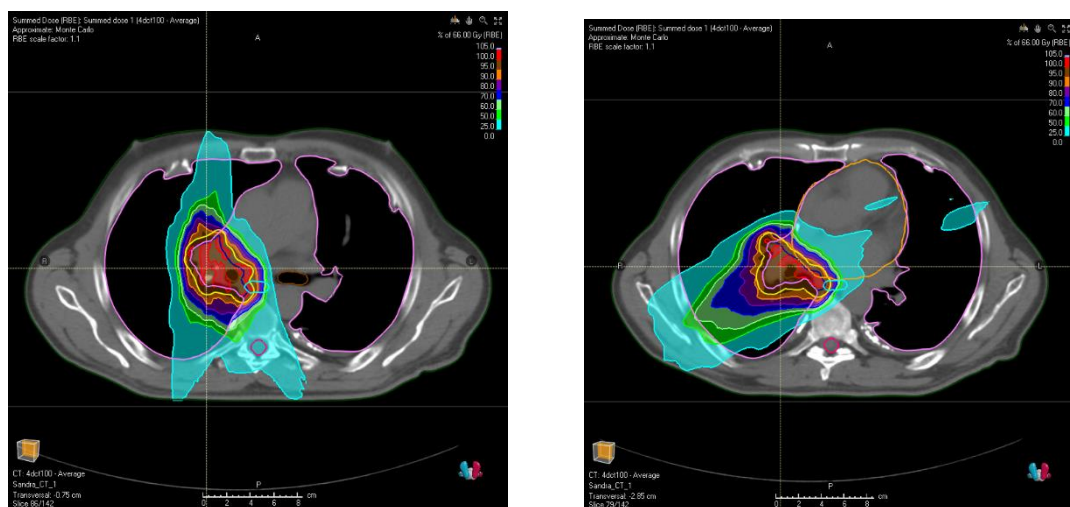
Figure 4.9: Generated treatment plans for patient 100 with optimal (left) and worst (right) beam angles.

By comparing the iCTV dose volume histogram (DVH) of the two treatment plans, we can observe dose deviations from the nominal. Inspection of *Figure 4.10* depicts that tumour coverage is significantly worse for the worst angle plan, with the DVH experiencing an overall shift to lower doses. Therefore, we conclude that the optimal beam geometry is more robust to intrafractional motion effects on tumour coverage. Subsequently, a similar inspection of the organs at risk DVH was performed. A significant reduction in the accumulated dose in the lungs and heart can be observed, while dose to

spinal cord increased in the optimal beam angle plan. The increase in the spinal cord dose was expected as one of the three beams' traverses through the spinal cord as seen in figure 3.8 and was the chosen compromise during angle selection. Through our angle selection we do not completely neglect the spinal cord irradiation, but, with the lower imposed weighting factor, we allow for partial irradiation if needed. However, the maximum dose received by the spinal cord was reported at approximately 25Gy which is significantly less than the accepted dose of 51Gy from the OUH guidelines.
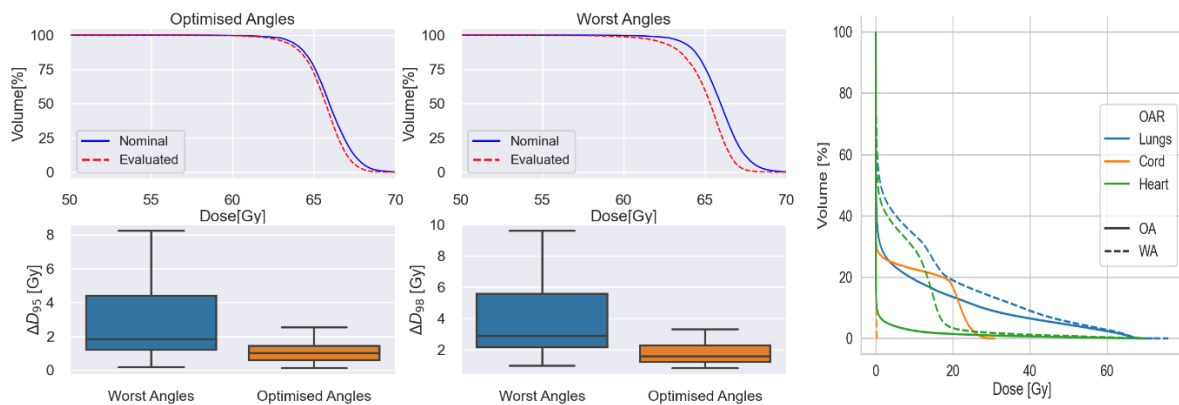
Figure 4.10: Right: Dose volume histogram (DVH) for OAR for the optimial anles plan and the worst angle plan (dotted line). Left: iCTV DVHs for both plans (top) and D98 - D95 reduction from nominal dose (bottom).

To conclude, through our angle selection algorithm we demonstrated a method to identify robust angle combinations against intrafractional motion while taking into consideration dose to organs at risk. The patient specific generated data extracted from the algorithm provide valued information to the treatment planner, enabling him to adjust and compromise between plan objectives during the angle selection procedure. The identified optimal beam orientations for all patients are reported in *Table 4.4.*

Patient	Angle 1	Angle 2	Angle 3	Tumour	Lungs	Heart	Cord
100	0,150	0,190	-60,20	2.0	1.0	1.5	0.5
101	0,180	-30,60	-60,30	2.0	1.0	1.5	0.5
102	-90,170	-15,160	15,210	2.0	1.5	1.0	0.5
104	-90,20	-30,30	-30,50	2.0	1.5	1.0	0.5
105	-60,200	0,170	15,190	2.0	1.0	1.5	0.5
106	-90,20	-45,30	-30,50	2.0	1.0	1.5	0.5
107	0,180	0,140	0,160	2.0	1.8	0.5	0.5
108	15,200	15,240	15,260	2.0	1.8	0.5	0.5
110	-90,175	-15,160	15,210	2.0	1.5	0.5	1.0
111	-45,170	30,60	60,50	2.0	1.5	0.5	1.0
114	-90,150	-90,170	-15,160	2.0	1.5	1.0	0.5

Table 4.4 The identified optimal angle and subsequent variable weighting factors for all patients are reported in table, where angles are present in a couch, gantry angle orientation.

4.4 3D vs 4D Robust Optimisation

A comprehensive dosimetric evaluation of the treatment plans generated using both the 3D and 4D robust optimisation techniques was performed. Primary objective was to investigate the plan robustness against intra-fractional motion and the subsequent impact on organs at risk. Respiratory effects on plan degradation were evaluated by employing the conditions stated in section 3.5.2 and the extracted results are presented in *Table 4.5* for all plans. Depicted in *Figure 4.11* we visualise the 3D and 4D robustly generated treatment plans for patient 100 on the left and the subsequent dose distribution differences on the right.
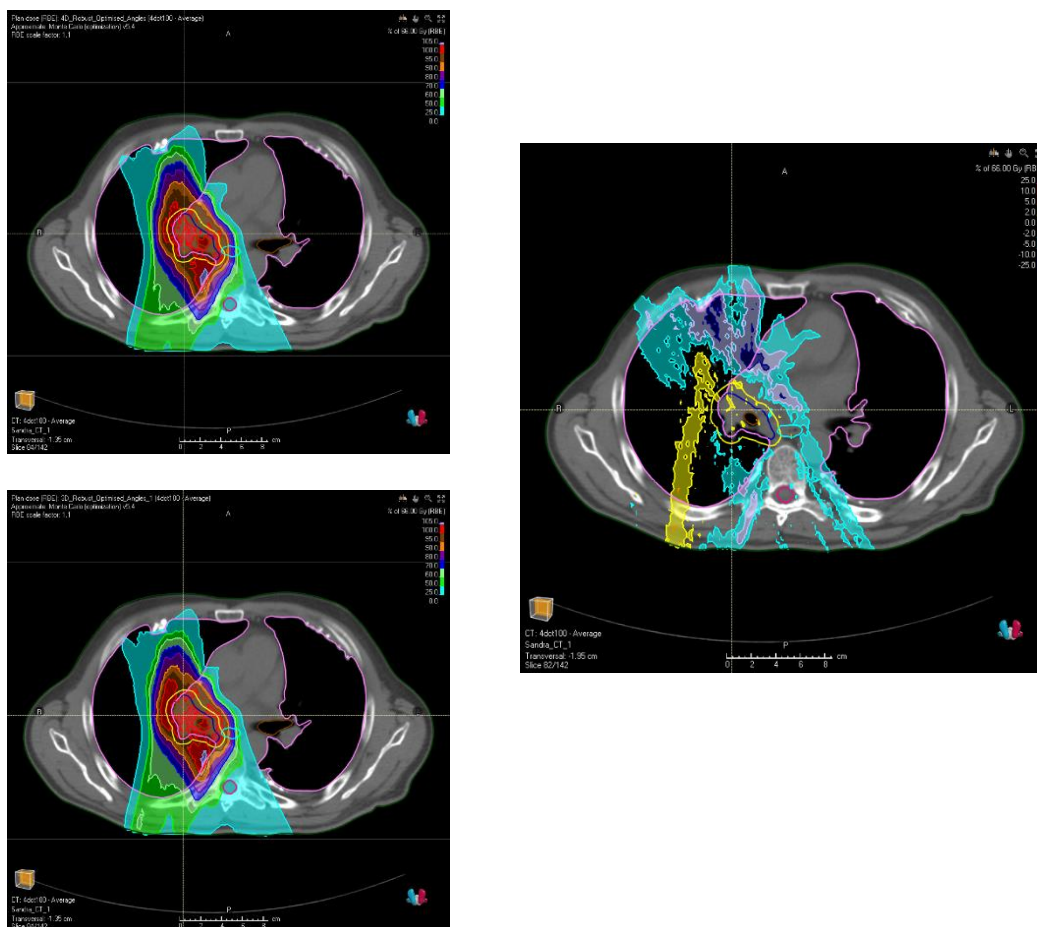
Figure 4.11: Left: 4D (top) and 3D (bottom) robustly optimised plans for patient 100. Right: difference between the 3D and 4D robustly optimised plans for patient 100. Dark blue contour indicates the iGTV and yellow contour the iCTV of the patient. Dose distributions are presented with grey for 105%, red for 100%, brown for 95%, orange for 90%, purple for 80%, blue for 70%, light green for 60%, dark green for 50% and light blue for less than 25% of the prescribed dose.

Patient		CTV V95 [%]	iCTV V95 [%]	iCTV D95 [Gy]	iCTV D98 [Gy]	HI [%]	BW Low [cGy]	BW High [cGy]
100	3D	99.92	99.91	64.80	64.44	5.56	31	32
	4D	99.98	99.98	64.98	64.68	4.99	14	29
101	3D	99.93	99.91	64.80	64.44	5.56	32	32
	4D	99.98	99.98	64.99	64.68	4.99	14	29
102	3D	100	99.98	64.93	64.61	4.98	15	25
	4D	99.98	99.91	64.80	64.42	5.12	15	25
104	3D	100	99.98	65.21	64.97	4.13	29	25
	4D	100	99.97	65.12	64.89	3.96	32	11
105	3D	99.97	99.71	64.88	64.42	6.36	86	29
	4D	100	99.83	64.90	64.48	6.00	64	27
106	3D	97.6	97.00	63.28	62.18	9.28	36	47
	4D	100	100	65.15	64.92	4.32	19	18
107	3D	100	100	65.08	64.81	3.99	22	20
	4D	100	100	65.20	64.97	3.65	21	19
108	3D	100	100	65.00	64.73	4.73	11	17
	4D	100	100	65.10	64.86	4.39	13	19
110	3D	99.69	99.60	65.16	64.86	4.81	59	41
	4D	100	100	65.09	64.82	4.54	8	50
111	3D	98.15	97.86	64.86	64.37	7.10	158	47
	4D	98.28	98.73	64.89	64.35	5.75	146	28
114	3D	99.37	98.77	64.67	64.18	6.99	57	65
	4D	99.88	99.18	64.87	64.46	6.35	29	50

Table 4.5: Tumour coverage criteria results extracted from the 3D and 4D robustly optimised plans for all patients. Values not highlighted met with criteria 1, while values highlighted with orange met with criteria 2 and red met no criteria.

Indicated in table 4.5 are the dose characterisation values of treatment plans evaluated in this study. Additionally, an assessment of how each value aligns with the predefined criteria is included, with values highlighted in orange indicate the corresponding value met with criteria two, and red failed to meet any criteria. Remaining values not highlighted, denote that dose characteristic met with criteria one, demonstrating an acceptable level. Evaluation of treatment plans revealed that the majority were found to be within the acceptable set criteria. This indicated that the employed optimisation strategies generated effective treatment plans with desired dose distribution effects for patients within our dataset.

Notably, application of 4D robust optimisation consistently met with the predetermined criteria without any failures. In contrast, 3D robustly optimised plans were successful for nine of the eleven patients. Specifically, the treatment plan for patient 111 exhibited an acceptable tumour coverage, however, depicted slightly unacceptable homogeneity characteristics. Moreover, treatment plan for patient 116 demonstrated significant tumour dose degradation and inhomogeneous dose deposition. For all patients where 3D robust optimisation was not able to generate an acceptable treatment plan, the application of 4D robust optimisation resulted in significant improvements.

Further investigation of patient 106 was conducted to gain an insight on why the 3D robust optimisation failed to provide an acceptable treatment plan. Inspection of the patient's tumour characteristic from Table 4.1, revealed a motion amplitude of 13.3mm and of particular importance a superior-inferior displacement of 13.2mm, broken down to 5.2mm and 8.0mm respectively. In the set Robust optimisation parameters, a 5mm isotropic margin of the CTV was incorporated which is significantly lower than the 8mm maximum displacement in the inferior direction. As only the

deformably registered CTV of the planning CT was incorporated in the optimisation procedure for the 3D plan, the used 5mm margin might have been insufficient to generate a robust against tumour motion treatment plan. On the contrary, in 4D robust optimisation where CTVs of all breathing phases were incorporated in the   plan optimisation, the generated plan was well within the acceptable criteria.

 From inspection of *Figure 4.12*, it is evident that the 3D optimised plan (left) exhibited significant dose degradation from the planned, while the 4D optimised plan closely resembled the nominal DVH. Dose reduction could be a result of an inadequate CTV margin employed in 3D robust optimisation. However, since only patient 106 demonstrated this particularly motion behaviour, our dataset is insufficient to draw definite conclusions. Further investigations should be performed, with a larger patient cohort that exhibits high tumour motion and directional displacement amplitudes.
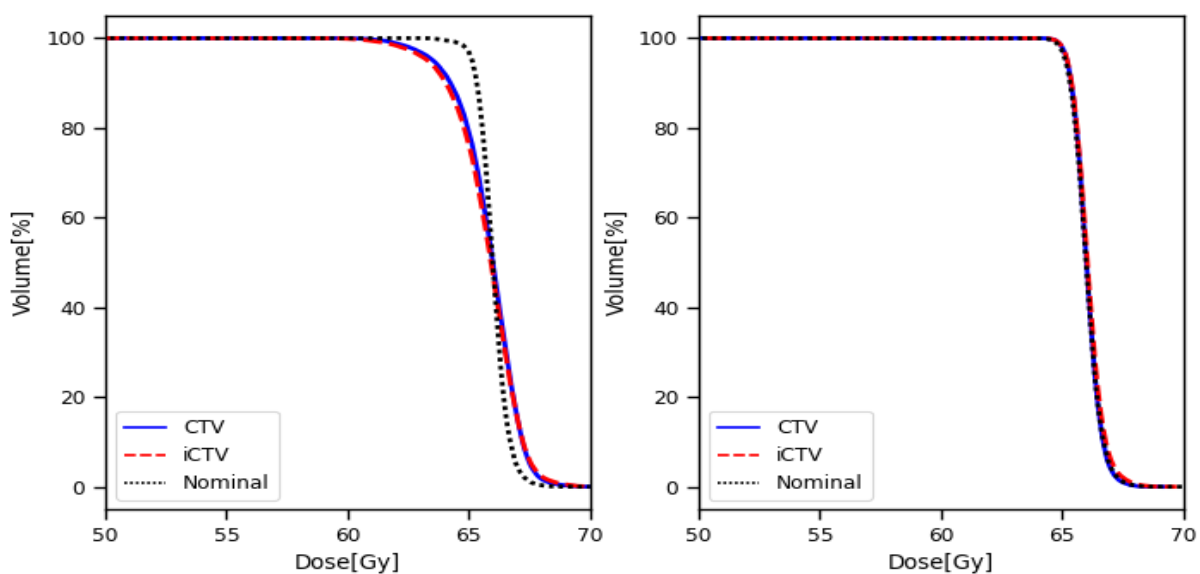

Figure 4.12: DVHs of planned iCTV and evaluated CTV and iCTV for 3D(left) and 4D(right) robustly optimised treatment plans of patient 106.

Comparative analysis of the evaluated tumour dose between the two optimisation strategies, 3D and 4D robust optimisation, is presented in *Figure 4.13.* A marginally improved tumour coverage is observed from the 4D plans indicated by the iCTV and CTV V95 and V98 graphs. The V95 graphs depict a generally similar tumour coverage with the population average recorded for the CTV at 99.5% for the 3D and 99.8% for the 4D plans, while for the iCTV and 99.2% and 99.7% respectively. However, the V98 plots demonstrate that the 4D plans maintained a higher tumour coverage at larger doses, with the reported CTV and iCTV V98 average values at 95.7% and 94.8% for 3D and 98.0% and 97.5% for 4D. This suggests the presence of a more abrupt dose fall-off for the 4D robustly optimised plan, comparable to the observed in Figure 3.9.

Investigated tumour dose measurements D95, D98, D2 and Dmean yield similar results for both optimisation strategies with the exception the 3D plan of patient 106. Tumour dose measurements for the majority of the patients were within an identical or clinically irrelevant range except patient 106 which stands out as an outlier in all plots.
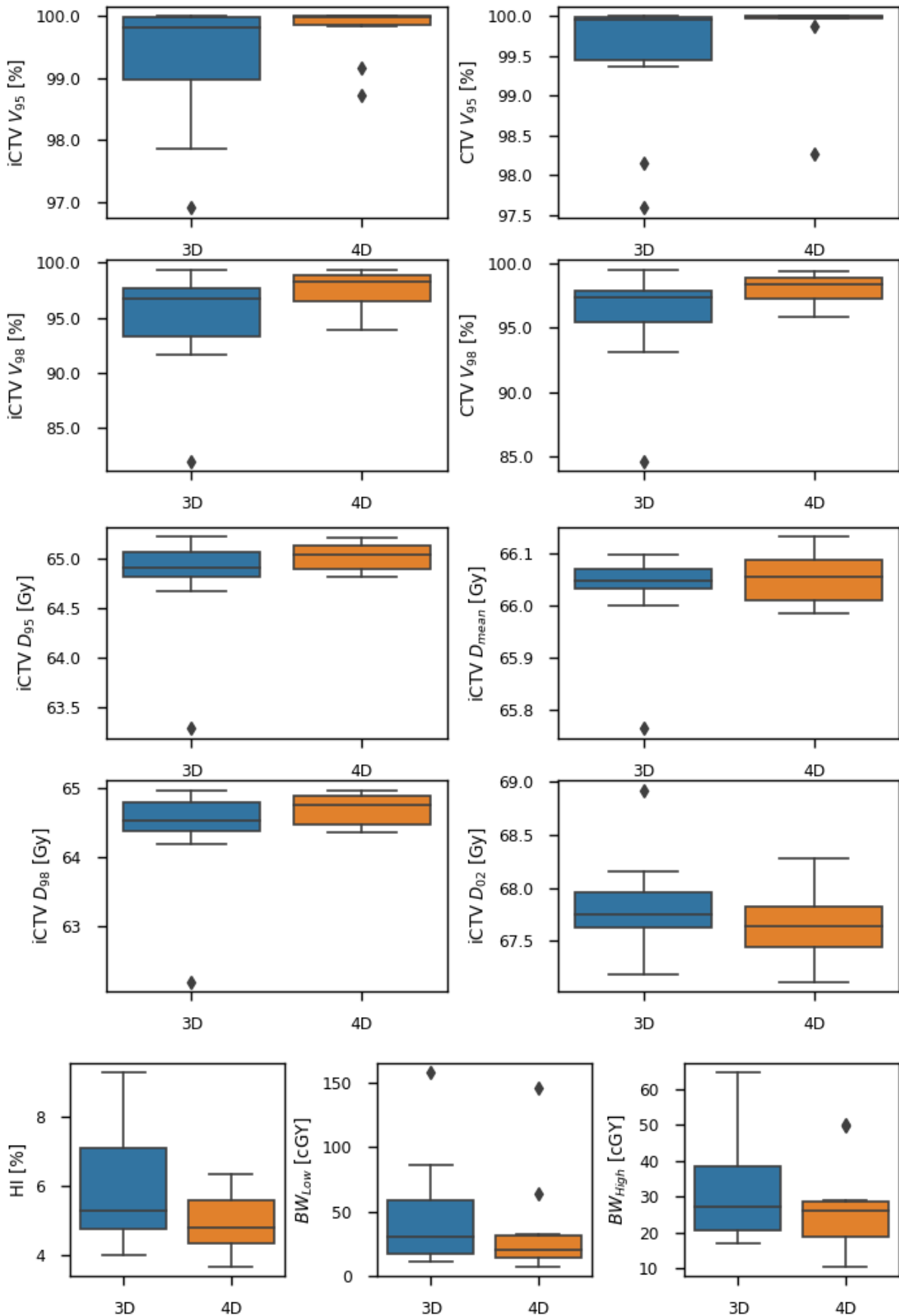
Figure 4.13: Comparison of 3D and 4D plans for tumour coverage with CTV and iCTV V95 and V98, tumour dose statistics with iCTV D95, D98, D02 and Dmean and homogeneity result investigated with HI, and DVH BW low and high.

The significant advantage of the 4D robust optimisation procedure becomes apparent in the dose homogeneity plots in Figure 4.10. Average reported homogeneity index was 5.87% for the 3D optimisation and 4.91% for the 4D optimisation. Accordingly, the average band width for low and high doses was measured at 48cGy and 32cGy for 3D and 36cGy 26cGy for 4D. It is evident that the 4D robust optimisation approach provided a more homogeneous dose distribution in all breathing phases compared to 3D, even though the average dose measurements where similar. This suggests that in 3D robust optimisation, some phases acquired higher dose while others accumulate less, resulting in a similar average dose as the 4D optimised plan, where each phase accumulated an approximately equal dose.
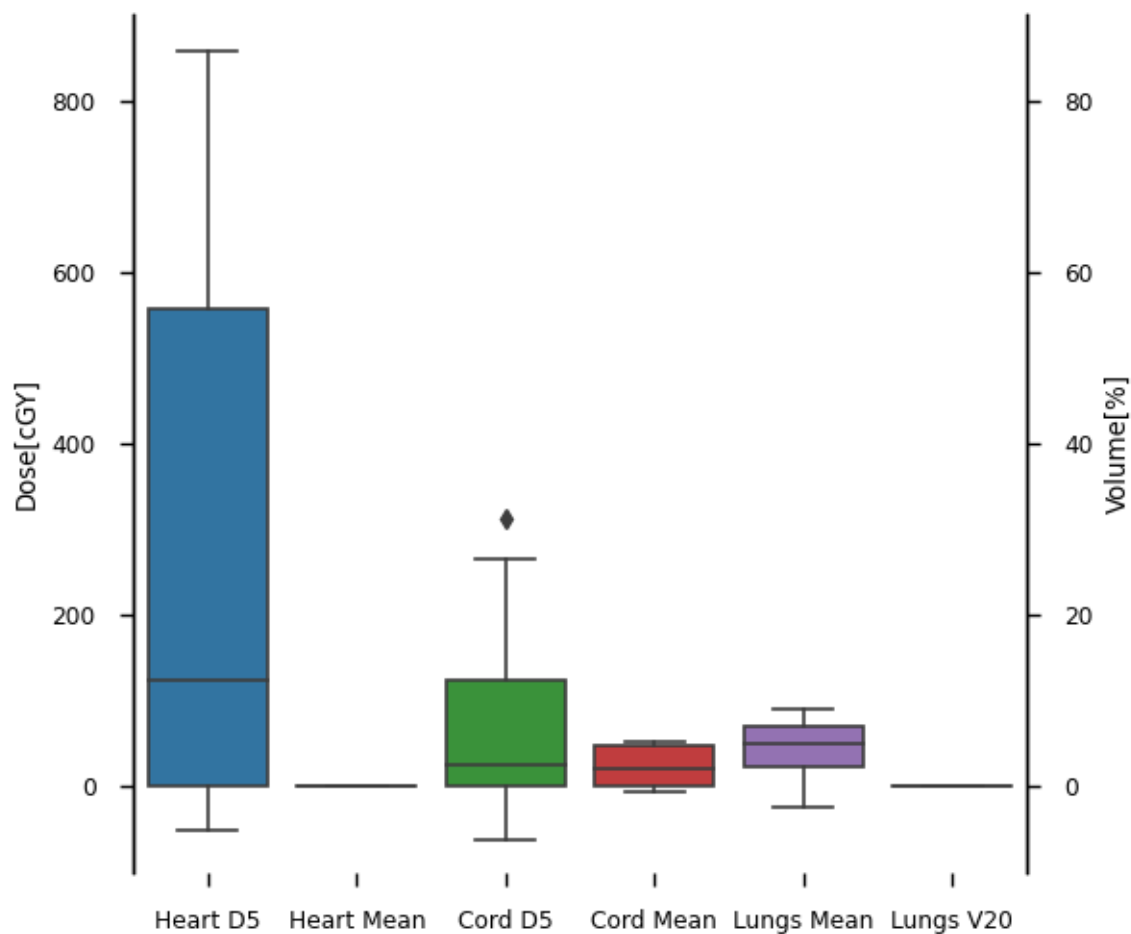
Figure 4.14: Difference in accumulated organ dose between the 4D and 3D robustly optimised plans

The more robust plans generated by 4D robust optimisation had consequently higher accumulated dose in organs at risk. Figure 4.11 illustrates the difference in accumulated organ dose between the 4D and 3D robustly optimised plans. The mean organ dose, particularly for the heart, remains identical, with only marginal increases observed for the spinal cord and lungs, averaging below 100cGy for the whole dataset. Irradiated lung volume, as indicated by the Lungs V20 variable, appears to be unaffected by the optimisation strategy. The volumetric dose variable, lungs V20 depicted insignificant

variation between 3D and 4D robustly optimised plan, possibly due to the identical incident beam geometries utilised in both cases.

However, higher extreme doses can be observed in the 4D robustly optimised plans as depicted by the heart and cord D5 plots. Larger margin volumes utilised in 4D robust optimisation approach could contributed to a higher accumulated dose to organs at risk with the reported average D5 difference at 290cGy for the heart and 85cGy for the Cord. This effect seems to be more prominent for some patient with the maximum reported heart D5 at 858cGy for patient 111, while for the spinal cord at 320cGy for patient 110. The observed effect could also be induced by the spot optimisation process and should be analysed with a more patient-specific approach. It is worth noting that no high dose variable was evaluated for the lungs due to the closer proximity to the tumour. As mentioned in previous sections, the CTV was cropped at the lungs and not the iCTV. A more homogeneous tumour dose distribution would thus inherently increase Lung dose.

In conclusion, the comparison between 4D and 3D robust optimisation processes emphasised the advantages of 4D optimisation in terms of robustness against intra-fractional motion effects, tumour coverage, and dose homogeneity. While 3D optimisation was generally successful, 4D optimisation demonstrated superior performance, particularly in handling complex motion patterns and achieving a more homogeneous dose distribution. However, it is important to acknowledge that these advantages were accompanied by a higher accumulated organs at risk dose. The trade-off between improved target coverage and increased dose to organs at risk should be carefully evaluated on case by case as the effect seem to be more prominent for some patients.

5. Discussion.

In this study the ability to extract patient specific respiratory information from 4D CT scans to minimise and estimate intrafractional motion effects on plan quality was evaluated. Our developed algorithms successfully identified optimal beam geometries that minimised tumour dose degradation while considering organs at risk. The conducted ΔWEPL analysis was able to identify the extend of tumour dose degradation, with the average correlation for D95 and D98 reduction estimated at 0.89 and 0.88 respectively, thus accepting our first hypothesis. Additionally, OAR percentage irradiation was strongly correlated with accumulated organ dose, with average correlations reported at 0.88 for heart D5, 0.98 for heart Dmean, 0.92 for cord D5, 0.97 for cord Dmean, 0.93 for lungs Dmean and 0.90 for lungs V20. Therefore, our second hypothesis was also accepted. Furthermore, a comprehensive analysis of tumour motion was conducted by investigating both translational displacement and volumetric variations during respiration. Lastly, a comparative analysis of the effectiveness of 3D and 4D robust optimisation strategies to account for intrafractional uncertainties was performed. A minor improvement was observed from the 4D optimised plans; however, the 3D robust optimisation was able to generate robust plans within our acceptable criteria for all patients except one. Therefore, a study with a larger patient cohort consisting of tumours with more pronounced motion is required before accepting our last hypothesis.

5.1 HULT Uncertainties.

In this study, the Hounsfield unit to stopping power calibration of the Hounsfield Unit Look-Up table (HULT) followed the stoichiometric calibration method described by Schneider et al [58]. The CT Hounsfield units were converted to relative electron densities and relative proton stopping powers utilising tissue substitution values. However, due to the unavailability of the CT scanner used for image acquisition, it was not possible to directly verify the accuracy of the conversion table employed in this study. The accompanying paper of the dataset provided relative electron density to HU conversions, but the associated methodology and uncertainties were not specified. To quantify the uncertainty of the converted RSP, experimental validation should have been performed using phantom measurements. The accuracy of the RSP conversion is influenced by factors such as image quality and estimation of tissue substitution values. Previous studies utilising similar HULTs reported mean relative errors of approximately 3% to 3.5%, highlighting the importance of ensuring accurate conversions for implementation in proton therapy treatment planning [79,80,81].

The uncertainties associated with the relative electron density conversions utilised for the creation of the HULT used in this study are important to consider. Demonstrated in literature and our results for the K conversion factor, suggest a close relationship between relative electron density and relative proton stopping power for identical tissues. Therefore, the inherited uncertainties of relative electron

density propagate to the RSP conversion. The main sources of error in the relative electron density conversion arise from uncertainties of the phantom CT images and calculation errors involved in the determination of the scanner characteristic k-values. Furthermore, direct calibration of CT data using tissue substitutions relies on approximations of the chemical composition and density of real tissues. It is not possible to produce tissue substitutes with exact specifications as real tissue. In addition, random variations that occur like for instance the variation of hydrogen content, could produce significant differences in proton stopping power [58]. Additionally, the tissue substitution values used in this study were extracted from the ICRU 1989, which were primarily developed for radiobiology and radiation dosimetry applications. Schneider et al have pointed out that the tissue substitution values used may not fully meet specific requirements for radiotherapy [58]. These factors contribute to the overall uncertainty in the accuracy of the RSP conversion and should be taken into consideration in the interpretation of the results.

5.2 ΔWEPL for Angle selection.

In our study, we employed the HULT to assess the variation in water equivalent path length (ΔWEPL) between planning and evaluated CT scans for different couch-gantry angles. This approach enabled us to evaluate the robustness of various beam geometries against dose degradation caused from respiratory induced anatomical changes. This implementation could be adapted to meet clinical requirements of proton therapy treatment planning of lung cancer.

Proposed adaptations of our algorithm include the use of higher angle increments during an initial iteration off couch and gantry angles and the implementation of restrictions to irradiation areas. By using higher angle increments we can identify regions with more robust angles, allowing for a more detailed investigation in subsequent iterations with smaller angle increments. Furthermore, by implementing restrictions on irradiation areas, such as avoiding irradiation of the cross lateral lung, we can avoid unnecessary computations. This reduction in computational time from the proposed adaptations, makes it more feasible for integration of our algorithm into clinical workflow. Moreover, we propose the integration of this methodology into the optimisation algorithm procedure. By calculating the ΔWEPL at the allocated spot positions instead of the tumour distal edge, we could incorporate it as a penalty factor in the intensity-modulated proton therapy optimisation algorithm. This approach would help identify more robust spots within the entire beam and increase their relative intensity, potentially leading to improved plan quality.

Finally, the approach we described can be utilised as a tool to assess interfractional changes in WEPL. During the course of the treatment, variations in patients' anatomy and tumour size may occur, potentially leading to suboptimal treatment delivery. By employing WEPL analysis, we can evaluate the efficacy of the current treatment plan to deliver an adequate and robust dose to the tumour and identify the need for plan adaptations. By comparing the WEPL values from the initial CT scan with ones acquired from the daily cone-beam CT (CBCT) scan before dose delivery, we can potentially quantify variations in the path length and assess their impact on plan quality. If significant variations

are observed, indicating a noteworthy deviation between planned and actual treatment conditions, a repeat CT scan and subsequent plan adaptations could be considered. Incorporating the CBCT scan into our approach allows us to access real-time anatomical information during the treatment course. However, it is important to note that there are inherent variations between the CBCT and CT scan, such as image quality and accuracy. Therefore, while the CBCT scan provides valuable information into anatomical variations, it may not be sufficient for precise quantitative analysis. For cases where severe anatomical changes are observed from the WEPL analysis on the CBCT, a repeat CT scan could be employed. The repeat scan depicts a more comprehensive representation of the patient's current anatomy, enabling plan evaluation and considered plan adaptations. Therefore, by utilising the WEPL analysis on the CBCT scan as a trigger for potential anatomical variations and subsequent repeat CT scans, we incorporate real-time monitoring of the treatment without the need for excess imaging.

Such adaptations have the potential of enhancing the robustness and efficacy of proton therapy for lung cancer, ultimately improving the overall treatment outcomes for patients and are worth further investigation.

5.3 Interplay Effect

Interplay effects resulting from intrafraction motion during pencil beam scanning delivery were not investigated in our study. This effect occurs when dose deposition takes place on a moving target, leading to deviations between delivered and planned dose. Lack of synchronisation between beam delivery and tumour desired position results in a shift of the steep dose gradients and subsequent dose degradation such as regions of over-dosage and under-dosage [82]. To evaluate interplay effects, a 4D dynamic dose must be constructed, as they are not apparent in the 4D evaluated dose utilised in our study. To achieve this, the precise spot delivery time could be extracted from the treatment delivery logs via RayStation and utilised to bin the specific spot to the appropriate CT scan from the breathing cycle. By randomly identifying the initial phase and iterating spot binning for all delivered spots, a dynamic dose considering temporal dynamics of beam delivery and tumour motion could be constructed.

Minimisation of interplay effects can be achieved through two main approaches, tumour motion suppression or beam rescanning. Rescanning techniques involve splitting the beam's monetary units and delivering multiple times per fraction, simulating a higher fractionation schedule. The random hot and cold dose spots induced from interplay are averaged over the multiple beam scans, to achieve a smooth dose heterogeneity. Rescanning modalities implemented are, layer rescanning where each energy is scanned multiple times before moving to the next one and volumetric rescanning, where all energy layers are delivered and then repeated [83, 84].

Interplay effects were not evaluated in our study due to several reasons. Firstly, accurate construction of the dynamic dose requires sub-second precision of the CT scans, which can be acquired through the patient's breathing curve. However, the corresponding breathing curves or time gating information utilised for the creation of the 4D CT scan were not available for our dataset. Assumptions made for the entire dataset would not accurately represent each patient's individual breathing pattern

and thus the observed interplay effects would not have been representative. Additionally, interplay effects are primarily relevant for hypofractionation therapies as reported by several studies. The normal fractionation schedule in conjunction with multiple beams per fractionation utilised in our study substantially minimise interplay effects. The averaging effect over the multiple fractions in the conventional fractionation helps mitigate the random over- and under- dose regions associated with interplay effects, to achieve a homogeneous dose similar to rescanning methods. As stated by Phua et al, to mathematically nullify interplay effects, an integration over infinite number of fractions and breathing cycles is required. However, in practice they state that a similar effect could be accomplished from conventional fractionation of typically 30 fractions of 2 Gy for proton therapy of lung cancer [85]. Furthermore, since each beam would experience interplay effect, the random dose spots generated over a single fraction would contribute to the averaging effect, leading to a final homogeneous dose distribution. Therefore, the observed interplay effect in our study would be minimal for the conventional fractionated treatment plans generated.

Several studies attempted to establish a correlation between the extent of dose degradation caused by interplay effects and the observed tumour motion of the patient. However, these attempts have been unsuccessful thus far. Current clinical implementation is the evaluation of interplay effects for each patient and the use of volumetric rescanning combined with motion compensation techniques to mitigate the impact [86,87].

For future research, it would be valuable to investigate interplay effects further and explore the possibility of correlating their severity with the Tumour Location Probability (TLP) map. The TLP map provides voxel probabilities that describe the likelihood of tumour's presence within each voxel through the breathing cycle. By examining the beam scanning process utilising the irradiated voxels' probability, we could potentially get an insight into the relationship between interplay effect and the patient-specific intrafractional motion. Additionally, the possibility to optimise beam scanning direction with regards to the patient specific motion could be investigated. A simulation of scanning direction over the TLP map and breathing phases could provide information to identify scanning or incident beam orientations more robust against interplay. This avenue of investigation holds promise for enhancing our understanding of interplay effects and improve the current treatment planning strategies in proton therapy of lung cancer.

5.4 Tumour motion in Proton Therapy.

Tumour motion during irradiation is accounted within the PTV margin in conventional X-ray therapy, which is not utilised in active-scanning proton therapy as discussed previously. To minimise geometrical misses in IMPT, population-based or individual margins are employed in the plan optimisation procedure in conjunction with robust optimisation strategies [88]. Several methodologies to generate population-based margins have been proposed in literature, with the one most commonly used being the "Van Herk recipe" [89]. The estimated margin around the CTV is constructed so that it ensures 95% of the prescribed dose is delivered on the CTV for 90% of patients.

The margin is calculated by considering both systematic and random errors. Systematic errors are described by the broadening of the proton beam penumbra; therefore, a cumulative Gaussian modelling is employed. In proton beam therapy of lung cancer, the broadening of the penumbra is caused by the increased range of the secondary electrons that lead to subsequent blurring of the dose distribution. This effect dominates the cumulative dose effects with additional random error margins being relatively small. Individualised margins employ target volumes like the iGTV and iCTV that encompass all motion and shape variations over the respiration cycle and was the preferred method employed in this study. Additional individualised margins like the mid-position (MidP) technique can be employed and was shown to reduce target volumes without compromising target coverage when compared with the ITV [90,91]. The MidP volume is extracted by investigating the time-average position of the tumour and motion standard deviation derived for each patient from the 4D CT scan. The presence of four-dimensional imaging has been the therapeutic standard of care in lung cancer radiotherapy. Respiratory induced changes can be identified from the 4DCT enabling the treatment planner to design the treatment in patient specific manner [90]. These methods ensure that no systematic errors of intrafractional motion enter the treatment planning process and are preferred over population-based procedures clinically.

5.5 Robust Optimisation Strategies.

In our study we evaluated the efficacy of both 3D and 4D robust optimisation strategies to account for tumour motion effects during respiration. Target volume of the constructed treatment plans was the CTV, with optimisation parameters set on the ITV and iCTV to minimise geometrical misses. Subsequently, a 5mm isotropic margin of the CTV was employed on each beam to ensure sufficient tumour coverage. The isotropic expansion of the CTV also accounted for set-up uncertainties which were not investigated in this study. By employing robust angles against intra-fractional motion effects in conjunction with a 3.5% range uncertainty of the robust optimisation, we ensure the minimisation of range effects on degradation of the dose distribution.

Evaluation of both optimisation strategies in relation to tumour motion revealed that both procedures were successfully in generating robust treatment plans for the majority of the patients. Minor improvements were observed in the 4D robustly optimised plans; nevertheless, 3D robust optimisation was able to generate acceptable treatment plans for all patients except one. However, the observed tumour motions within our dataset were relatively small, with the average motion amplitude reported at 7.75mm and the maximum at 13.27mm. Only for patient 106 with the highest exhibited motion amplitude of our sample, was 3D robust optimisation not able to generate an acceptable treatment plan. The significant plan degradation observed could have been caused due to insufficient margins set in the robust optimisation procedure. However, a larger patient cohort with more profound tumour motion amplitudes should be investigated to derive significant conclusions.

In future research, exploring the integration of patient-specific optimisation margins within the 3D robust optimisation process would be valuable. Current clinical implementation is to employ an

isotropic margin to account for setup and motion uncertainties. Therefore, utilising directional motion amplitude as motion margins, could potentially enhance the effectiveness of 3D robust optimisation. However, to achieve this it is important to deconvolve the contribution of the set up and tumour motion factors in the robust optimisation margin. By incorporating the specific directional motion factors, the 3D optimisation process can take into account unique characteristics of each patient's tumour motion. A higher margin can thus be implemented to account for higher motion in specific planes, while the lower margins can reduce target volume and consequently reduce dose to organs at risk. The more personalised approach for 3D robust optimisation might improve plan robustness by incorporating patient specific motion parameters similar to 4D robust optimisation.

5.6 Motion management.

Treatment plans generated in our study where designed to be delivered during free breathing, without considering any motion management techniques. However, several motion management methods have been proposed in literature and are in use in clinical practice [92]. One such technique is Breath Hold or Deep Inspiration Breath Hold (DIBH), where patients hold their breath during delivery of radiation. This technique immobilises lung tumours and reduces lung density, allowing for a reduction in the volume of normal lung tissue receiving high dose of radiation. However, this technique requires patients to hold their breath for a duration of 15-20 seconds, which may not be feasible for all patients depending on their physical condition [93,94].

Another technique is amplitude gating, where the radiation beam is delivered only when the tumour moves within a desired range of positions. Real-time monitoring of the target position is essential for this technique, which can be achieved by utilising an external surrogate signal similar to 4D CT scan acquisition, or through internal target monitoring using real-time X-ray fluoroscopy imaging. To achieve an acceptable treatment time and maintain a clinically acceptable level of dose preservation, it is important to determine the most reproducible and stable phases of the respiratory cycle and define the suitable gating window. Exhalation gating, using phases in the range of 30% to 70% depending on the patient's breathing pattern, is commonly used clinically due to their stability[94,95].

Abdominal compressions or diaphragm suppression are another method employed for lung tumour located near the diaphragm. By suppressing diaphragm motion, tumour motion can potentially be reduced. However, this method may not be as effective for tumours situated in other lung regions and is most commonly used clinically for stereotactic lung or liver cancer treatments [96,97].

The identification of an appropriate motion management technique for each patient should be based on their specific tumour characteristics and physical condition. However, certain limitations exist with each technique. BH and DIBH, particularly for lung cancer patients may not be able to sustain breath holding for extended periods during treatment. Gating techniques require a stable, predictable and reproduceable breathing pattern, which may not be achieved in some patients with erratic respiration. Moreover, patients may experience alteration of their breathing pattern due to stress encountered during imaging and treatment. In certain cases, patients may not require any motion management or

may perceive the reproducibility of such techniques as insufficient, thus opting for treatment during free breathing.

In our study, the angle selection algorithm was designed under the assumption of free breathing and encompassed all breathing phases in the calculations. Nevertheless, our algorithm can be readily modified to incorporate any of the aforementioned motion management techniques by integrating images acquired with the application of the respective motion management technique. The versatility of our algorithm enables the treatment planner to identify optimal beam geometries for a wide range of cases, regardless of whether motion management techniques are employed or not.

6. Conclusion

This thesis aimed to investigate the intrafractional motion of locally advanced non-small cell lung cancer patients in order to enhance therapeutic outcomes for intensity modulated proton beam therapy. The study focused on assessing the feasibility of using water equivalent path length (WEPL) analysis as a tool for identifying robust angles that mitigate the effects of intrafractional motion. This was achieved through a comparison of the variation in WEPL (ΔWEPL) with the corresponding dose degradation of the clinical target volume (ΔD95, ΔD98) between the planning and evaluated CT scans. Strong positive correlations were observed, with population average Pearson coefficient of 0.89 for ΔD95 and 0.89 for ΔD98, indicating the potential of WEPL analysis in identifying the effect of target dose degradation.

Furthermore, the impact of the incident beam orientation on the heart, lungs and spinal cord, was investigated. The percentage irradiated organ volume with accumulated dose (D5, Dmean, V20) was compared to assess the organ specific effect. The analysis revealed significant correlations, with the average Pearson coefficients of 0.88 for heart D5, 0.98 for heart Dmean, 0.93 for spinal cord D5, 0.97 for spinal cord Dmean, 0.90 for lungs Dmean and 0.89 for lungs V20, emphasising the influence of beam orientation on organ dose.

To facilitate the identification of optimal beam geometries, an angle selection algorithm was developed. This algorithm successfully identified the tumour distal edge and generated a beam simulation to assess the impact of different incident beam geometries on the tumour and organs at risk. By evaluating 350 unique couch-gantry angle combinations, the algorithm constructed 2D maps illustrating the effects of incident beam on the tumour and investigated organs. To normalise the significance of these effects, a Z-score statistical transformation was performed, with patient-specific anatomy and information from the ΔWEPL and organ irradiation maps taken into consideration in the format of weighting factors for each map. By aggregating the weighted maps, a final Z-score map was generated and through the process of minimisation, the algorithm successfully identified the three optimal incident beam geometries, with a 20° angle separation.

In addition to the angle selection algorithm, a comprehensive analysis of tumour motion was conducted utilising our tumour motion algorithm. The analysis involved evaluating motion amplitude, volumetric variation and the construction of a Tumour Location Probability map for each patient. Subsequently, 3D and 4D robust optimisation plans were generated to evaluate the effectiveness of the optimisation strategies against intrafractional motion. However, no significant correlation between observed plan degradation and tumour motion was identified from our dataset.

Evaluated 3D robustly optimised treatment plans were within the acceptable criteria of this study for all patients except one, where insufficient margins were suspected to have contributed to plan failure. It is worth noting that the observed tumour motions within our dataset were relatively small.

Therefore, further investigation is needed in a patient cohort with more pronounced tumour motions, to assess the efficacy of 3D and 4D robust optimisation in the development of robust treatment plans.

References

[1]   Cancer Research UK, https://www.cancerresearchuk.org/health-professional/cancer-statistics/worldwide-cancer#heading-One, Accessed May 2023.

[2]   Cancer Registry of Norway, *Norwegian Lung Cancer Registry, annual report 2022*, Tech. Rep.   2023.

[3]   Zhao et al, *Radiation dose effect in lung cancer*. J Thorac Dis. 2014;6:336-347

[4]   Yu et al, *Effects of respiratory motion on proton therapy.* J Radia Oncol Biol Phys 2013;576-582

[5]   Mesko et al*, Proton therapy in Non-Small Cell Lung Cancer.* Curr. Treat. Option in Oncol. 2018; 19:27

[6]   Hoffmann et al, *Adaptation is mandatory for intensity modulated proton therapy of advanced lung cancer to ensure target coverage.* Radiother. Oncol. 2017; 122(3):400-405.

[7]   Li et al, *Clinical evaluations of an amplitude-based binning algorithm for 4DCT reconstruction in radiation therapy*, Med. Phys. 2012; 39(2): 922-932

[8]   Zhao et al, *Dosimetric impact of intrafractional motion for compensator based proton therapy of lung cancer.* Phys.Med.Biol. 2008; 53: 3343-3364.

[9]   Kim et al, *Beam angle optimization using angular dependency of range variation assessed via water equivalent path length (WEPL) calculation for head and neck proton therapy.* Physica Media, 2020;69 :19-27

[10] Bourque et al, *A stoichiometric calibration method for dual energy computed tomography.* Phys Med Biol, 2014;21;59(8):2059-88.

[11] Onimaru et al, *Tolerance of organs at risk in small-volume, hypofractionated, image-guided radiotherapy for primary and metastatic lung cancers.* Int J Radiat Oncol Biol Phys, 2003;56(1): 126-135.

[12] McGowan et al, *Treatment planning optimisation in proton therapy.* Brit Inst of Radiology, 2013;86(1021):20120337-3.

[13] Liu et al, *Impact of respiratory motion on worst-case scenario optimised intensity modulated proton therapy for lung cancer.* Pract Radia Oncol, 2015;5(2) 77-86.

[14] Lung Anatomy | Fairview. *https://www.fairview.org/patient-education/82995* (Accessed on 29/05/2023)

[15] Goldsrtaw et al, *The IASLC Lung Cancer Staging Project: Proposals for Revision of the TNM Stage Groupings in the Forthcoming (Eighth) Edition of the TNM Classification for Lung Cancer.* J Thorac Oncol. 2016 Jan;11(1):39-51.

[16] Lung Cancer Staging | LUNGevity Foundation (n.d.). *https://www.lungevity.org/for-patients-caregivers/navigating-your-diagnosis/lung-cancer-staging* (Accessed on 29/05/2023)

[17] Partama et al, *X-ray Microcomputed Tomography (μCT) for Mineral Characterization: A Review of Data Analysis Methods.* Minerals, 2019;9(3)

[18] Mekki et al, *Characterization and performance optimization of radiation monitoring sensors for high energy physics experiments at the CERN LHC and Super-LHC.* CERN Thesis, 2009

[19] Eirik Malinen, *Radiation Dosimetry, Photon Interactions*, University of Oslo, lecture slides, 2021.

[20] Venugopal et al, *de Broglie Wavelength and Frequency of Scattered Electrons in the Compton Effect. March 2013.* Physics Education, 2013;29(1):35

[21] IOP, *Antiparticles and the lepton family.* Episode 519-3 Particle tracks (16-19), Lecture slides.

[22] Okafor et al, *Trends in reinforced composite design for ionizing radiation shielding applications: a review.* J Mater Sci, 2021;56(88):11631-11655

[23] Nguyen et al, *Scattered Radiation Emission Imaging: Principles and Applications.* Int J Biomed Imag. 2011;913893-154

[24] Chen et al, *A Study on Properties of Novel Metallic Foam for Nuclear Applications*. Doctoral thesis, 2015

[25] Bartkoski et al, *Analysis, Prototyping, and Design of an Ionization Profile Monitor for the Spallation Neutron Source Accumulator Ring.* Doctoral thesis, University of Texas MD Anderson cancer center, 2013.

[26] CT Physics.https://web2.uwindsor.ca/courses/physics/high_schools/2006/Medical_Imaging/ ctphysics.html. (Accessed on 29/05/2023)

[27] Baumann et al, *Effects of the Bragg peak degradation due to lung tissue in proton therapy of lung cancer patients*. Radiat Oncol. 2019; 14: 183.

[28] Dawson et al, *Image-guided radiotherapy: rationale, benefits, and limitations.* The Lanc Oncol, 2006;7(10):848-858.

[29] Bouhris et al, *Hyperfractionated or accelerated radiotherapy in head and neck cancer: a meta-analysis.* The Lanc Oncol, 2006;368(9538):843-854.

[30] Gildo et al, *Implementation and utilization of hypofractionation for breast cancer.* Advan Rad Oncol, 2018;3(3):265-270

[31] Hughes et al, *Tumor oxygenation and cancer therapy—then and now,* Br J Radiol. 2019; 92(1093): 20170955.

[32] Zeman et al, *Basics of Radiation Therapy*, Hemat Oncol Palliativ Medic, 2015;13034.

[33] The 2007 Recommendations of the International Commission on Radiological Protection. Annals of the ICRP. ICRP publication 2007;103.37(2–4). 2007.

[34] Paganetti et al *Relative biological effectiveness (RBE) values for proton beam therapy*. Int J Radiat Oncol Biol Phys, 2002;53(2):407-21

[35] Giovannini et al *Variable RBE in proton therapy: comparison of different model predictions and their influence on clinical-like scenarios*. Radia Oncol, 2016;11:68.

[36] Studenski et al, *Proton therapy dosimetry using positron emission tomography. World J Radiol.* 2010; 2(4): 135-142

[37] Baumann et al, *Comparative Effectiveness of Proton vs PhotonTherapy as Part of Concurrent Chemoradiotherapy for Locally Advanced Cancer.* JAMA Oncol.2019;95(1):32-40.

[38] Wang et al *A critical appraisal of the clinical utility of proton therapy in oncology.* Medical Devices: Evidence and Research 2015;8:439

[39] Matsugi et al, *Measurement of Interfraction Variations in Position and Size of Target Volumes in Stereotactic Body Radiotherapy for Lung Cancer.* Int J Radiat Oncol Biol Phys, 2009;75(2): 543-548.

[40] Vyfhuis et al, *Advances in radiotherapy techniques and delivery for non-small cell lung cancer: Benefits of intensity-modulated radiation therapy, proton therapy, and stereotactic body radiation therapy*. Translational Lung Cancer Research 2007;6(2):131-147

[41] Xiaodong et al, *Intensity-modulated proton therapy reduces the dose to normal tissue compared with intensity-modulated radiation therapy or passive scattering proton therapy and enables individualized radical radiotherapy for extensive stage IIIB non-small-cell lung cancer: a virtual clinical study.* Int J Radiat Oncol Biol Phys, 2010;77(2):357-366.

[42] Chuong et al, *Pencil beam scanning versus passively scattered proton therapy for unresectable pancreatic cancer.* Journal of gastrointestinal oncology, 2014;52098486.

[43] Pereira et al, *The role of imaging in radiation therapy planning: past, present, and future.* Biomed Res Int, 2014;231090

[44] Wang et al, *MRI-based Treatment Planning with Electron Density Information Mapped from CT Images.* Technology in Cancer Research and Treatment, ISSN 2008;1533-0346

[45] Stasa et al, *The role of PET-CT in radiotherapy planning of solid tumours.* Radiol Oncol, 2015; 49(1): 1–9

[46] Srinivasan et al, *Applications of linac-mounted kilovoltage Cone-beam Computed Tomography in modern radiation therapy: A review.* Pol J Radiol. 2014;79: 181–193

[47] Orrison et al, Chapter 3 - *Clinical Brain Imaging: Computerized Axial Tomography and Magnetic Resonance Imaging, ,* Functional Brain Imaging, Mosby 1995 , pg. 97-114

[48] Beister et al, *Iterative reconstruction methods in X-ray CT,* European Journal of Medical Physics, 2012;28:94-108

[49] Khan et al, *Advanced ceramic matrix composites for high energy x-ray generation.* Advances in Natural Sciences: Nanoscience and Nanotechnology, 2012;2(4):045015

[50] Podgorsak et al, *Radiation Oncology Physics: A Handbook for Teachers and Students.* Chapter 5: Treatment Machines for External Beam Radiotherapy, IAEA publications, July 2005.

[51] Garnett et al, *A comprehensive review of dual-energy and multi-spectral computed tomography.* Clinical Imaging 2020;67

[52] Real-time Tracking and Motion Management | Varian. (n.d.). Real-time Tracking and Motion Management | Varian. https://www.varian.com/products/radiotherapy/real-time-tracking-and-motion-management (Accessed on 29/05/2023)

[53] Moorees et al, *Four dimensional CT imaging: A review of current technologies and modalities.* Australasian physical & engineering sciences in medicine, 2012;35(1):9-23

[54] Kang et al, *4D Proton Treatment Planning Strategy For Mobile Lung Tumors.* Int J Radiat Oncol Biol Phys, 2006;67(3):906-914

[55] Underberg et al, *Use of maximum intensity projections (MIP) for target volume generation in 4DCT scans for lung cancer.* Int J Radiat Oncol Biol Phys, 2005;63(1):253-60

[56] Wijesooriya et al, *Importance of 4D simulation Planning and delivery.* 2014 AAPM Summer School University of Vermont, June 2014.

[57] Sabri et al, *Multi-detector CT (MDCT) evaluation in interstitial lung disease (ILD): Comparison of MinIP and volumetric high resolution CT (HRCT) images.* The Egyptian Journal of Radiology and Nuclear Medicine 2017;48.1: 87-95

[58] Schneider et al *The Calibration of CT Hounsfield Units for Radiotherapy Treatment Planning*. Phys Med Biol, 1995;41:111-124

[59] Rutherford et al, *Measurement of effective atomic number and electron density using an EMI scanner.* Neuroradiology, 1976;11:15-21

[60]   Bichsel et al, *Passage of charged particles through matter.* Amer Inst Phys Handb 1972;8-142-89

[61]   Gorgisyan et al, *Impact of beam angle choice on pencil beam scanning breath-hold proton therapy for lung lesions*. Acta Oncol, 2017;54(6):853-859

[62]   Jagt et al, *An automated planning strategy for near real-time adaptive proton therapy in prostate cancer.* Phys Med Biol, 2018;63:130517

[63]   Zhou et al, *Robust Angle Selection in Particle Therapy.* Front. Oncol. 2021;11:715025.

[64]   Chang et al, *Clinical implementation of intensity modulated proton therapy for thoracic malignancies.* Int J Radiat Oncol Biol Phys,2014;90(4):809-18

[65]   Magaz et al, *A method for selection of beam angles robust to intra-fractional motion in proton therapy of lung cancer*. Acta Oncol, 2014;53(8):1058-63.

[66]   Yu et al, *Motion-robust intensity-modulated proton therapy for distal esophageal cancer.* Med Phys, 2016;43(3):1111-1118

[67]   ICRU Report 65, *Quantities, Units and Terms in Radioecology. J. ICRU. vol. 1, 2 (2002).* Acta Radiol, 2002;43(6)

[68]   Arimura et al, *Computer-Assisted Target Volume Determination*. Image-Based Computer-Assisted Radiation Therapy, 2017;10(1007):978-981

[69]   Lomax AJ, *Intensity modulated proton therapy and its sensitivity for treatment uncertainties 1: potential effects on calculational uncertainties.* Phys Med Biol 2008;53:1027-1042

[70]   Lomax AJ, *Intensity modulated proton therapy and its sensitivity for treatment uncertainties 2: potential effects on calculational uncertainties.* Phys Med Biol 2008;53:1043-1056

[71]   Hugo et al, *Data from 4D Lung Imaging of NSCLC Patients (Version 2) [Data set].* The Cancer Imaging Archive.

[72]   Hugo et al, *A longitudinal four-dimensional computed tomography and cone beam computed tomography dataset for image-guided radiation therapy research in lung cancer.* Med Phys, 2017;44(2):762-771.

[73]   Kerem et al, (2018),"dicom-contour" , https://github.com/KeremTurgutlu/dicom-contour.git, GitHub Depository.

[74]   Sengbuscha et al, *Maximum proton kinetic energy and patient-generated neutron fluence considerations in proton beam arc delivery radiation therapy*. Med Phys, 2009;36(2):364-372

[75]   Beare et al, *Image Segmentation, Registration and Characterization in R with SimpleITK*. J Stat Softw, 2018;86(8)

[76]   Moller et al, *Heterogeneously Hypo fractionated Radiotherapy of Locally Advanced NSCLC – 2*. Aarhus University Hospital, version 4, HERAN2 Id:87157, June 2022

[77]   Rana et al, *Investigating volumetric repainting to mitigate interplay effect on 4D robustly optimized lung cancer plans in pencil beam scanning proton therapy*. ", J Appl Clin Med Phys, 2020;22(3):107-118

[78]   Kataria et al*, Homogeneity Index: An objective tool for assessment of conformal radiation treatments*. J Med Phys, 2012;37(4): 207–213

[79]   Marzi et al, *Calibration of CT Hounsfield units for proton therapy treatment planning: use of kilovoltage and megavoltage images and comparison of parameterized methods.* Phys Med Biol, 2013;58:4255.

[80]   Constantinou et al, *An electron density calibration phantom for CT-based treatment planning computers*. Med Phys, 1992;19:325–7

[81]   Jiang et al, *Effects of Hounsfield number conversion on CT based proton Monte Carlo dose calculations*. Med Phys, 2007;34:1439–49

[82]   Dolde et al, *4DMRI-based investigation on the interplay effect for pencil beam scanning proton therapy of pancreatic cancer patients.* Rad Oncol, 2019;14(30).

[83]   Clemens et al, *Motion mitigation for lung cancer patients treated with active scanning proton therapy.* Radiation therapy physics, 42;5:2462-2469.

[84]   Engwall et al, *Effectiveness of different rescanning techniques for scanned proton radiotherapy in lung cancer patients.* Phys Med Biol, 2018;63:095006

[85]   Phua et al, *Interplay effect in lung cancer proton therapy.* Journal of Xiangya Medicine, 2018;3

[86]   Grassberge et al, *Motion interplay as a function of patient parameters and spot size in spot scanning proton therapy for lung cancer.* Radiat Oncol Biol Phys, 2013;86(2):380-6

[87]   Matney et al, *Effects of Respiratory Motion on Passively Scattered Proton Therapy Versus Intensity Modulated Photon Therapy for Stage III Lung Cancer: Are Proton Plans More Sensitive to Breathing Motion?* Radiat Oncol Biol Phys, 2013;3(1):576-582.

[88]   Ruysscher et al, *Tumour Movement in Proton Therapy: Solutions and Remaining Questions: A Review. 2015;* Radiat Oncol Biol Phys, 7(3): 1143–1153.

[89]   Van Herk et al, *The probability to correct target dosage: Dos-population histograms for deriving treatment margins in radiotherapy.* Radiat Oncol Biol Phys, 2000;47:1121-1135

[90]   Engelman et al, *The effect of breathing and set-up errors on the cumulative dose to a lung tumour*. Radio Oncol, 2001;60:95-105.

[91]   Wanet et al, *The effect of breathing and set-up errors on the cumulative dose to a lung tumour*. Radio Oncol, 2014;110:529-537

[92]   Han et al, *Current status of proton therapy techniques for lung cancer*. Radiat Oncol J. 2019;37(4): 232–248

[93]   Wong et al, *The use of active breathing control (ABC) to reduce margin for breathing motion.* Int J Radiat Oncol Biol Phys, 1999;44:911–9.

[94]   Kaza et al, *Lung volume reproducibility under ABC control and self-sustained breath-holding.* J Appl Clin Med Phys. 2017;18:154–62

[95]   Matsuura et al, *Integration of a real-time tumor monitoring system into gated proton spot scanning beam therapy: an initial phantom study using patient tumor trajectory data.* Med Phys. 2013;40:071729

[96]   Huang et al, *. Respiratory motion reduction in PET/CT using abdominal compression for lung cancer patients.* PLoS One. 2014;9:e98033.

[97]   Bouilhol et al, *Is abdominal compression useful in lung stereotactic body radiation therapy? : a 4DCT and dosimetric lobe-dependent study.* Phys Med. 2013;29:333–40
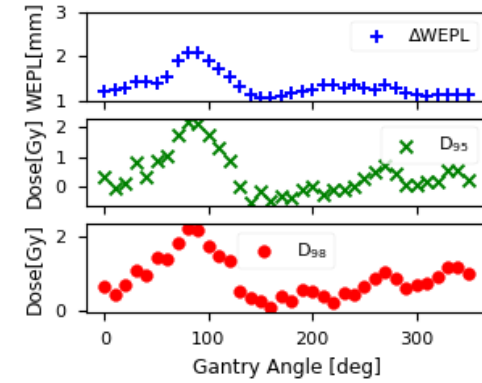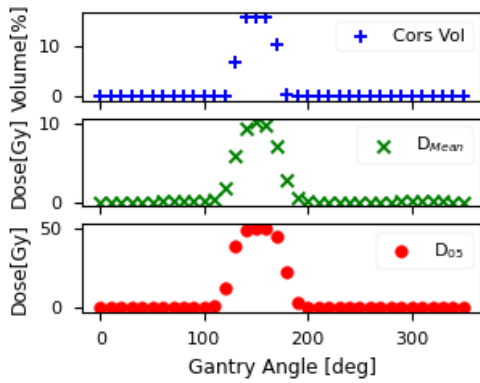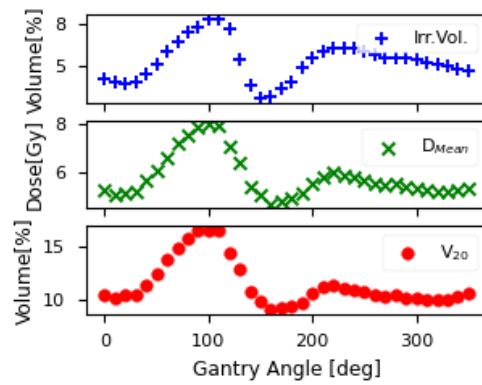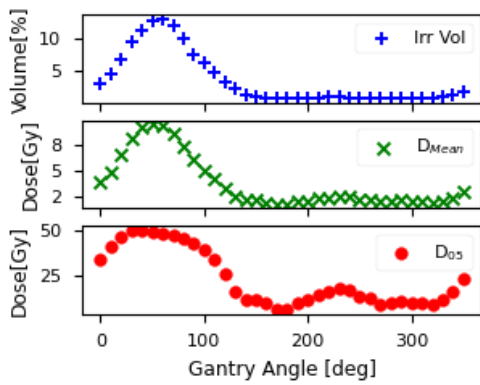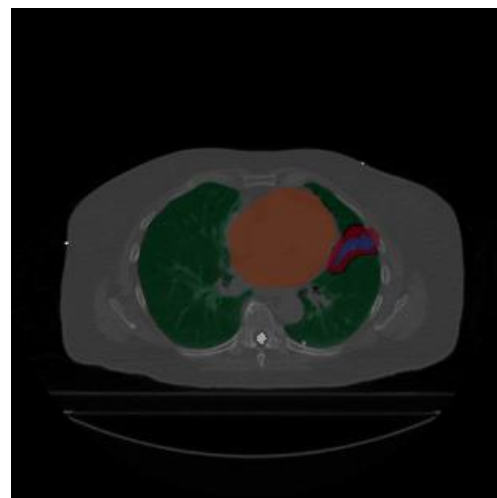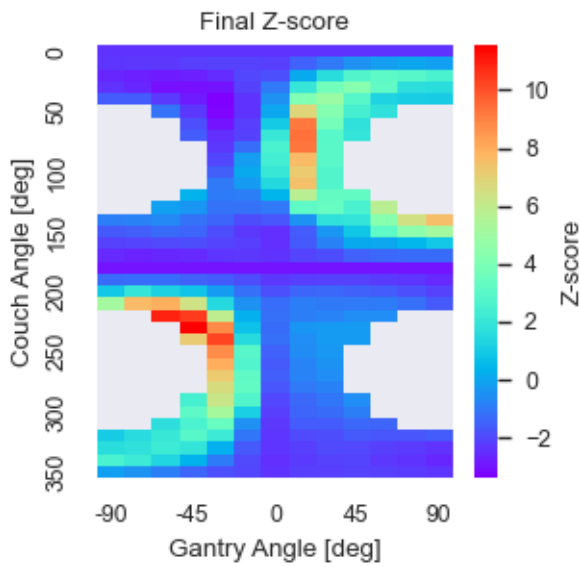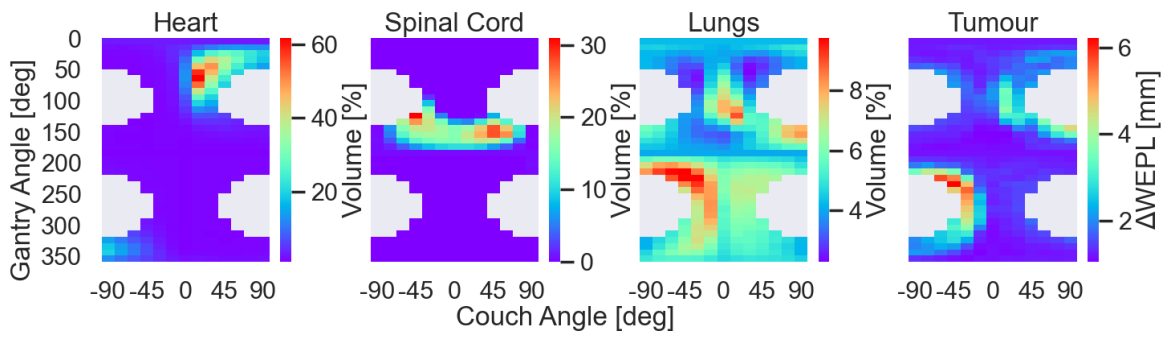
Appendix A

Figures in appendix A depict patient specific graphs for all the patients utilised in the study. On top, the ΔWEPL and OAR irradiation maps of the patient are presented. Next, on the left the final Z-score that was utilised to identify the robust beam geometries is depicted. On the right, the AIP CT scan of the patient can be identified, where the iGTV is delineated in blue, the iCTV in red, the heart in orange, lungs in green and the spinal cord in white. Finally, the correlation graphs between the ΔWEPL and OAR percentage irradiation with iCTV dose reduction and OAR accumulated dose were presented. Top with portrays the heart percentage irradiation with heart D5 and Dmean. Top left depicts the lungs percentage irradiation with lungs Dmean and V20. Bottom right portrays cord percentage irradiation, with cord D5 and cord Dmean. Finally, bottom left depicts ΔWEPL and iCTV ΔD95 and ΔD98. Graphs of all 11 patients utilised are presented.
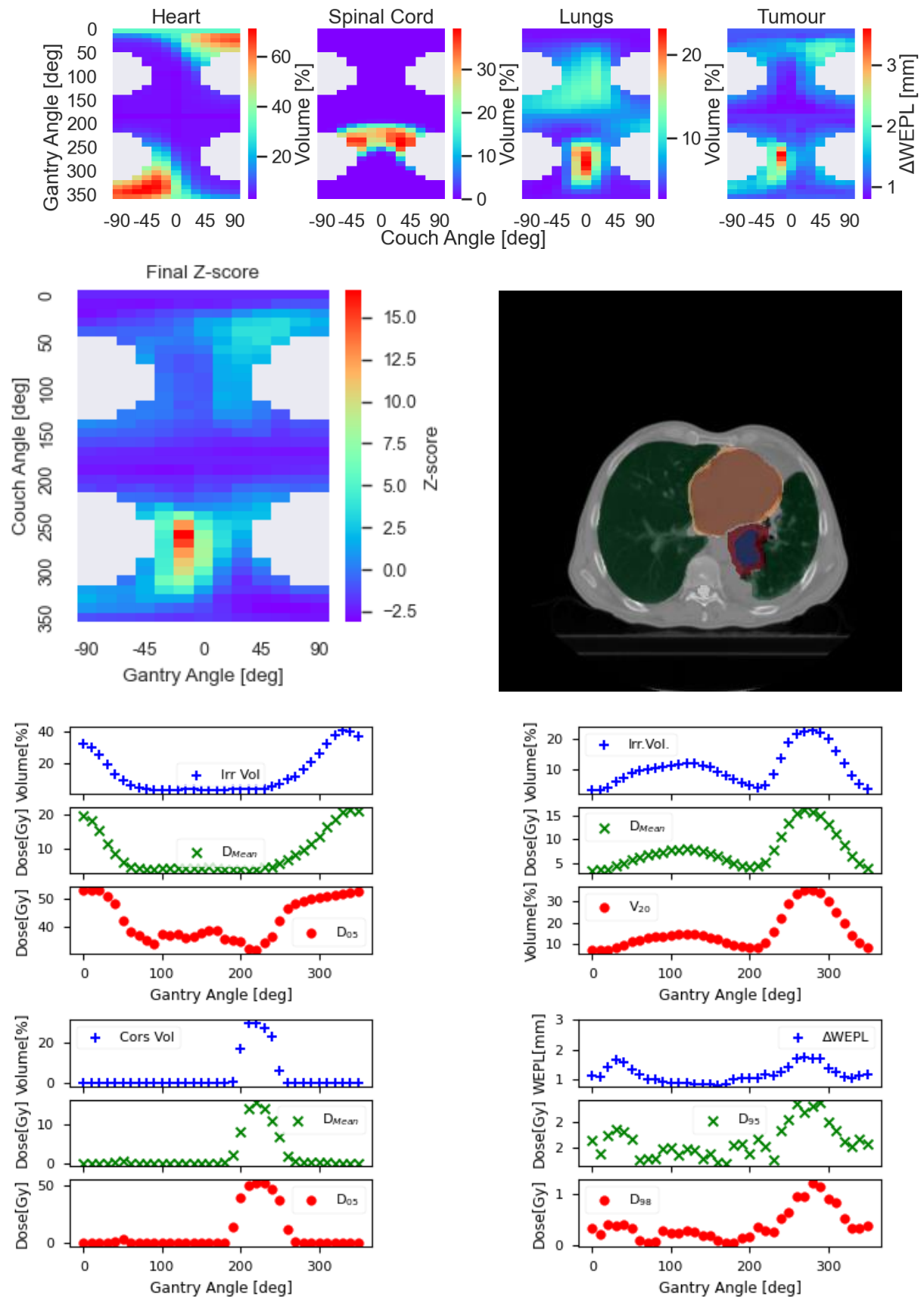
Patient 100
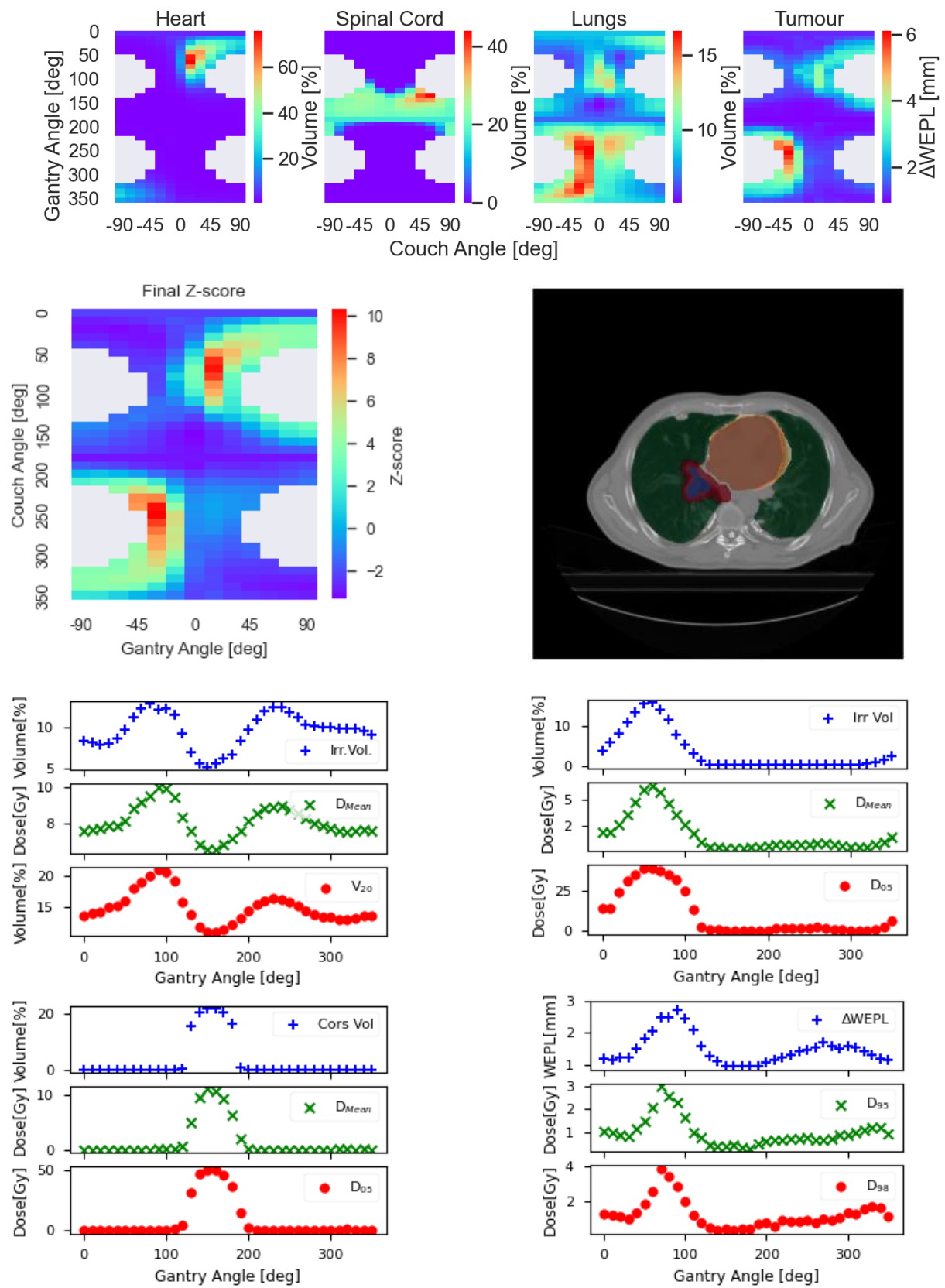
Patient 101

Patient 102
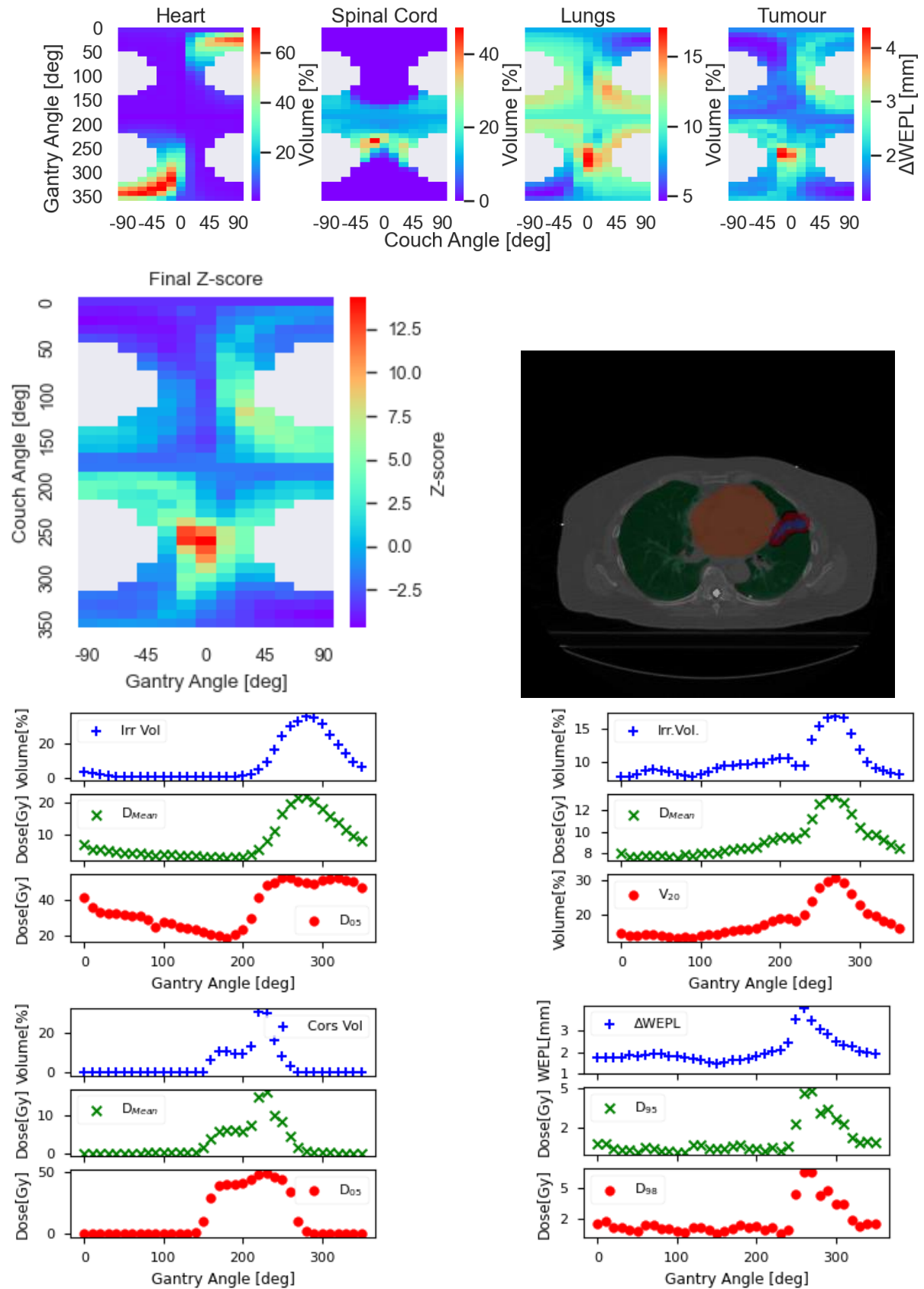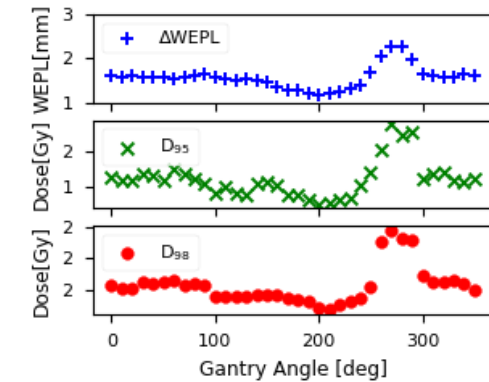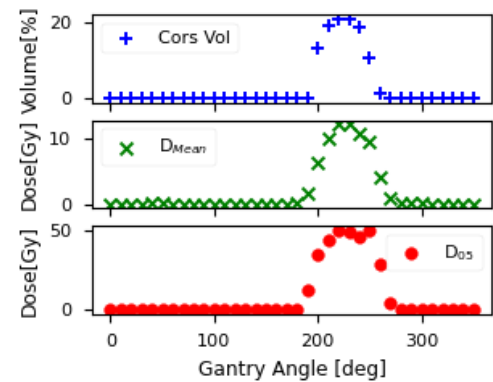
Patient 104

Patient 105
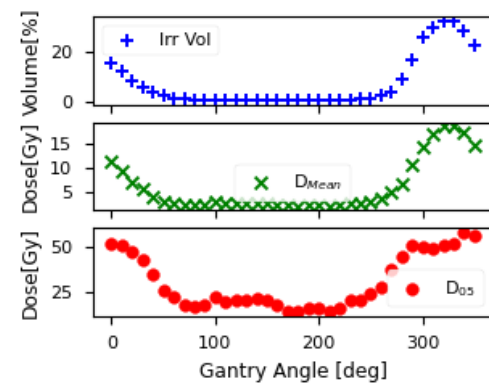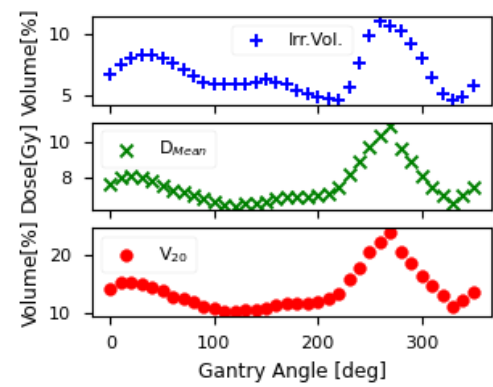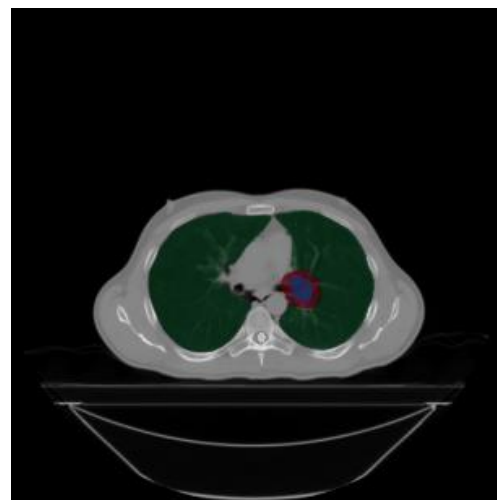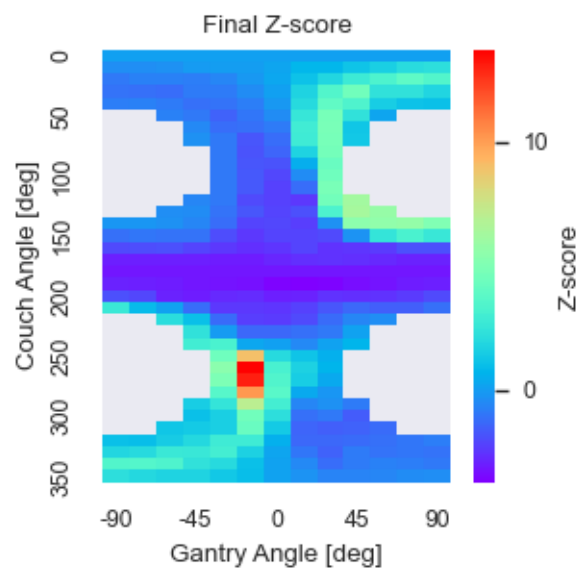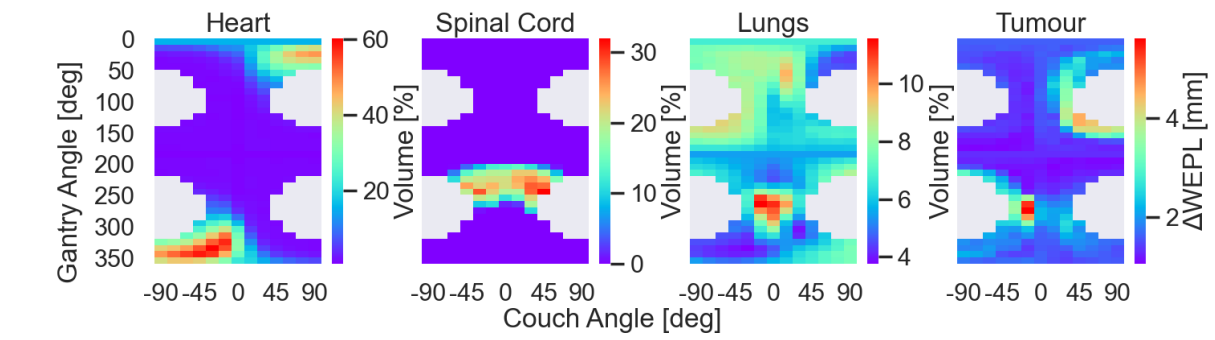
Patient 106
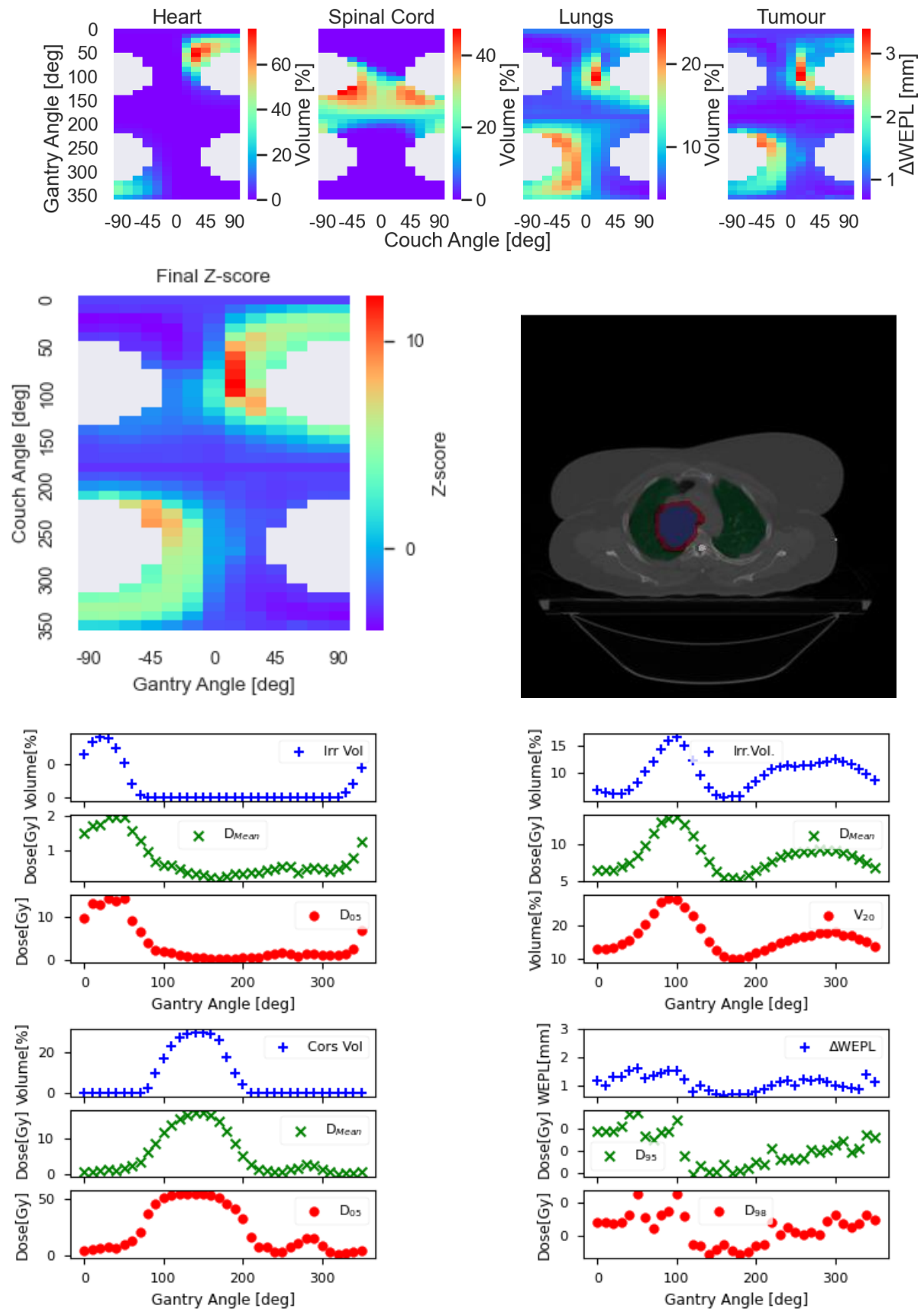
Patient 107
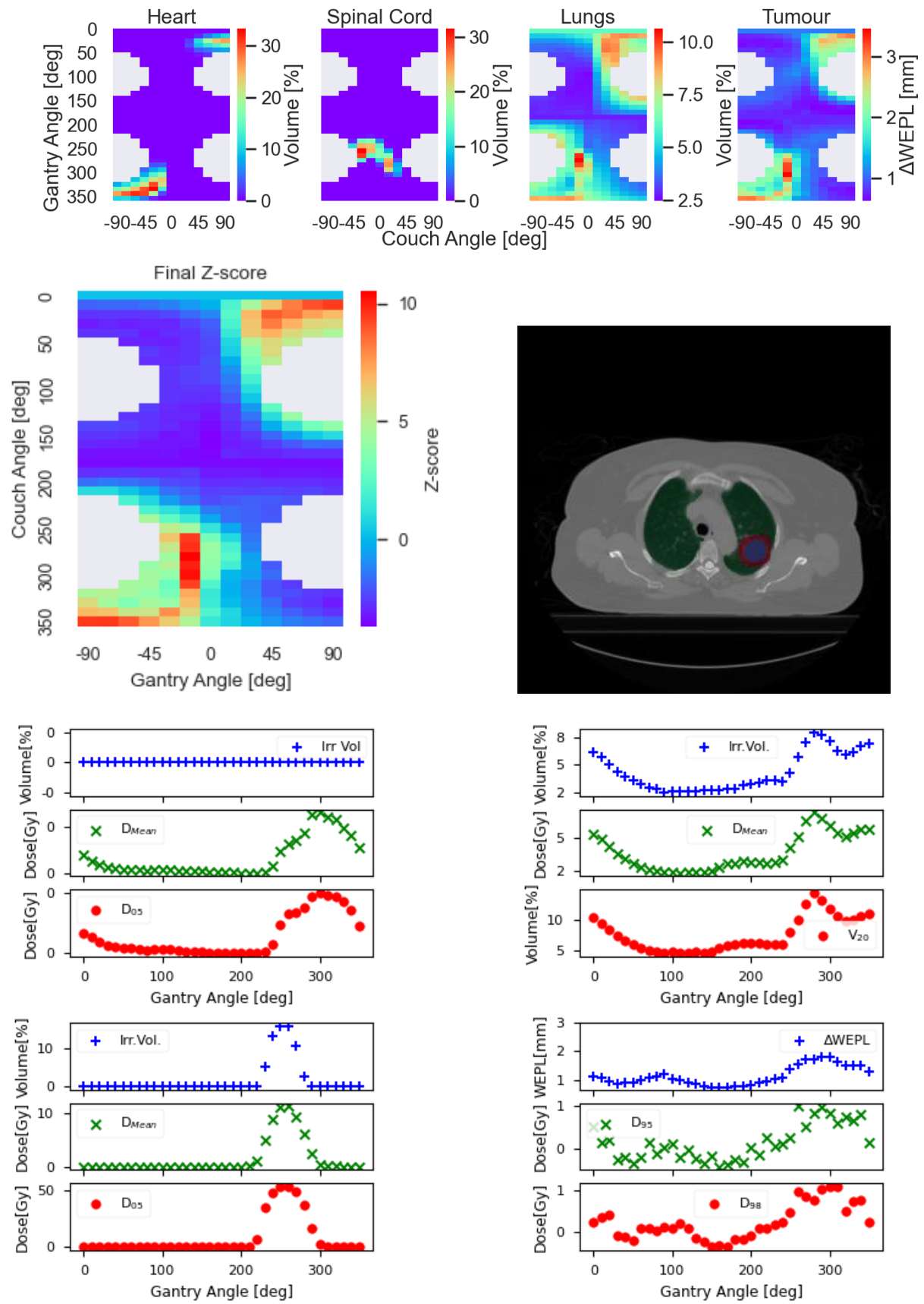
Patient 108
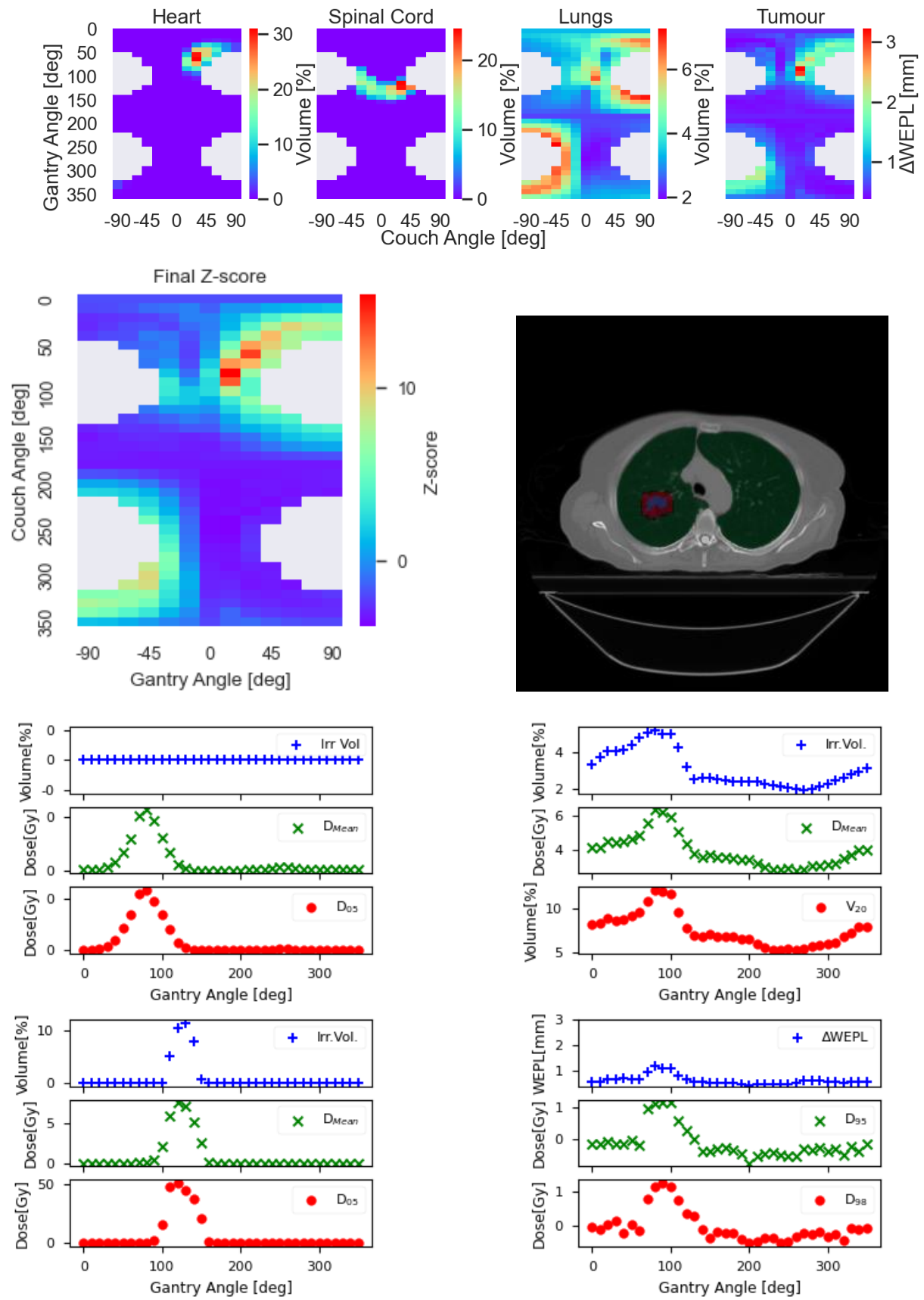
Patient 110
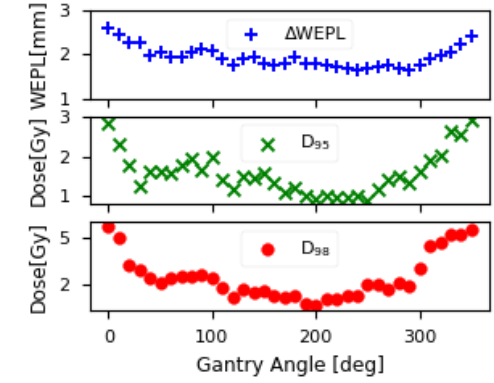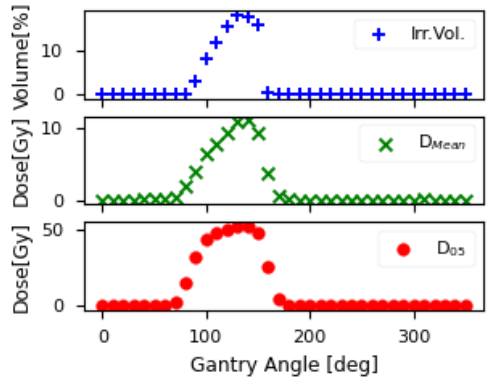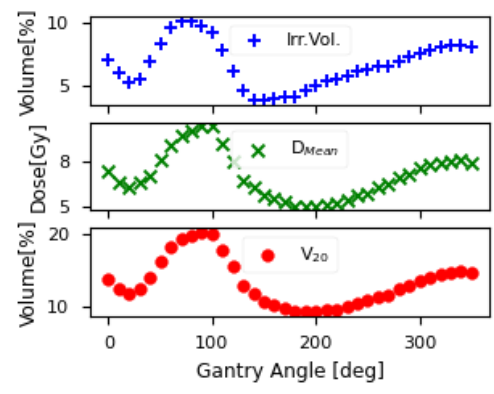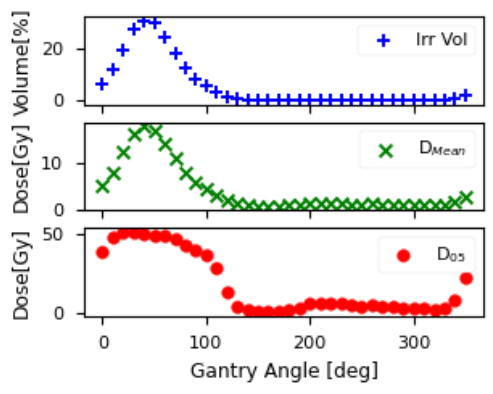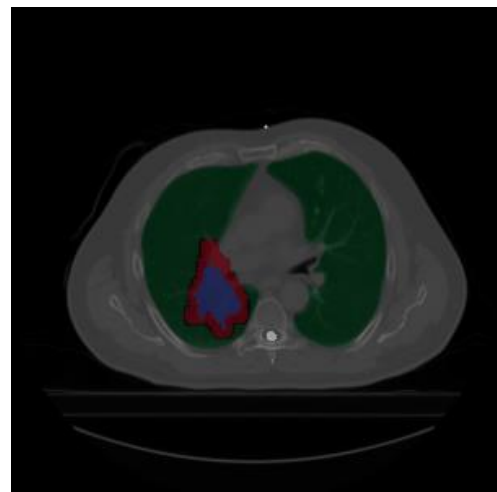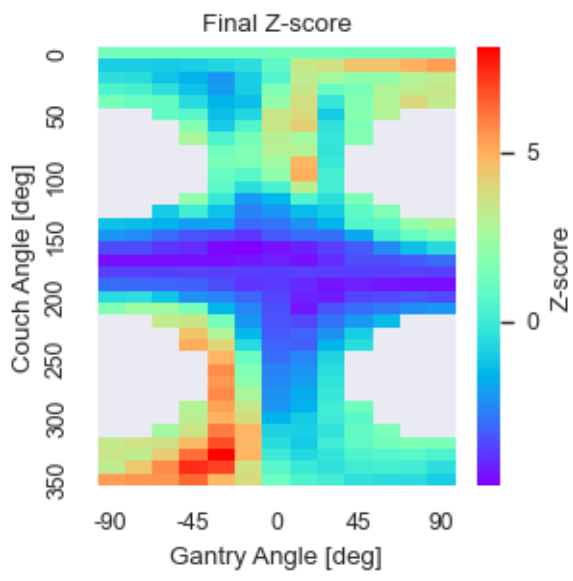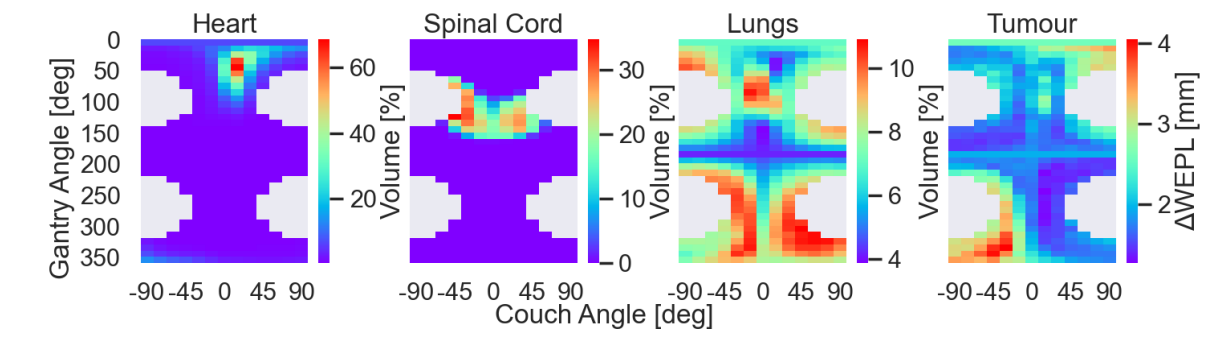
Patient 111
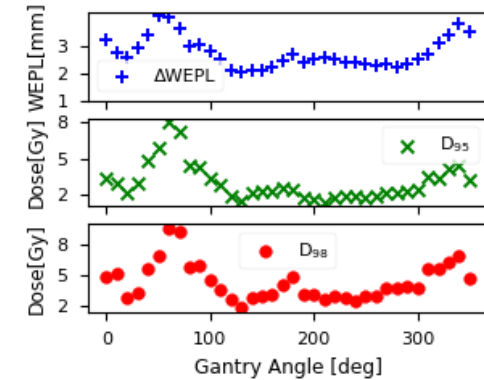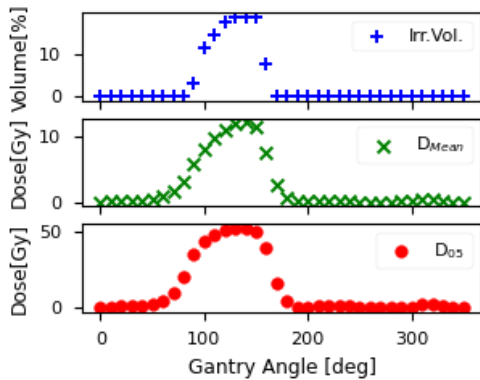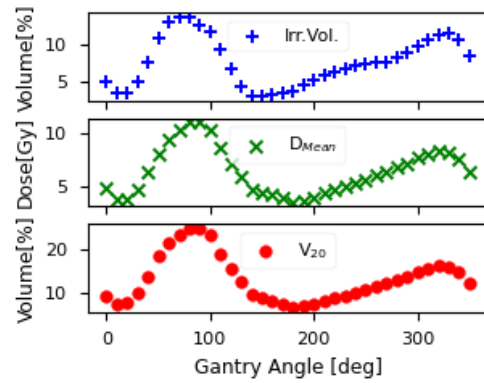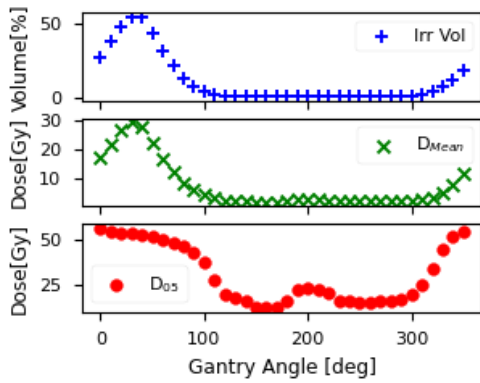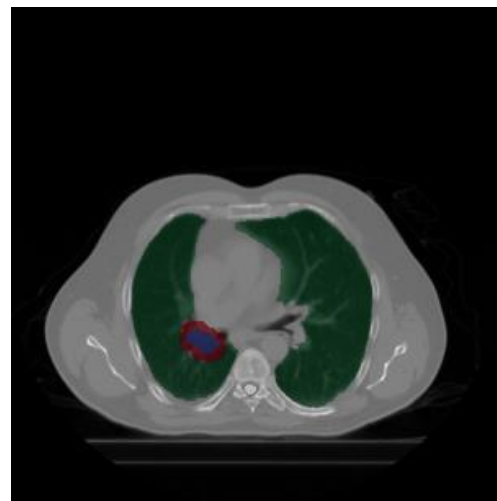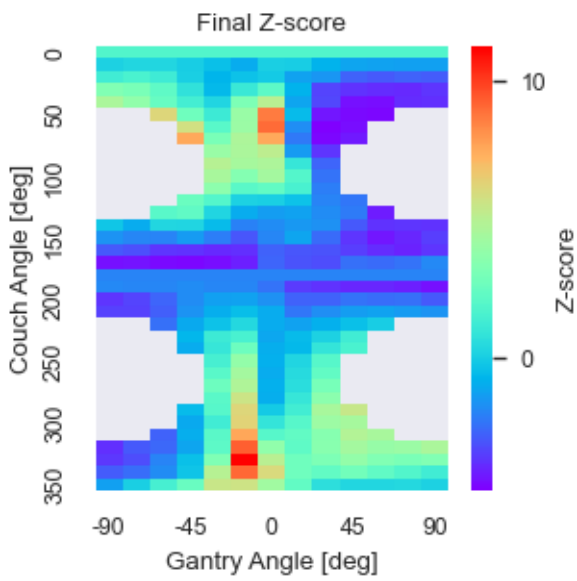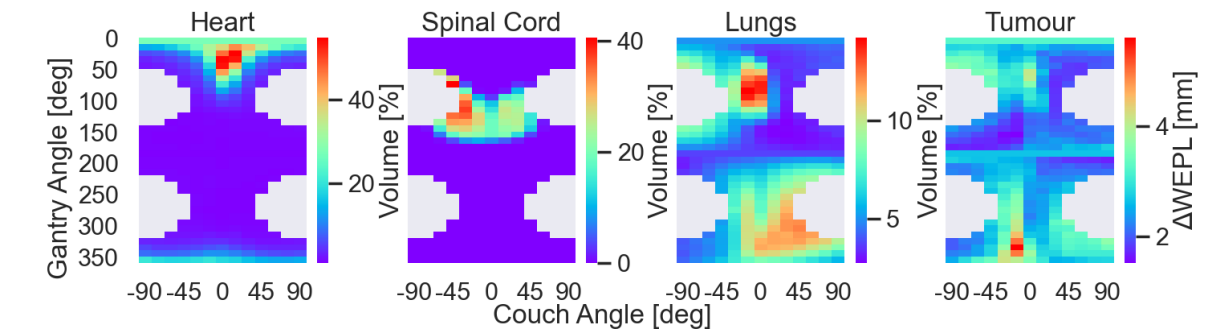
Patient 114
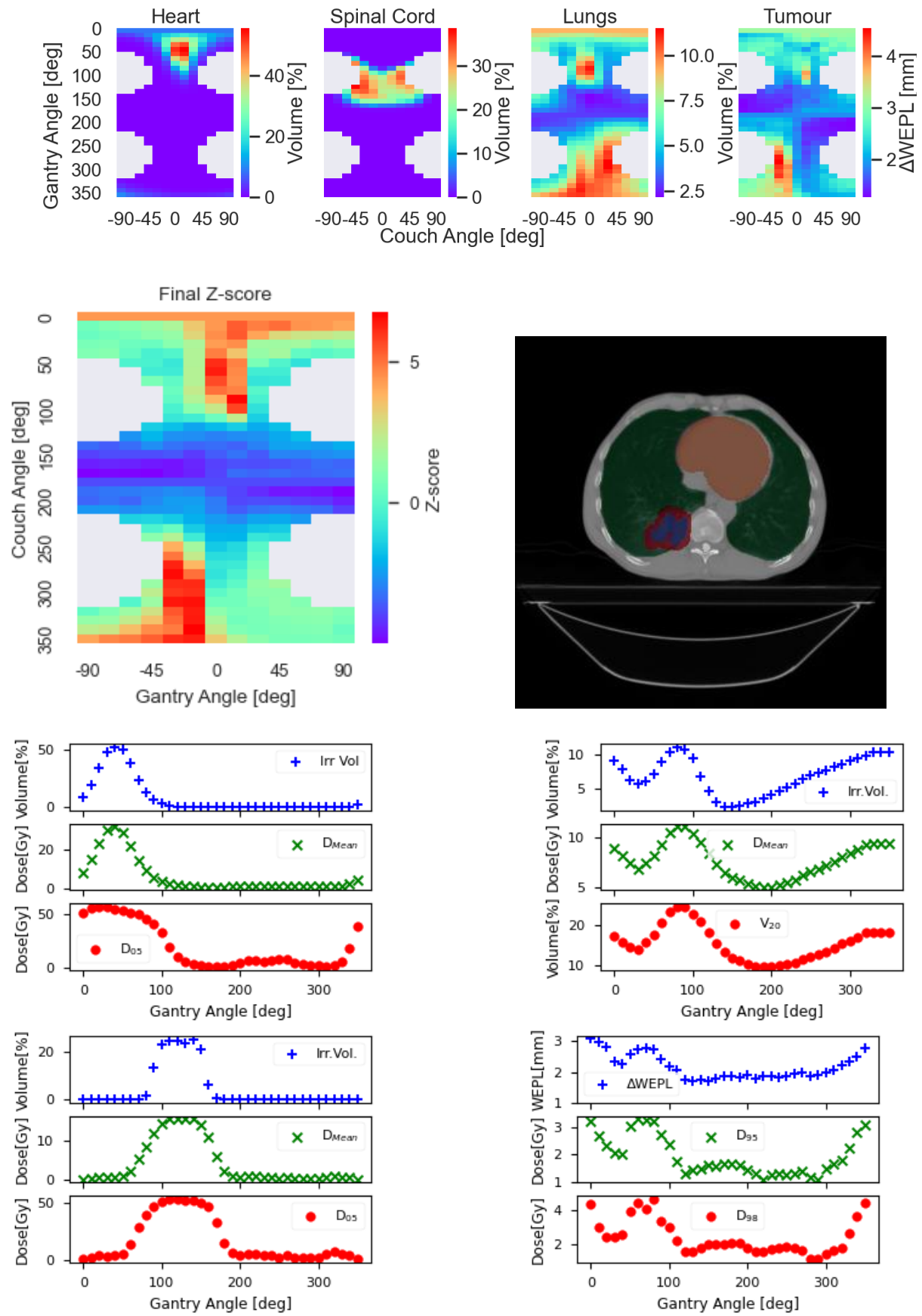
Appendix B - Python Codes

B.1 DICOM to Array

The python code utilised for the conversion of the images and structures delineation to arrays is presented. The python code of Kerem et al was utilised and it can be identified in the GitHub Depository.

```python
1.  """
2.  Funtion to convert delineation and images to arrays inputted after the GitHub code
3.  """
4.  def load_dicom_file(image_path, rt_path,delinition):
5.      """
6.      Parameters
7.      ----------
8.      image_path :
9.      rt_path :
10.     Returns
11.     -------
12.     tumor :
13.     ct_scan :
14.     """
15.     contour_filename = str(list(Path(rt_path).iterdir())[0])
16.     #print(contour_filename)
17.     # read dataset for contour
18.     rt_sequence = dicom.read_file(contour_filename)
19.     ## extract roi index in RT Struct
20.     print(get_roi_names(rt_sequence))
21.     ## Find the index of the structure that is going to be extracted. You need to know the
name of the contour but is also printed above
22.     index = np.where(np.array(get_roi_names(rt_sequence)) == delinition)[0][0]
23.     print(index)
24.     contour_datasets = get_roi_contour_ds(rt_sequence, index)
25.     # construct mask dictionary that fill contours
26.     mask_dict = get_mask_dict(contour_datasets, image_path)
27.     # get slice orders
28.     slice_orders = slice_order(image_path)
29.     #### get image and mask data for patient####
30.     img_voxel, mask_voxel = get_data(image_path, contour_filename, roi_index=index)
31.     #Stack all tumor slices together.
32.     contour = np.stack(mask_voxel, axis=0)
33.     ct_scan = np.stack(img_voxel, axis=0)
34.
35.     return contour , ct_scan
36.
37.
38. # Example of CT path
39. image_path = 'C:/Users/kyria/Desktop/Thesis Data/Patients CT/104/4D-Lung/104_HM10395/09-29-
1998-NA-p4-84934/1.000000-P4P104S300I00012 Gated 90.0A-47114'
40. rt_path = 'C:/Users/kyria/Desktop/Thesis Data/Patients CT/104/4D-Lung/104_HM10395/09-29-
1998-NA-p4-84934/1.000000-P4P104S300I00012 Gated 90.0A-74.10'
41.
42. """
43. Run the Funtion
44. The orientation of the output array will be in the order of [SI,AP,RL].
45. """
46. #Run Funtion for all deliniations
47. tumor, ct_scan= load_dicom_file(image_path, rt_path,"Tumor_c90")
48. RLung, ct_scan = load_dicom_file(image_path, rt_path,"RLung_c90")
49. LLung, ct_scan = load_dicom_file(image_path, rt_path,"LLung_c90")
50. heart, ct_scan= load_dicom_file(image_path, rt_path,"Heart_c90")
51. cord, ct_scan= load_dicom_file(image_path, rt_path,"Cord_c90")
52. #Save data
53. np.save('Tumor_90.npy',tumor)
54. np.save('ct_scan90.npy', ct_scan)
```

```
55. np.save('RLung_00.npy',RLung)
56. np.save('LLung_00.npy',LLung)
57. np.save('heart90.npy', heart)
58. np.save('cord90.npy', cord)
```

B.2 Pre-processing Algorithm

```python
1. import os
2. import numpy as np
3. import matplotlib.pyplot as plt
4. import pickle
5. from scipy import ndimage
6. ct_list = []
7. tumor_list = []
8. heart_list = []
9. cord_list = []
10. RLung_list = []
11. LLung_list = []
12. esophagus_list = []
13. trachea_list =[]
14. voxel_size=(3.0,1.0527,1.0527)
15.
16. """
17. Load CT arrays
18. """
19. # giving directory name
20. dirname = 'CT_p104'
21. # giving file extension
22. ext = '.npy'
23. for files in os.listdir(dirname):
24.     if files.endswith(ext):
25.         print(files)  # printing file name of desired extension
26.         filepath = dirname + '/' + files
27.         # Load the STL files and add the vectors to the plot
28.         ct = np.load(filepath)
29.         ct_list.append(ct)
30. """
31. Load Tumor arrays
32. """
33. # giving directory name
34. dirname = 'tumor_p104'
35. # giving file extension
36. ext = '.npy'
37. for files in os.listdir(dirname):
38.     if files.endswith(ext):
39.         print(files)  # printing file name of desired extension
40.         filepath = dirname + '/' + files
41.         # Load the STL files and add the vectors to the plot
42.         tum = np.load(filepath)
43.         tumor_list.append(tum)
44. """
45. Load Organs At Risk
46. """
47. #Heart
48. # giving directory name
49. dirname = 'heart_p104'
50. # giving file extension
51. ext = '.npy'
52. for files in os.listdir(dirname):
53.     if files.endswith(ext):
54.         print(files)  # printing file name of desired extension
55.         filepath = dirname + '/' + files
56.         # Load the STL files and add the vectors to the plot
57.         hea = np.load(filepath)
58.         heart_list.append(hea)
```

```python
59. ## Cord
60. # giving directory name
61. dirname = 'cord_p104'
62. # giving file extension
63. ext = '.npy'
64. for files in os.listdir(dirname):
65.     if files.endswith(ext):
66.         print(files)  # printing file name of desired extension
67.         filepath = dirname + '/' + files
68.         # Load the STL files and add the vectors to the plot
69.         cor = np.load(filepath)
70.         cord_list.append(cor)
71.
72. cord_floats = []
73. for cord in cord_list:
74.     cord_floats.append(cord.astype(float))
75. ##RLung
76. # giving directory name
77. dirname = 'rlung_p104'
78. # giving file extension
79. ext = '.npy'
80. for files in os.listdir(dirname):
81.     if files.endswith(ext):
82.         print(files)  # printing file name of desired extension
83.         filepath = dirname + '/' + files
84.         # Load the STL files and add the vectors to the plot
85.         rl = np.load(filepath)
86.         RLung_list.append(rl)
87. ##LLung
88. # giving directory name
89. dirname = 'llung_p104'
90. # giving file extension
91. ext = '.npy'
92. for files in os.listdir(dirname):
93.     if files.endswith(ext):
94.         print(files)  # printing file name of desired extension
95.         filepath = dirname + '/' + files
96.         # Load the STL files and add the vectors to the plot
97.         ll = np.load(filepath)
98.         LLung_list.append(ll)
99.
100.
101. def generate_oar_maps(oar_list):
102.     print('Generate OAR map')
103.     oar = np.sum(oar_list, axis = 0)
104.     return oar
105.
106. def generate_ct_maps(ct_array):
107.     """
108.     Parameters
109.     ----------
110.     ct_array : A list of Arrays containign CT in numpy array format
111.     Returns
112.     -------
113.     average_ct : The average attenuation of each voxel is displayed.
114.     MIP_ct : The voxel with the highest attenuation is displayed.
115.     MinIP_ct : The voxel with the lowest attenuation is displayed.
116.     """
117.     # calculate the average CT
118.     average_ct = np.mean(ct_array, axis=0)
119.     # calculate MIP CT
120.     MIP_ct = np.amax(ct_array, axis=0)
121.     #Calculate MinIP CT
122.     MinIP_ct = np.amin(ct_array, axis=0)
123.     return average_ct, MIP_ct ,MinIP_ct
124.
125. def generate_tumor_maps(tumor_array):
126.     """
127.     Parameters
128.     ----------
```

```python
129.        tumor_array : A list of Arrays containign tumor coordinates in numpy array format
130.        Returns
131.        -------
132.        Prob_map : Voxel value represents the probability of tumor location within the
timescale of the input arrays
133.        itv : Geometric summation of all tumor coordinates
134.        """
135.        # calculate the probability map
136.        tumors_lists = []
137.        for tumor in tumor_array:
138.            tumor[tumor > 0.1] = 1
139.            tumors_lists.append(tumor)
140.
141.        itv = np.sum(tumors_lists, axis=0)
142.        #generate the PM
143.        Prob_map = np.copy(itv)/10
144.        # generate the ITV
145.        itv[itv>=1]=1
146.        return Prob_map, itv
147.
148. def generate_ctv(tumor_list, voxel_size, expansion_magnitude):
149.        print('generate ctv')
150.        ctv_list =[]
151.        i= 0
152.        for tumor in tumor_list:
153.            i = i +1
154.            print(i)
155.            # Calculate the dilation radius for the x-y plane only
156.            dilation_radius = tuple(expansion_magnitude / np.array(voxel_size))
157.            new_array = np.zeros_like(tumor)
158.            ctv = np.zeros_like(tumor)
159.            # Find the tumor indices
160.            tumor_indices = np.argwhere(tumor)
161.            # Get the min and max indices for the tumor in the z-axis
162.            z_min = np.min(tumor_indices[:, 0])
163.            z_max = np.max(tumor_indices[:, 0])
164.
165.            # Iterate over the z-axis where there is tumor
166.            for z in range(z_min, z_max+1):
167.                # Get the x-y slice of the tumor for this z-index
168.                tumor_slice = tumor[z,:,:]
169.
170.                # Expand the tumor in the x-y plane using binary dilation
171.                dilated_array = ndimage.binary_dilation(tumor_slice,
structure=np.ones(shape=(3,3),dtype=float),iterations=int(np.floor(np.max(dilation_radius[1]))))
172.
173.                # Update the tumor array with the dilated array for this z-index
174.                new_array[z,:,:] = dilated_array
175.
176.            dilated_array_z = ndimage.binary_dilation(new_array, structure=
np.ones(shape=(3,1,1),dtype=float), iterations=int(np.floor(dilation_radius[0])))
177.            ctv[:,:,:] =  dilated_array_z
178.            ctv_list.append(ctv)
179.        ictv = np.sum(ctv_list, axis=0)
180.        ictv_pm = np.copy(ictv)/10
181.        ictv[ictv>=1]=1
182.
183.        return ctv_list, ictv,ictv_pm
184.
185. def transform_evaluate_to_rsp(arrays):
186.        new_arrays = []
187.        for array in arrays:
188.            new_array = array.copy()
189.            print("RSP_eval:")
190.            new_array[array > 80] = new_array[array > 80]*0.0005366+ 1.08604241
191.            new_array[(array > 20) & (array <= 40)] = new_array[(array > 20) & (array <=
40)]*0.00148779 + 1.000424545
192.            new_array[array <= 20] = new_array[array <= 20]*1.01372549 + 1.01372549
193.            new_arrays.append(new_array)
194.        return new_arrays
```

```
195.
196. def transform_refernce_to_rsp(array):
197.     new_array = array.copy()
198.     print("RSP_ref:")
199.     new_array[array > 80] = new_array[array > 80]*0.0005366+ 1.08604241
200.     new_array[(array > 20) & (array <= 40)] = new_array[(array > 20) & (array <= 40)]*0.00148779 + 1.000424545
201.     new_array[array <= 20] = new_array[array <= 20]*1.01372549 + 1.01372549
202.     return new_array
203.
204. """
205. ### Call the funations
206. """
207. ave_ct, mip_ct , min_ip_ct = generate_ct_maps(ct_list)
208. prob_map, itv = generate_tumor_maps(tumor_list)
209. ct_eval_rsp = transform_evaluate_to_rsp(ct_list)
210. ct_ave_rsp = transform_refernce_to_rsp(ave_ct)
211. ct_mip_rsp = transform_refernce_to_rsp(mip_ct)
212. heart = generate_oar_maps(heart_list)
213. cord = generate_oar_maps(cord_floats)
214. rlung = generate_oar_maps(RLung_list)
215. llung = generate_oar_maps(LLung_list)
216. ctv_list , ictv, ictv_pm = generate_ctv(tumor_list, voxel_size, 5)
217. lungs = np.add(rlung,llung)
218. lungs= np.where(lungs >0.1,1,lungs)
219. lungs = np.where(ictv>0.1,0,lungs)
220. heart = np.where(ictv>0.1,0,heart)
221.
```

B.3 Tumour Motion Algorithm

```
 1. import SimpleITK as sitk
 2. import numpy as np
 3. import os
 4. import matplotlib.pyplot as plt
 5. import matplotlib.ticker as ticker
 6. from scipy.spatial import distance
 7. import statistics
 8. import itertools
 9. from collections import Counter
10. """
11. Load Tumor arrays
12. """
13. tumor_list = []
14. # giving directory name
15. dirname = 'tumor_p104'
16. # giving file extension
17. ext = '.npy'
18. for files in os.listdir(dirname):
19.     if files.endswith(ext):
20.         print(files)  # printing file name of desired extension
21.         filepath = dirname + '/' + files
22.         # Load the STL files and add the vectors to the plot
23.         tum = np.load(filepath)
24.         tumor_list.append(tum)
25. prob_map = np.load('prob_map.npy')
26. print('prob_map.npy')
27. itv = np.load('itv.npy')
28. print('itv.npy')
29. ictv = np.load('ictv.npy')
30. print('ictv.npy')
31. """
32. Patient Specific CT Information all in mm
33. """
34. voxel_dimenstions = [3.0,1.0527,1.0527]
35. voxel_volume = np.prod(voxel_dimenstions)
36. """
37. Functions for Tumor Motion
```

```python
38.     """
39.     def center_of_mass_displacement(tumor_list, voxel_dimenstions):
40.         """
41.         Parameters
42.         ----------
43.         tumor_list : List containing tumor coordinates in numpy arrays
44.         voxel_size : Dimensions of voxel in mm [SI,AP,RL]
45.         Returns
46.         -------
47.         max_displacement : Tumor maximum displacement over the breathing cycle in mm calculate
from com displacement
48.         com_list         : List of all CoM coordinates
49.         average_com      : The average CoM coordinate
50.         """
51.         com_list = []
52.         displacement_list = []
53.         print('Calculating COM Displacement')
54.         def center_of_mass(arr):
55.             indices = np.where(arr == 1)
56.             RL_cm = np.mean(indices[2])
57.             AP_cm = np.mean(indices[1])
58.             SP_cm = np.mean(indices[0])
59.             return (SP_cm, AP_cm, RL_cm)
60.
61.         for tumor_array in tumor_list:
62.             com = center_of_mass(tumor_array)
63.             com_list.append(com)
64.
65.         average_com = np.mean(com_list, axis=0)
66.         print("Average center of mass:", average_com)
67.         itv_com = center_of_mass(itv)
68.         ictv_com = center_of_mass(ictv)
69.         print("itv center of mass:", average_com)
70.         print("iCTV center of mass:", average_com)
71.         fig = plt.figure('Centre of Mass')
72.         ax = fig.add_subplot(111, projection='3d')
73.         plt.title('Patient 104')
74.         for i, com in enumerate(com_list):
75.             ax.scatter(*com, cmap='tab10', alpha=1, label=str(i))
76.         x, y, z = zip(*com_list)
77.         ax.plot(x, y, z, ':k')
78.         ax.legend(loc = 'best')
79.         ax.set_xlabel("SI", labelpad =25)
80.         ax.set_ylabel("AP" ,labelpad =25 )
81.         ax.set_zlabel("RL", labelpad =25)
82.         plt.locator_params(axis='both', nbins=5)
83.         plt.show()
84.             # Calculate all pairwise distances between CoM points
85.         for pair in itertools.combinations(com_list, 2):
86.             point1 = [a * b for a, b in zip(pair[0], voxel_dimenstions)]
87.             point2 = [a * b for a, b in zip(pair[1], voxel_dimenstions)]
88.             displacement = distance.euclidean(point1, point2)
89.             displacement_list.append(displacement)
90.         max_displacement = max(displacement_list)
91.         print("Maximum displacement:", max_displacement)
92.         return max_displacement, com_list, average_com, itv_com,ictv_com
93. print(np.max(prob_map))
94.
95. def prob_hist(prob_map):
96.     """
97.     Parameters
98.     ----------
99.     prob_map : Array describing the Probability Map
100.    Returns
101.    -------
102.    prob_hist : frequency percentage of voxel probability
103.    """
104.    print('Generating Probability Histogram')
105.    prob_hist = prob_map[np.nonzero(prob_map)]
106.    mean_hist = np.mean(prob_hist)
```

```python
107.        sigma_hist = statistics.stdev(prob_hist,mean_hist)
108.        print('The average pixel probability is',mean_hist)
109.        print ('Sigma of the prob distribution is', sigma_hist)
110.        # Create a dictionary that contains the frequency of each value in the prob_hist array
111.        # Create a list of tuples with the value and its frequency
112.        value_freq = Counter(prob_hist)
113.        # Extract the values and frequencies from the Counter object
114.        fig, ax = plt.subplots(figsize=(4,5))
115.        #plt.title('Probability Map Frequency')
116.        values = [val for val in value_freq.keys()]
117.        freq = [value_freq[val] for val in values]
118.        freq = [value_freq[val]/len(prob_hist)*100 for val in values]
119.        ax.bar(values, freq, width=0.08, align='center')
120.        plt.xticks(np.linspace(0,1,11))
121.        ax.yaxis.set_major_formatter(ticker.PercentFormatter())
122.        #plt.gca().set_yticklabels(['{:,%}'.format(x) for x in freq])
123.        plt.title('Patient 104')
124.        plt.xlabel('Voxel Probability Value')
125.        plt.ylabel('Frequency')
126.        plt.grid(axis ='y')
127.        plt.show()
128.
129. def plot_tumor_volume(tumor_list, voxel_volume):
130.        """
131.        Parameters
132.        ----------
133.        tumor_list : List containing tumor coordinates in numpy arrays
134.        voxel_volume : Volume of each voxel in mm^3 (use converion *0.001 to convert to cc)
135.        Returns
136.        -------
137.        tumor_volume : List of tumor volumes
138.        """
139.        #print('Ploting  tumor volumes')
140.        tumor_volumes = []
141.        for i, tumor in enumerate(tumor_list):
142.            non_zero_voxels = np.count_nonzero(tumor)
143.            tumor_volume = non_zero_voxels * voxel_volume
144.            tumor_volumes.append(tumor_volume)
145.        mean_vol = np.mean(tumor_volumes)
146.        volume_var = 100*(np.max(tumor_volumes) - np.min(tumor_volumes))/mean_vol
147.        print('mean tumor volume is',mean_vol)
148.        print('perc volume variation is', volume_var)
149.        #plt.figure('Tumor Volume')
150.        plt.figure (figsize=(5,3))
151.        plt.title('Patient 104')
152.        phases = np.arange(0, 91, 10) # generate an array with phase values
153.        plt.bar(phases, tumor_volumes, width = 8, align = 'center', linewidth=4)
154.        plt.xlabel('Phase')
155.        plt.ylabel('Tumor Volume [cc]')
156.        plt.ylim(30,60)
157.        plt.xticks(np.linspace(0,90,10))
158.        plt.grid(axis = 'y')
159.        plt.show()
160.
161. def motion_image_deformation(tumor_list, itv):
162.        """
163.        Parameters
164.        ----------
165.        tumor_list : List containing tumor coordinates in numpy arrays.
166.        itv : Array describing the itv. (tumor voxels = 1)
167.        Returns
168.        -------
169.        max_displacement : Tumor maximum displacement over the breathing cycle in mm calculate
form image deformation
170.        directinal_displacement : Displacement of Tumor in each direction.
171.
172.        """
173.        print('Generate Image Deformation')
174.        # Generate a ROI as the itv bounding box (add some margins)
175.        itv_bb = itv.nonzero()
```

```python
176.        z_min, z_max = np.min(itv_bb[0]) + 5, np.max(itv_bb[0]) + 5
177.        y_min, y_max = np.min(itv_bb[1]) + 5, np.max(itv_bb[1]) + 5
178.        x_min, x_max = np.min(itv_bb[2]) + 5, np.max(itv_bb[2]) + 5
179.        # Create an empty list to store the deformation vectors
180.        deformation_vectors = []
181.        # Loop over all pairs of frames
182.        for reference_index, current_index in itertools.combinations(range(len(tumor_list)),
2):
183.            reference_frame = tumor_list[reference_index]
184.            reference_roi = reference_frame[z_min:z_max, y_min:y_max, x_min:x_max]
185.            reference_image = sitk.GetImageFromArray(reference_roi)
186.            # Define the image spacing and origin (in mm)
187.            spacing = voxel_dimenstions
188.            origin = itv_com
189.            reference_image.SetSpacing(spacing)
190.            reference_image.SetOrigin(origin)
191.            current_frame = tumor_list[current_index]
192.            current_roi = current_frame[z_min:z_max, y_min:y_max, x_min:x_max]
193.            current_image = sitk.GetImageFromArray(current_roi)
194.            current_image.SetSpacing(spacing)
195.            current_image.SetOrigin(origin)
196.            # Register the current frame to the reference frame
197.            registration = sitk.ImageRegistrationMethod()
198.            registration.SetMetricAsMeanSquares()
199.            registration.SetOptimizerAsRegularStepGradientDescent(4.0, .01, 200)
200.
registration.SetInitialTransform(sitk.TranslationTransform(current_image.GetDimension()))
201.            registration.SetInterpolator(sitk.sitkLinear)
202.            registration.AddCommand(sitk.sitkIterationEvent, lambda: print(".", end='',
flush=True))
203.            final_transform = registration.Execute(reference_image, current_image)
204.            # Extract the deformation vector from the final transform
205.            deformation_vector = np.array(final_transform.GetParameters())
206.            deformation_vectors.append(deformation_vector)
207.        final_deformation_vectors = np.array(deformation_vectors)
208.        # Compute the peak-to-peak (ptp) along axes
209.        ptp_axis_SI = np.ptp(final_deformation_vectors[:, 0], axis=0)
210.        ptp_axis1_AP = np.ptp(final_deformation_vectors[:, 1], axis=0)
211.        ptp_axis2_RL = np.ptp(final_deformation_vectors[:, 2], axis=0)
212.        # Compute directional displacement
213.        directinal_displacement = [ptp_axis_SI, ptp_axis1_AP, ptp_axis2_RL]
214.        # Print the peak-to-peak values for each axis
215.        print(f"Peak-to-peak deformation along axis SI: {ptp_axis_SI}")
216.        print(f"Peak-to-peak deformation along axis AP: {ptp_axis1_AP}")
217.        print(f"Peak-to-peak deformation along axis RL: {ptp_axis2_RL}")
218.        print(f"Max deformation displacement: {max_displacement}")
219.        # Calculate pairwise distances between deformation vectors
220.        distances = []
221.        for pair in itertools.combinations(final_deformation_vectors, 2):
222.            displacement = distance.euclidean(pair[0], pair[1])
223.            distances.append(displacement)
224.        max_displacement2 = max(distances)
225.        print("Maximum displacement:", max_displacement2)
226.        return (deformation_vectors,max_displacement, directinal_displacement)
227.
228.
229. ### Call the functions
230. max_displacement, com_list, average_com, itv_com ,ictv_com=
center_of_mass_displacement(tumor_list, voxel_dimenstions)
231. prob_hist = prob_hist(prob_map)
232. plot_tumor_volume(tumor_list, voxel_volume= (voxel_volume*0.001)) #convert to cc
233. deformation_vectors,max_displacement, directinal_displacement =
motion_image_deformation(tumor_list,itv)
234.
235.
236.
```

B.4 ΔWEPL Algorithm

```python
1. import pandas as pd
2. import numpy as np
3. import matplotlib.pyplot as plt
4. from scipy.spatial.distance import euclidean
5. import pickle
6.
7. def calculate_distances(lines_coords ):
8.     """
9.     Parameters
10.     ----------
11.     lines_coords : Array represending the coordinates that the beam passes through
12.     Returns
13.     -------
14.     distances : Euclidean Chord Distance taking into consideration voxel dimensions.
15.
16.     """
17.     distances = []
18.     voxel_size= [3.0,1.0527,1.0527]
19.     for line_coords in lines_coords:
20.         first_point = np.array(line_coords[0]) * voxel_size
21.         last_point = np.array(line_coords[-1]) * voxel_size
22.         num_vox = len(line_coords) -1
23.         distance = euclidean(first_point, last_point)/(num_vox)
24.         distances.append(distance)
25.     return distances
26.
27. def generate_steps(theta,phi,direction_vector):
28.     """
29.     Parameters
30.     ----------
31.     theta : Gantry Angle in degrees.
32.     phi : Couch Angle in degrees
33.     direction_vector : Vector indicating initial beam direction. In radiotherapy is towards
Anterior direction
34.     Returns
35.     -------
36.     z_step : Step distance in the SI direction for magnitude 1 vector
37.     y_step : Step distance in the AP direction for magnitude 1 vector
38.     x_step : Step distance in the RL direction for magnitude 1 vector
39.
40.     """
41.     cos_g = np.cos(np.deg2rad(theta))
42.     sin_g = np.sin(np.deg2rad(theta))
43.     cos_c = np.cos(np.deg2rad(phi))
44.     sin_c = np.sin(np.deg2rad(phi))
45.     trans_matrix_g = np.array([[1, 0, 0],
46.                                [0, cos_g, sin_g],
47.                                [0, -sin_g, cos_g]])
48.     trans_matrix_c = np.array([[cos_c, 0, -sin_c],
49.                                [0, 1, 0],
50.                                [sin_c, 0, cos_c]])
51.     trans_matrix = np.matmul(trans_matrix_c, trans_matrix_g)
52.     z_step, y_step, x_step = np.matmul(trans_matrix, [0,-1,0])
53.     print('step size is' ,z_step, y_step, x_step )
54.     return (z_step, y_step, x_step)
55.
56. def generate_lines(tumor, distal_points, steps):
57.     """
58.     Parameters
59.     ----------
60.     tumor : A 3D array describing tumor coordinates
61.     distal_points : Array representing the distal edge points for the specific angle
combinations
62.     steps : Steps that will define the direction of the beam based on the angle
combinations
63.     Returns
```

```
 64.       -------
 65.       lines : A 3D array that idicates all the voxels that the beam will pass through
 66.       lines_coords : A list of arrays that indicate the coordinates from the disatl edge
point
 67.                      to the last point of the beam before it goes out of bounds
 68.           DESCRIPTION.
 69.
 70.       """
 71.       print('Generating lines')
 72.       lines_coords = []
 73.       lines_coords_set = []
 74.       lines = np.zeros_like(tumor)
 75.       z_step, y_step, x_step = steps
 76.       for distal_point in distal_points:
 77.           i, j, k = distal_point[:3]
 78.           line_coords = []
 79.           line_coords_set = set()
 80.           z, y, x = i,j,k
 81.           while (0 <= int(z) < tumor.shape[0]) and (0 <= int(y) < tumor.shape[1]) and (0 <=
int(x) < tumor.shape[2]):
 82.               current_point = (int(z), int(y), int(x))
 83.               if current_point not in line_coords_set:
 84.                   line_coords_set.add(current_point)
 85.                   line_coords.append(current_point)
 86.               lines[int(z), int(y), int(x)] = 1
 87.               z += z_step
 88.               y += y_step
 89.               x += x_step
 90.           lines_coords.append(line_coords)
 91.           lines_coords_set.append(list(line_coords_set))
 92.       return lines , lines_coords
 93.
 94. def get_distal_edge_point(tumor, steps, threshold=40):
 95.       """
 96.       Parameters
 97.       ----------
 98.       tumor : A 3D array describing tumor coordinates
 99.       steps : Steps that will define the direction of the beam based on the angle
combinations.
100.           Use negative step to find the distal edge.
101.       threshold : Threshold to limit the binary search so the code does not run forever
102.       Returns
103.       -------
104.       distal_points : A list of all the distal edge points coordinates
105.       distal_array : A 3D array representing the distal edge.
106.       """
107.       print('Calculating distal points')
108.       distal_points = []
109.       distal_array = np.zeros_like(tumor)
110.       z_step, y_step, x_step = steps
111.       for i in range(tumor.shape[0]):
112.           for j in range(tumor.shape[1]):
113.               for k in range(tumor.shape[2]):
114.                   if tumor[i, j, k] == 1:
115.                       z, y, x = i - z_step, j - y_step, k - x_step
116.                       count = 0
117.                       is_distal_edge = False
118.                       while z >= 0 and int(np.round(z)) < tumor.shape[0] and y >= 0 and
int(np.round(y)) < tumor.shape[1] and x >= 0 and int(np.round(x)) < tumor.shape[2] and count <
threshold:
119.                           z_round, y_round, x_round =
int(np.round(z)),int(np.round(y)),int(np.round(x))
120.                           if tumor[z_round, y_round, x_round] == 0:
121.                               break
122.                           if tumor[z_round, y_round, x_round] == 1:
123.                               is_distal_edge = True
124.                           count += 1
125.                           z, y, x = z - z_step, y - y_step, x - x_step
126.                       if is_distal_edge and count < threshold:
127.                           z, y, x = int(z), int(y), int(x)
```

```python
128.                         distal_points.append((z, y, x))
129.                         distal_array[z,y,x] = 1
130.                 distal_points =[*set(distal_points)]
131.         return distal_points , distal_array
132.
133.
134.  def main(tumor, phi, theta):
135.         steps = generate_steps(theta,phi,[0,-1,0])
136.         distal_points , distal_array= get_distal_edge_point(tumor,steps)
137.         lines ,lines_coords= generate_lines(tumor, distal_points,steps)
138.         distance = calculate_distances(lines_coords)
139.         return lines_coords,distance, lines
140.
141.  def calculate_beam_wepl(ct, lines_coords, distance):
142.         """
143.         Parameters
144.         ----------
145.         ct : 3D array of the CT scan to be investigated
146.         lines_coords : List of arrays that indicate the coordinates the beam passes through.
147.         distance : The Euclidean chord distance.
148.
149.         Returns
150.         -------
151.         beam_wepl : A list of the WEPL values of the projected beams
152.             [BEV, each voxel is represented by the sum of all voxels behind it along the beam
direction].
153.
154.         """
155.         beam_wepl = []
156.         for line_cord in lines_coords:
157.             line_sum = 0
158.             for coord in line_cord:
159.                 line_sum += ct[coord[0], coord[1], coord[2]]
160.             beam_wepl.append(line_sum * np.mean(distance))
161.         return beam_wepl
162.
163.  def line_welp_variation(lists):
164.         """
165.         Parameters
166.         ----------
167.         lists : list of the WEPL diferences of all beams from reference to evaluated
168.         Returns
169.         -------
170.         line_variation : The WEPL Variation of each beam from all evaluated phases
171.         """
172.         line_max_wepl  = np.amax(np.copy(lists), axis= 0)
173.         line_min_wepl  = np.amin(np.copy(lists), axis= 0)
174.         line_variation = np.subtract(line_max_wepl, line_min_wepl)
175.         return line_variation , line_max_wepl
176.
177.  """ Functions end """
178.  # load the list from disk
179.  with open("ct_eval_rsp.pkl", "rb") as f:
180.         ct_list = pickle.load(f)
181.         print('ct_list loaded')
182.
183.  #ref_mip_ct= np.load('ct_mip_rsp.npy')
184.  ref_ave_ct= np.load('ct_ave_rsp.npy')
185.  print('load plan CT')
186.  tumor = np.load('ictv.npy')
187.  print('load tumor')
188.  df = pd.read_csv('accepted_angles.csv')
189.  print('load angles')
190.  oar_beam = []
191.  max_wepl =[]
192.  min_wepl = []
193.  line_5mm_percentage =[]
194.  mean_WEPL = []
195.  variation_WEPL = []
196.  couch_angles= []
```

```
197. gantry_angles =[]
198.
199. for index, row in df.iterrows():
200.     gantry_angle = row['gantry_angle']
201.     couch_angle = row['couch_angle']
202.     print(f"gantry_angle: {gantry_angle}\tcouch_angle: {couch_angle}")
203.     lines_coords, distance, lines = main(tumor , couch_angle ,gantry_angle)
204.     ## Calculate Reference WEPL
205.     ref_wepl = calculate_beam_wepl(ref_ave_ct, lines_coords, distance)
206.     ### Calculate Evaluated WEPL
207.     i = 0
208.     eval_wepls = []
209.     for ct in ct_list:
210.         i = i+1
211.         print(i)
212.         eval_beam_wepl = calculate_beam_wepl(ct, lines_coords, distance)
213.         eval_wepls.append(eval_beam_wepl)
214.         ### Calculate Diference in WEPL
215.     dif_phase_wepl = []
216.     dif_phase_mean_wepl=[]
217.     ## Calculate diference in WEPL
218.     for eval_wepl in eval_wepls:
219.         dif_wepl = np.subtract(np.array(ref_wepl), np.array(eval_wepl))
220.         dif_phase_mean_wepl.append(np.mean(np.abs(dif_wepl)))
221.         dif_phase_wepl.append(dif_wepl)
222.     max_wepl.append(np.max(dif_phase_mean_wepl))
223.     min_wepl.append(np.min(dif_phase_mean_wepl))
224.     mean_WEPL.append(np.mean(dif_phase_mean_wepl))
225.     gantry_angles.append(gantry_angle)
226.     couch_angles.append(couch_angle)
227.
```

B.5 OAR Percentage Irradiation Algorithm.

The main python function (`def main(tumor, phi, theta):`) utilised in this code is identical to the one in the ΔWEPL algorithm presented in B.4.

```
1. def oar_irradiated_vol(oar,lines,oar_name):
2.     """
3.     Parameters
4.     ----------
5.     oar : Array of OAR investigated
6.     lines : Array showing the beam path for specific angles
7.     Returns
8.     -------
9.     perc_oar_vol : Percentage volume overlap of the irradiated OAR.
10.
11.     """
12.     print('Calculate percentage irradiated volume of "{}"'.format(oar_name))
13.     oar_total_vol = np.sum(oar)
14.     lines_oar = np.where(lines>=1, oar,0)
15.     if np.max(lines_oar)>=1:
16.         oar_beam_volume = np.sum(lines_oar)
17.         perc_oar_vol = (oar_beam_volume/oar_total_vol)*100
18.     else:
19.         perc_oar_vol = 0
20.     return perc_oar_vol
21.
22. ref_ave_ct= np.load('ct_ave_rsp.npy')
23. print('load plan CT')
24. tumor = np.load('ictv.npy')
25. print('load ictv')
26. heart = np.load('heart.npy')
27. print('Load Heart')
28. cord = np.load('cord.npy')
29. print('Load Cord')
30. rlung = np.load('rlung.npy')
```

```python
31. print('Load RLung')
32. llung = np.load('llung.npy')
33. print('Load LLung')
34. lungs = np.load(lungs.npy)
35. print('Load Lungs')
36. df = pd.read_csv('accepted_angles.csv')
37. print('load angles')
38.
39. beam_heart = []
40. beam_cord = []
41. beam_rlung = []
42. beam_llung = []
43. beam_lungs = []
44. gantry_angles = []
45. couch_angles = []
46.
47. for index, row in df.iterrows():
48.     gantry_angle = row['gantry_angle']
49.     couch_angle = row['couch_angle']
50.     print(f"gantry_angle: {gantry_angle}\tcouch_angle: {couch_angle}")
51.
52.     lines_coords, lines, distal_points , steps  = main(tumor , couch_angle ,gantry_angle)
53.     heart_irr = oar_irradiated_vol(heart, lines, 'heart')
54.     cord_irr = oar_irradiated_vol(cord,lines, 'cord')
55.     rlung_irr = oar_irradiated_vol(rlung,lines, 'rlung')
56.     llung_irr = oar_irradiated_vol(llung,lines, 'llung')
57.     lungs_irr = oar_irradiated_vol(lungs,lines, 'lungs')
58.     gantry_angles.append(gantry_angle)
59.     couch_angles.append(couch_angle)
60.     beam_heart.append(heart_irr)
61.     beam_cord.append(cord_irr)
62.     beam_rlung.append(rlung_irr)
63.     beam_llung.append(llung_irr)
64.     beam_lungs.append(lungs_irr)
65.
```